Charge properties of cuprates: Ground state and Excitations

Christoph Waidacher

Dissertation
Institut für Theoretische Physik
Technische Universität Dresden
1999

Contents

Preface

This thesis investigates charge properties of undoped cuprate compounds. Cuprates are strongly correlated electron systems. Therefore, they have several unusual and interesting properties. In particular, upon doping many of these compounds become superconducting at surprisingly high temperatures. This phenomenon is still not well understood. By trying to understand the charge properties of undoped cuprates one also hopes to shed some light on the (unknown) mechanism of superconductivity. Fortunately, several excellent experimental investigations of charge excitations in undoped cuprates are available. Some of these experimental results will be used to test the theoretical approaches developed in the present work.

The thesis is organized in three parts. Part I consists of an introduction into the field of research, both from the view of experiment (Chap. 1), and theory (Chap. 2). Charge properties pertain to the ground state as well as to excitations. Consequently, Parts II and III deal with ground-state properties and excitations, respectively. In Part II we develop a new analytical approach to the approximation of ground-state charge properties (Chap. 3) and apply it to the geometries found in the cuprates (Chap. 4). With the additional help of numerical methods (Projector Quantum Monte Carlo) we analyze the influence of the dimensionality on the ground state properties (Chap. 5). The topic of Part III are charge excitations, especially Cu $2p_{3/2}$ core-level X-ray photoemission spectroscopy (XPS). Low dimensional systems are treated with exactly solvable models, which allow a good description of experimental data (Chap. 6). For systems of higher dimensionality an approximation scheme using projection technique is presented (Chap. 7). The results are compared to several experimental spectra (Chap. 8). As in Part II, the analysis centers around the question: How does the dimensionality of the compound influence its charge properties?

Part I

Introduction

Chapter 1

Motivation, materials, and measurements

In this chapter we formulate the basic questions that this thesis will try to clarify. After a few general motivating remarks in Sec. 1.1, some important physical properties of the materials are described in Sec. 1.2. A schematic view of the experimental technique (core-level photoemission spectroscopy) is developed in Sec. 1.3. In this section we also explain why these experiments provide information about the electronic properties of the materials. Finally, in Sec. 1.4 we present the experimental results that will be analyzed in this thesis.

1.1 Motivation

Since the discovery of high-temperature superconductivity in ceramic copper oxide compounds in 1986 [11], there has been a large number of publications starting with the words 'Since the discovery of high-temperature superconductivity...'. Nevertheless, in spite of concentrated world-wide efforts, these compounds continue to puzzle solid-state physicists for by now almost 15 years. Among the works on high-temperature superconductivity there are excellent review articles [22] and [18], which describe experimental findings as well as theoretical proposals. Therefore, to give a motivation for the present thesis, we restrict ourselves to a few general remarks and refer the interested reader to the above articles and references cited therein.

The interest in high-temperature superconducting (high-T_c) compounds has three basic reasons. Experimentally, these materials have many unusual and interesting properties, also above the critical temperature T_c. Theoretically, strong correlations in high-T_c compounds call for the use of many-body models – a

notoriously challenging field of research. And, finally, these materials offer the possibility of industrial applications.

The common structural feature of all cuprates are CuO_2 planes which are separated by layers of other atoms. Typical examples for these cuprates are La_2CuO_4 and $YBa_2Cu_3O_6$. These materials may be doped, for example by introducing strontium ($La_{2-x}Sr_xCuO_4$), or oxygen ($YBa_2Cu_3O_{6+x}$). Upon doping, the cuprates become superconducting below a critical temperature T_c. This temperature is called "high" if it exceeds approximately 30 K. For $La_{1.85}Sr_{0.15}CuO_4$ the critical temperature is 39 K. In the case of $YBa_2Cu_3O_7$ one observes $T_c = 92$ K. Currently, there is no generally accepted explanation for superconductivity at high temperatures. It is, however, widely believed that superconductivity is related to physical properties of the CuO_2 planes. The other layers of ions mainly seem to provide charge carriers for these planes. For this reason most of the research in the field is dedicated to the investigation of CuO_2 planes. It turns out that already the undoped "parent" compounds have interesting spin- and charge properties. By understanding these properties one also hopes to shed some light on the superconducting mechanism. In this respect, the low dimensionality of CuO_2 planes is of special interest. How strongly, one might ask, do the electronic properties of Cu-O structures depend on their dimensionality? Fortunately, there are substances ("model cuprates") that contain Cu-O structures of even lower dimensionality than the CuO_2 planes (see Sec. 1.2). Thus, experimental answers to the above question can be obtained, for example using X-ray photoemission spectroscopy (see Secs. 1.3 and 1.4). In the following, we shall try to understand the results of these experiments from a theoretical point of view.

Summarizing, the topic of the present thesis is the theoretical description of charge excitations in low-dimensional undoped model cuprates. One of the questions we shall try to clarify is to which extent the charge properties of CuO structures do depend on their dimensionality.

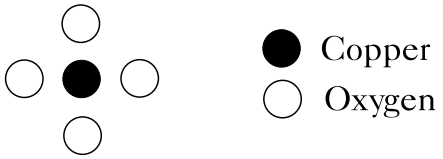

Figure 1.1: The CuO_4 plaquette: the basic building element of the cuprates.

1.2 Crystal structure and other properties

The materials that we shall investigate in this thesis are the cuprates Bi_2CuO_4, Li_2CuO_2, Sr_2CuO_3, and $Sr_2CuO_2\,Cl_2$. In general, the lattice structure of all these model cuprates is orthorhombic or tetragonal, as is the lattice structure of the high-T_c parent compounds. The basic building element of the cuprates are CuO_4 plaquettes, i.e. Cu ions surrounded by O ions (see Fig. 1.1). There are, however, some important differences in the arrangement of the CuO_4 plaquettes in these materials.

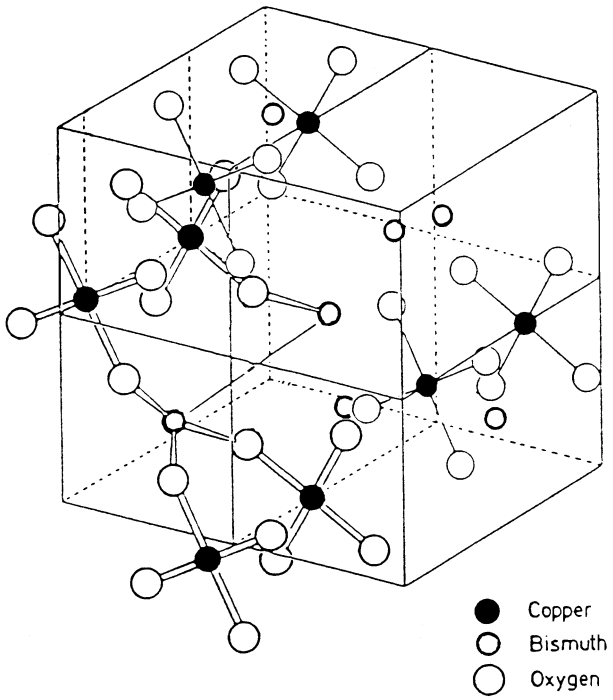

Figure 1.2: Lattice structure of Bi_2CuO_4 (after [2]).

Figure 1.2 shows the lattice structure of Bi_2CuO_4. In this tetragonal structure, CuO_4 plaquettes are stacked above each other. Notice that the Cu ions are not bridged by other ions. Thus, one might assume that electronically the CuO_4 plaquettes in Bi_2CuO_4 are rather isolated as well. This assumption will be discussed later (Sec. 6.3). Magnetically, however, the CuO_4 plaquettes in Bi_2CuO_4 cannot be regarded as isolated since band structure calculations show that they are connected by a small (0.1 eV) but rather isotropic transfer integral [85]. In addition, the Cu ions order antiferromagnetically at about 50 K (see below).

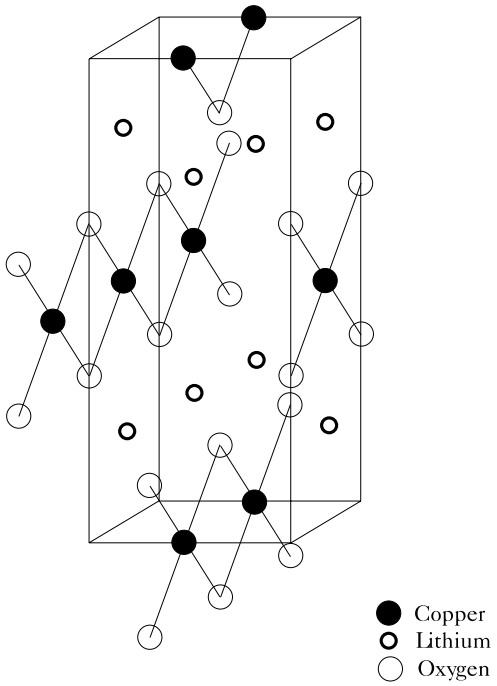

Figure 1.3: Lattice structure of Li_2CuO_2 (after [86]).

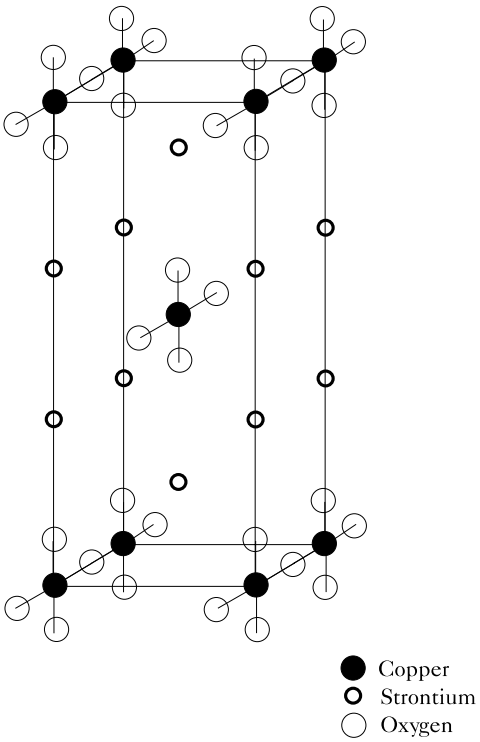

Figure 1.4: Lattice structure of Sr_2CuO_3 (after [4]).

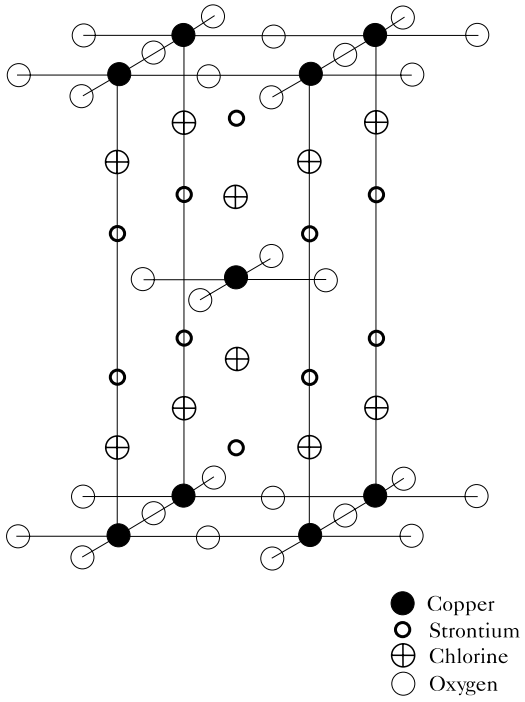

Figure 1.5: Lattice structure of $Sr_2CuO_2Cl_2$ (after [67]).

The next two cuprates contain chain-like Cu-O structures. The orthorhombic lattice structure of Li_2CuO_2 is shown in Fig. 1.3. The Cu-O structures in this compound form chains of edge-sharing plaquettes. Figure 1.4 shows the orthorhombic lattice structure of $Sr_2\ CuO_3$. In contrast to the edge-sharing chains in Li_2CuO_2, the CuO_4 plaquettes in Sr_2CuO_3 form corner-sharing chains.

Finally, in Fig. 1.5 we show the lattice structure of $Sr_2CuO_2Cl_2$. This material has a body centered tetragonal symmetry. It is isostructural to La_2CuO_4, with Sr instead of La ions, and with Cl ions replacing the apex O. In contrast to La_2CuO_4 , which undergoes an orthorhombic distortion below a temperature of 530 K, $Sr_2CuO_2Cl_2$ remains undistorted for temperatures between 10 and 300 K (see Ref. [101]). Furthermore, $Sr_2CuO_2Cl_2$ apparently cannot be doped [67].

The Cu-O sub-structures of the four cuprates discussed above may be schematically displayed as in Fig.1.6. There are Cu-O networks of different dimensionality: (a) the "zero-dimensional" isolated plaquettes in Bi_2CuO_4, (b) the one-dimensional chains in Li_2CuO_2 and (c) in Sr_2CuO_3, and (d) the two-dimensional planes in $Sr_2CuO_2Cl_2$. Below, an analysis of the electronic structure will show that the edge-sharing chains in Li_2CuO_2 should rather be regarded as consisting of isolated plaquettes. In this sense, Li_2CuO_2 may be called a "zero-dimensional" cuprate as well. Of course, a structural analysis alone cannot answer the question

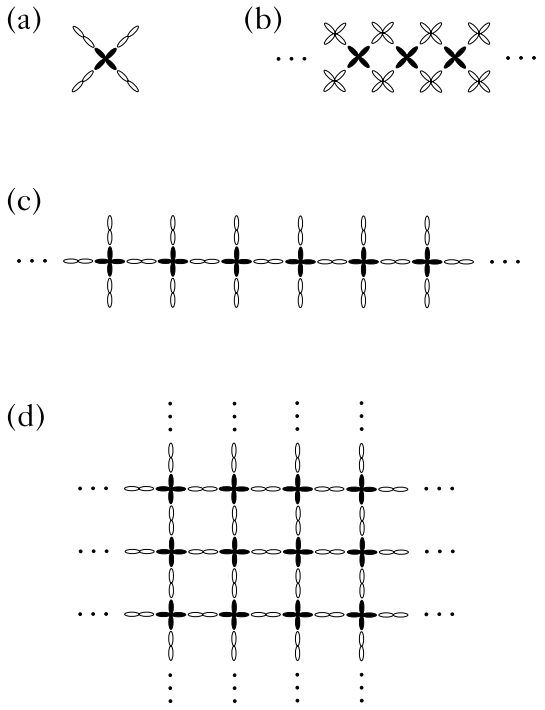

Figure 1.6: Cu-O sub-structures of the model cuprates: (a) Bi_2CuO_4, (b) Li_2CuO_2, (c) Sr_2CuO_3, (d) $Sr_2CuO_2Cl_2$. Cu $3d_{x^2-y^2}$ orbitals are shown in black, O $2p_{x(y)}$ orbitals in white.

if it is possible to describe charge excitations in the cuprates by considering only the Cu-O sub-structures while neglecting all other ions in the materials. This problem will be addressed in chapters 6 and 8.

In Table 1.1 we show the lattice constants, the Cu-O distance, and other typical distances. These distances have been determined at room temperature (except for Sr_2CuO_3 where values for 11 K are shown). All distances are in Angstrom. $O^{\perp}$ denotes the out-of chain O site in Sr_2CuO_3 (see Fig.1.6(c)). The Cu-O distances in all compounds are of the same order of magnitude. Notice,

	a	b	c	Cu-O	other distances	reference
Bi_2CuO_4	8.50		5.82	1.94	Cu-Cu: 2.91	[78]
Li_2CuO_2	2.86	9.39	3.66	1.96		[86]
Sr_2CuO_3	3.91	3.49	12.69	1.95	Cu-$O^{\perp}$: 1.96	[4]
$Sr_2CuO_2Cl_2$	3.97		15.61	1.99	Cu-Cl: 2.86	[67]
$La_{1.85}Sr_{0.15}CuO_4$	3.80		13.19	1.90	Cu-O^{apex}: 2.41	[67]

Table 1.1: Lattice constants and typical distances (Å) in the model cuprates.

though, that the Cu-O distances in the model cuprates are consistently larger than in $La_{1.85}Sr_{0.15}CuO_4$. The largest separation between Cu and O is found in $Sr_2CuO_2Cl_2$. This cuprate has also the largest lattice constant of the materials discussed here. It is 18% longer than c in the La compound.

The basic electronic properties of the cuprates are similar. In an ionic picture, all these compounds have a simple Cu valency of 2+. Since a Cu atom has a $[\mathrm{Ar}]\,3d^{10}4s^1$ electron configuration, this implies a $3d^9$ configuration for the Cu ions. On the other hand, the O ions, which have an atomic $[\mathrm{He}]\,2s^2 2p^4$ electron configuration, have a valency of 2−. Thus, the O ions have a completely filled $2p^6$ shell. For this reason it is appropriate to use the hole notation, with one hole per Cu-O unit cell. In the $3d$ shell, the hole occupies an orbital with $3d_{x^2-y^2}$ character (see also Sec. 2.1). Furthermore, there is a strong hybridization between the Cu $3d_{x^2-y^2}$ orbital and the O $2p_{x(y)}$. Therefore, the hole occupies not only the Cu $3d_{x^2-y^2}$ orbital but also, to a certain degree, the O $2p_{x(y)}$ orbitals. As shown in Fig. 1.6 for (c) the CuO_3 chain and (d) the CuO_2 plane, two neighbouring Cu $3d_{x^2-y^2}$ orbitals hybridize with the same O $2p$ orbital. This allows the hole in the unit cell of these compounds to delocalize onto the neighbouring Cu site. For the CuO_2 chain configuration, on the other hand, the Cu orbitals hybridize with different O $2p$ orbitals (see Fig. 1.6(b)). For this reason, the hole in the unit cell of Li_2CuO_2 cannot easily delocalize onto the neighbouring Cu site. The same conclusion can be drawn from band-structure calculations [85],[110]. As a first approximation, Li_2CuO_2 may consequently be regarded as consisting of isolated plaquettes rather than of chains with nearest-neighbour delocalization.

Since there is one hole per Cu site, one would expect the undoped cuprates to be metallic in the absence of correlations. This is, in fact, also the result of LDA band-structure calculations. For example, in the case of La_2CuO_4 a paramagnetic ground state is predicted [51]. However, experimentally all of these compounds are insulators. This is a consequence of strong correlations due to Coulomb interaction which are not adequately taken into account in the LDA calculations. These correlations make double occupancies of holes on Cu sites (and, to a smaller degree, double occupancies of O sites) energetically unfavoured.

Finally, we shortly discuss some magnetic properties of the (undoped) materials presented in this section. All of them order antiferromagnetically below a Néel temperature T_N. (The in-chain order of the CuO_2 chains in Li_2CuO_2 is ferromagnetic.) As shown in Table 1.2, the value of T_N differs strongly for different compounds. The fact that T_N is very small for Sr_2CuO_3, Li_2CuO_2, and relatively small for Bi_2CuO_4, underscores the low dimensionality of these compounds.

Summing up, all materials presented in this section are strongly correlated systems with one hole per Cu site. This hole occupies a state dominated by

	T_N (K)	ordered Cu moment (μ_B)	reference
Bi_2CuO_4	$\simeq 50$	0.56	[78]
Li_2CuO_2	8.3	0.96	[86]
Sr_2CuO_3	5	0.06	[55],[4],[57]
$Sr_2CuO_2Cl_2$	256	0.34	[41],[101]
La_2CuO_4	$\simeq 300$	0.60	[101]

Table 1.2: Magnetic properties of the model cuprates.

a Cu $3d_{x^2-y^2}$ orbital which hybridizes with O $2p_{x(y)}$ orbitals. At low temperatures the spins on the Cu sites order antiferromagnetically. The Cu-O structures in the materials have different dimensionality: Bi_2CuO_4 and Li_2CuO_2 may be roughly described as consisting of single CuO_4 plaquettes; Sr_2CuO_3 contains one-dimensional CuO_3 chains, and $Sr_2CuO_2Cl_2$ consists of two-dimensional CuO_2 planes.

1.3 Schematic view of core-level XPS

In the field of experimental solid-state physics, PhotoEmission Spectroscopy (PES) is a method of fundamental importance [60]. For a review of PES in the field of high-temperature superconductors see Ref. [91]. Figure 1.7 shows a sketch of a typical experimental setup.

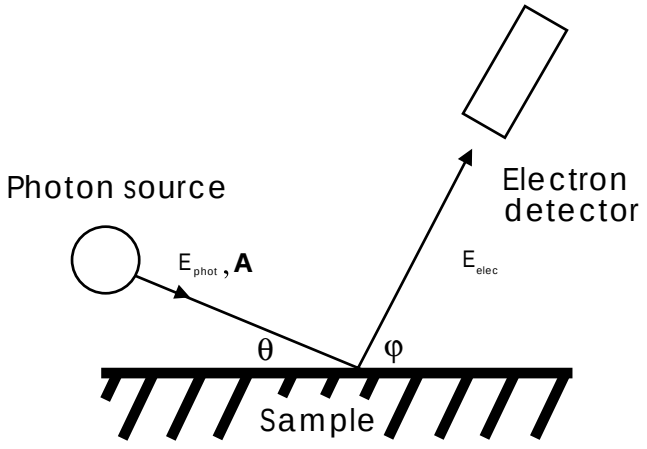

Figure 1.7: Setup of a photoemission experiment (after [49]).

Photons with an energy of $E_{\rm phot}$ and a polarization $\mathbf{A}$ are emitted from a light source, and strike the sample under an angle θ with respect to the surface. Due

to the photoelectric effect, the sample emits electrons which are analyzed with respect to their kinetic energy E_{elec} and their emission angle φ with the surface. Thus, the measured quantity is the intensity $I\left(E_{\mathrm{phot}}, \mathbf{A}, \theta, E_{\mathrm{elec}}, \varphi\right)$ of the emitted electrons as a function of all experimental parameters. The light source may be a gas discharge lamp, an X-ray tube, or a synchrotron radiation source. A (crystal) monochromator filters incoming light of the desired energy E_{phot}, and an (electrostatic) energy analyzer does the same for the kinetic energy E_{elec} of the outcoming photo electrons. For low emission rates the signal is enhanced by an electron amplifier. Finally, the photo electrons are detected using an electron collector.

The so-called three-step model [49] describes the photoemission process as follows: A photon strikes the sample and excites an electron (step 1). The excited electron approaches the surface of the sample (step 2). Finally, the electron escapes the sample by overcoming the surface-work function Φ (step 3). Of course, in reality the photoemission is a single quantum-mechanical process. The basic assumption of the three-step model is that this process can be approximately separated into the three isolated steps described above. Furthermore, one assumes that steps 2 and 3 influence the spectra only in a simple way. Step 2 is supposed simply to lead to a background due to the scattering of electrons from other parts of the crystal during the emission. In the analysis of the spectra, this background may then be subtracted properly. The escape from the sample surface in step 3 is assumed to lead to a simple energy shift in the spectra. Due to energy conservation, the following equation holds for the kinetic energy of the photo electrons

$$E_{\mathrm{elec}} = E_{\mathrm{phot}} - \Phi - |\omega| \ , \tag{1.1}$$

where the work function Φ is measured from the Fermi level to the spectrometer level, and where ω is the so-called binding energy. The work function Φ is a spectrometer constant which has to be calibrated with a well known sample such as Au or Cu. The binding energy ω, on the other hand, is an excitation energy which contains important physical information. Usually, ω is measured from the Fermi level down to lower energies, and it is given as a positive number. In Sec. 2.2 we will see that ω may be interpreted as the energy difference between the ground state of a N-electron system and the eigenstates of a $(N-1)$-electron system.

There are some principle experimental restrictions connected with PES. The most important property of PES is its surface sensitivity. According to the so-called "universal curve" [49] the electron escape depth lies between about 3 Å and 20 Å for E_{elec} between 10 eV and 1500 eV. Therefore, PES allows to obtain

$2s$	$2p_{1/2}$	$2p_{3/2}$	$3s$	$3p_{1/2}$	$3p_{3/2}$
1096.7	952.5	932.5	122.5	77.2	75.2

Table 1.3: Binding energies of core levels in free Cu atoms (all energies in eV).

information only about a relatively thin volume on the surface of the sample. On the one hand, this makes PES the method of choice for the analysis of surface properties. On the other hand, it may be difficult to extract bulk properties of the sample from PES spectra. In fact, some of the early photoemission data from the high-temperature superconductors were discredited due to their surface problems [91]. Thus, surface quality of the samples is of crucial importance. One way to estimate the bulk contribution to the spectrum is an analysis of the dependence on the incident angle θ of the photons. Since the electron escape depth decreases for smaller θ, the variation of θ allows to reduce or enlarge the surface contribution to the spectra. Thus, if the spectra show no or only small change with θ one may assume that surface contributions are small. Fortunately, the compounds discussed in Sec. 1.2 turn out to have good cleavage leading to high surface quality [14]. In $Sr_2CuO_2Cl_2$, for instance, the first CuO_2 plane lies well below the surface. An additional experimental complication in PES is the necessity to use ultra-high vacuum to preserve good surfaces. Furthermore, since during a PES measurement the sample is continuously losing electrons, one has to take account of charging effects. These are especially important for insulating materials, like the undoped cuprates.

Since the kinetic energy $E_{\rm elec}$ of the photo electrons has to be positive, according to Eq.(1.1) the energy $E_{\rm phot}$ of the incoming light determines the maximal excitation energies in the PES. If one is interested only in the emission of valence electrons, photo energies in the hard UV or soft X-ray range between 3 eV and 100 eV are sufficient. These experiments are called Ultraviolet Photoemission Spectroscopy (UPS). For excitations from core levels, on the other hand, high energy X-rays are required. This can be inferred from Table 1.3, which shows the binding energies of the core levels in free Cu atoms (after[49]). Notice that the strong spin-orbit coupling leads to a splitting of $2p_{1/2}$ and $2p_{3/2}$ states. In view of these binding energies one needs photo energies $E_{\rm phot}$ of more than 1000 eV for the investigation of core-level excitations. In this case one speaks of X-ray Photoemission Spectroscopy (XPS). Note that $E_{\rm phot}$ restricts only the maximum excitation energy. Therefore, low-energy excitations from valence states are observed in XPS as well.

In this thesis we shall be concerned exclusively with Cu $2p_{3/2}$ core-level XPS spectra, i.e. $E_{\rm phot} > 1000$ eV. To be precise, the energy used in the experiments

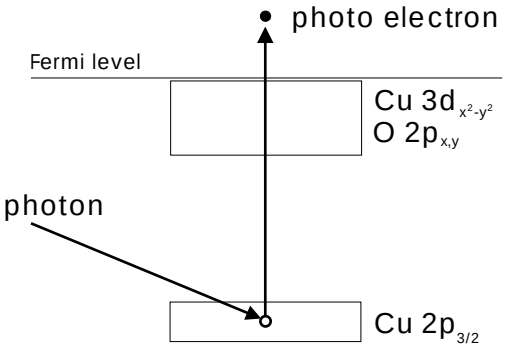

Figure 1.8: Schematic view of the Cu $2p_{3/2}$ photoemission process.

shown in Sec. 1.4 is $E_{\text{phot}} = 1486.6$ eV [16]. We shall not consider the dependence of the spectrum on the polarization vector $\mathbf{A}$ of the incoming light, and the emission angle φ of the photo electrons. These are important parameters for a different kind of measurement, the so-called Angle-Resolved PhotoEmission Spectroscopy (ARPES). Furthermore, we will not analyze the dependence of the intensity on the incident angle θ of the X-rays. Therefore, the experimental quantity that we will try to describe in the following is the spectral intensity $I(\omega)$ as a function of binding energy ω.

Summarizing, we may give the following schematic view of Cu $2p_{3/2}$ core-level XPS in cuprate compounds, see Fig. 1.8. An incident X-ray photon hits an electron in the $2p_{3/2}$ core level of one of the Cu ions. This electron is emitted from the crystal and detected by the electron collector. In atomic Cu, the resulting spectrum ideally consists of a single sharp peak at the binding energy of 932.5 eV, because the system cannot convert the energy of the incoming photon into inner excitations. In this case the photoemission measures occupation probabilities of one-electron states, essentially mirroring the density of states of the electrons. However, in the cuprates there is a strong interaction between the Cu $2p_{3/2}$ core hole created during the photoemission, and the valence holes at and near the Cu core-hole site. Therefore, one observes additional spectral lines which correspond to different inner excitations of the system. These excitations are often called "screening processes", as one can imagine them as a screening response of the valence holes to the perturbation created by the Cu $2p_{3/2}$ core hole. Consequently, the binding energies that are observed in the cuprates are more than simple atomic binding energies, since they also contain the energies of additional excitations in the crystal.

The importance of Cu $2p_{3/2}$ core-level XPS in cuprate compounds is, therefore, that they allow to extract information about the valence system. We shall try to give a more concise microscopical picture of the Cu $2p_{3/2}$ core-level emission

process in Chap. 2. Before, let us have a first look at the experimental results in the next section.

1.4 Experimental results

The experiments that we analyze theoretically in this thesis were performed by T. Böske and coworkers from the group of J. Fink at the IFW Dresden [15], [16]. Of course, these are not the only Cu $2p_{3/2}$ core-level XPS measurements available for the cuprates presented in Sec. 1.2, and we shall discuss some other results in Sec. 2.3. However, the work by Böske and coworkers represents the first systematic study using single crystals and high-resolution XPS (for details about the sample preparation and experiment see [15], [16]). Therefore, it is an ideal starting point to investigate the influence of the Cu-O network geometry on charge excitations in undoped cuprates.

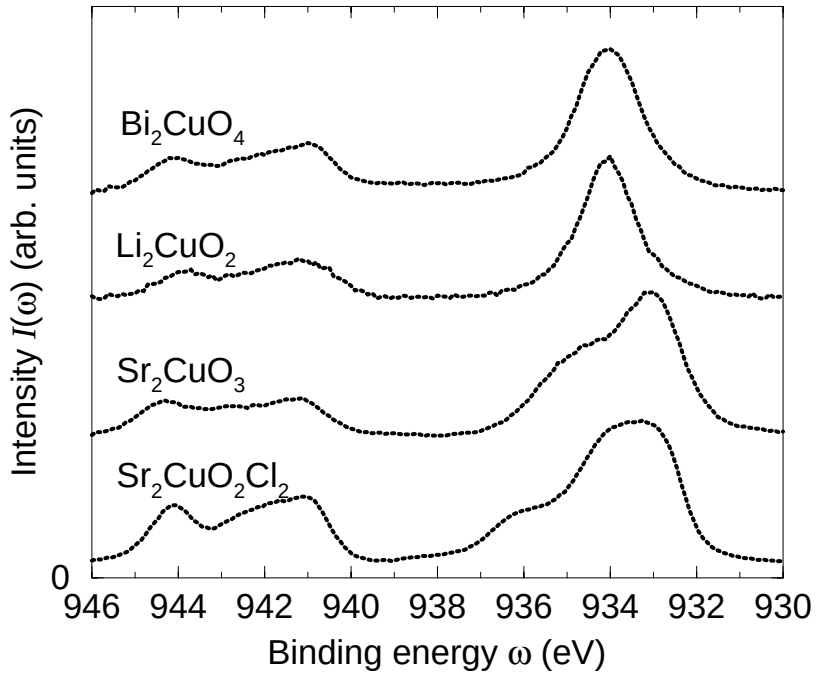

Figure 1.9: Cu $2p_{3/2}$ core-level spectra of the model cuprates (from Ref.[16]).

Figure 1.9 shows the Cu $2p_{3/2}$ core-level spectra of Bi_2CuO_4, Li_2CuO_2, Sr_2CuO_3, and $Sr_2CuO_2Cl_2$ in the binding-energy range from 930 eV to 946 eV [16]. An integral background has been subtracted, and the spectra are normalized to the leading peak. Thus, the intensities can only be given in arbitrary units. The

Compound	I_s/I_m
Bi_2CuO_4	≤ 0.58
Li_2CuO_2	0.56
Sr_2CuO_3	0.37
$Sr_2CuO_2Cl_2$	0.52

Table 1.4: Experimental intensity ratios I_s/I_m between satellite and main line.

energy resolution is about 0.4 eV. Due to charging effects, the accuracy of the absolute energy values is estimated to be ± 0.3 eV [16]. All spectra basically consist of two regions with non-vanishing spectral weight: the so-called satellite between 940 eV to 945 eV binding energy, and the main line between about 932 eV and 936 eV binding energy. The satellite is more or less similar for all materials. The main line, on the other hand, differs strongly from one compound to the other. For the "zero-dimensional" cuprates Bi_2CuO_4 and Li_2CuO_2 one observes a comparatively narrow and symmetric main line. In contrast, the main line of the one-dimensional Sr_2CuO_3 has a clearly resolved shoulder at higher binding energies. For the two-dimensional $Sr_2CuO_2Cl_2$ the main line contains even more substructure. An analysis using Voigt functions shows that at least three features are needed to obtain a reasonable fit [15]. Thus, these experiments suggest a strong dependence of the form of the Cu $2p_{3/2}$ main line on the Cu-O geometry of the compound. In particular it seems that the number of features of the main line increases with increasing dimensionality of the Cu-O structure. It is one of the aims of this thesis to check the validity of these hypotheses.

We finally note that further valuable information contained in the spectra shown in Fig. 1.9 is the ratio between the intensity of the satellite I_s and the main line I_m. The experimental values from Ref. [16] are shown in Table 1.4. Since in Bi_2CuO_4 an emission from the Bi $4s$ core level contributes at about 940 eV, the value 0.58 for I_s/I_m is only an upper estimate [16].

Chapter 2

Microscopic Description

After the more phenomenological discussion in Chap. 1, we now develop a microscopic picture of the Cu $2p$ core-level XPS. In Sec. 2.1, Hamiltonians are introduced to describe the electronic valence system of the compounds from Sec. 1.2, and the interaction between core holes and this valence system. In Sec. 2.2, the intensity of the XPS is expressed by means of a correlation function. This correlation function will be evaluated in the following chapters. It turns out that this evaluation requires the solution of two problems. First, one has to find an approximation for the ground state of the Hamiltonian before the creation of the core hole. This problem will be addressed in Part II of this thesis. Second, given the ground state, one has to solve the dynamics of the system after the creation of the core hole. This problem will be discussed in Part III. Before we are going to tackle these two problems, the present chapter is concluded with Sec. 2.2, where we give an overview of results by other groups.

2.1 Hamiltonians

We now construct a Hamiltonian H_{XPS} for the description of the Cu $2p_{3/2}$ core-level XPS. This operator contains a part H which describes the essential electronic valence structure of the cuprates discussed in Sec. 1.2. Furthermore, there is a part H_c that takes account of the interaction with the core holes created in the photoemission process

$$H_{\mathrm{XPS}} = H + H_c \ . \tag{2.1}$$

First, we discuss the part H, i.e. the operator of the electronic system in absence of core holes. The first simplifying assumption is to take one single CuO structure as representative for the whole crystal, and to neglect all other constituents of

the material. This should be justified if the CuO structures are reasonably well separated from each other and from the other ions in the crystal. As we have seen from the crystal structures in Sec. 1.2, there is some reason to assume that this approach is justified. Nevertheless, one cannot take this assumption for granted, and its validity will be discussed in chapters 6 and 8. The next simplifying assumption is to neglect all filled orbitals of the Cu and O ions. These are the Cu $1s$, $2s$, $2p$, $3s$, and $3p$ orbitals, and the O $1s$ and $2s$ orbitals. This approximation is justified as long as the influence of the filled orbitals on the electronic structure can be neglected or at least absorbed into remaining parameters of the model. For instance, there is theoretical evidence that the s orbitals in Sr_2CuO_3 lead to an enlarged effective hybridization between Cu and O sites [85]. Thus, in the Hamiltonian H only the Cu $3d$ and the O $2p$ orbital are taken into account. Due to its small spin-orbit coupling (order of magnitude 0.1 eV [71]), the states in these orbitals may be classified according to crystal symmetry. There are ten Cu states: $3d^\sigma_{x^2-y^2}$, $3d^\sigma_{xy}$, $3d^\sigma_{xz}$, $3d^\sigma_{yz}$, and $3d^\sigma_{z^2-r^2}$ (with $\sigma = \pm 1/2$), and six O states: $2p^\sigma_x$, $2p^\sigma_y$, and $2p^\sigma_z$. From all these states we only take account of the states with highest energy, because these are the states that the valence holes of the CuO structure will predominantly occupy. Furthermore, we restrict ourselves to the states that hybridize most, i.e. the states $3d_{x^2-y^2}$ for Cu, and $2p_x$, $2p_y$ for O.

For the geometry of a two-dimensional CuO_2 plane, in which each unit cell contains one Cu $3d$ and two O $2p$ orbitals, we are thus led to the well-known three-band Hubbard or Emery model [29]. On the other hand, in a one-dimensional CuO_3 chain, each unit cell contains four orbitals. Therefore, strictly speaking, this model should be called "four-band Hubbard model". To avoid confusion, we will use the term "multi-band Hubbard model", independent of the geometry under consideration. Due to the atomic $3d^9 2p^6$ configuration, it is appropriate to use the hole notation, with one hole per unit cell (the so-called case of half-filling). The Hamiltonian H consists of an atomic part H_0 and a hopping part H_1

$$H = H_0 + H_1 \ , \tag{2.2}$$

$$H_0 = \Delta \sum_{j\sigma} n^p_{j\sigma} + U_d \sum_i n^d_{i\uparrow} n^d_{i\downarrow} + U_p \sum_j n^p_{j\uparrow} n^p_{j\downarrow} + V_{pd} \sum_{\langle ij\rangle \sigma\sigma'} n^d_{i\sigma} n^p_{j\sigma'} \ , \tag{2.3}$$

$$H_1 = t_{pd} \sum_{\langle ij\rangle\sigma} \phi^{ij}_{pd} \left(p^\dagger_{j\sigma} d_{i\sigma} + \text{h.c.} \right) + t_{pp} \sum_{\langle jj'\rangle\sigma} \phi^{jj'}_{pp}\, p^\dagger_{j\sigma} p_{j'\sigma} \ . \tag{2.4}$$

The indices i and j denote Cu and O sites, respectively. σ is the spin-index (with values $\pm 1/2$). $d^\dagger_{i\sigma}$ ($p^\dagger_{j\sigma}$) create a hole with spin σ in the i-th Cu $3d$ orbital (j-th O $2p$ orbital), and $n^d_{i\sigma}$ ($n^p_{j\sigma}$) are the corresponding number operators. The

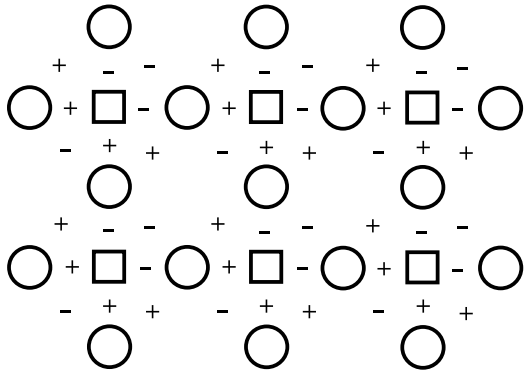

Figure 2.1: Definition of the phase factors ϕ_{pd}^{ij} and $\phi_{pp}^{jj'}$ in the case of the CuO_2 plane. Cu sites are represented by squares, O sites by circles.

first term in the atomic part H_0 denotes the charge-transfer energy contribution. The charge-transfer energy Δ is the difference between the on-site energies of O and Cu sites. To obtain this form, we have subtracted a constant energy that consists of all Cu on-site energies ϵ_i^d. The second and the third term on the r.h.s. of Eq.(2.3) describe the on-site Coulomb repulsions on Cu sites (parameter U_d) and on O sites (U_p). The last term in H_0 is the inter-site Coulomb repulsion (V_{pd}) between holes on neighbouring Cu and O sites, where $\langle ij \rangle$ denotes summation over nearest-neighbour pairs. The hopping part H_1 consists of two terms. First, there is the hybridization between neighbouring Cu $3d$ and O $2p$ orbitals (hopping strength t_{pd}), and, second, there is the hybridization between neighbouring O $2p$ orbitals (hopping strength t_{pp}). The factors ϕ_{pd}^{ij} and $\phi_{pp}^{jj'}$ in Eq.(2.4) give the correct sign for the hopping processes. They are defined in Fig. 2.1.

Using band-structure calculations for La_2CuO_4 [66], [51],[40], the following parameter values for model (2.2) have been obtained (all values are in eV)

Δ	U_d	U_p	V_{pd}	t_{pd}	t_{pp}
3.6	10.5	4	1.2	1.3	0.65

(2.5)

Oxygen occupancies are expected to be smaller than copper occupancies, because the positive value of the charge-transfer energetically favours copper sites, and because there are at least two oxygen sites per hole (two dimensions: two O sites per hole; one dimension: three O sites per hole). Therefore, the most important parameters in model (2.2) are Δ, U_d, and t_{pd}. For the same reason, the parameters U_p, V_{pd}, and t_{pp} are frequently neglected. Reference [74] contains a discussion of the influence of U_p and V_{pd} on the Cu $2p_{3/2}$ spectra of finite CuO_3 chain clusters. The authors concluded that the spectra are rather insensitive to these parameters. In the present thesis we will follow this line of reasoning, but

we will take account of the O-O hopping t_{pp}. Thus, we set $U_p = V_{pd} = 0$, and use the following simplified form of Hamiltonian (2.2)

$$H = H_0 + H_1 \ , \tag{2.6}$$

$$H_0 = \Delta \sum_{j\sigma} n^p_{j\sigma} + U_d \sum_i n^d_{i\uparrow} n^d_{i\downarrow} \ , \tag{2.7}$$

$$H_1 = t_{pd} \sum_{\langle ij\rangle\sigma} \phi^{ij}_{pd} \left(p^\dagger_{j\sigma} d_{i\sigma} + \text{h.c.} \right) + t_{pp} \sum_{\langle jj'\rangle\sigma} \phi^{jj'}_{pp}\, p^\dagger_{j\sigma} p_{j'\sigma} \ . \tag{2.8}$$

As standard set of parameters for Hamiltonian (2.6) we use [104] (again all values are in eV)

Δ	U_d	t_{pd}	t_{pp}
3.5	8.8	1.3	0.65

(2.9)

We now turn to the second term H_c in Eq.(2.1). H_c describes the interaction between the core and the valence holes. Since in experiments the best synchrotron flux is about 10^{12} photons per second while typical process times are 10^{-16} seconds, it is safe to assume that the core holes do not influence each other. Therefore, it suffices if H_c describes the interaction with a single core hole. We will include two contributions to H_c. First, there is a Coulomb repulsion U_{dc} between the Cu $2p_{3/2}$ core hole and the $3d$ valence holes on the core-hole site. Without loss of generality we may assume that this core-hole site is Cu site $i = 0$. Second, there is the interaction that leads to multiplet splitting. This interaction will be described by a Heisenberg-exchange term with an exchange constant I_{dc}. Thus, H_c reads

$$H_c = U_{dc} \sum_{\sigma\xi} n^d_{0\sigma} n^c_{0\xi} + I_{dc}\, \mathbf{S}^d_0 \cdot \mathbf{J}^c_0 \ . \tag{2.10}$$

$n^c_{0\xi}$ and $\mathbf{J}^c_0$ are the number operator and the pseudo-spin 3/2 operator of the Cu $2p_{3/2}$ core hole, with $\xi = \pm 3/2, \pm 1/2$ (see Sec. 6.2). $\mathbf{S}^d_0$ is the spin 1/2 operator of the Cu $3d$ valence hole. Notice that the on-site energy ϵ_{core} of the core hole, which is a constant, has been subtracted. In passing we note that the Cu $2p_{1/2}$ spectrum could be described by an analogous Hamiltonian, if $\mathbf{J}^c_0$ and $n^c_{0\xi}$ are replaced by the appropriate spin-1/2 quantities. In Eq.(2.10) the interaction between the core hole and the valence holes is described in a rather simple fashion. The multiplet splitting, for example, could be modelled in a more realistic way (see the references in Sec. 2.3). Furthermore, the Coulomb repulsion between core hole and valence holes will in reality not be restricted to the Cu site alone. Thus, an intersite Coulomb term U_{pc} between the core hole and the

neighbouring O valence holes might be added to H_c. However, the influence of U_{pc} on the Cu $2p_{3/2}$ spectra of finite CuO_3 chain clusters has been found to be rather small [74]. Therefore, Eq.(2.10) incorporates the essentials of the core hole - valence hole interaction. Furthermore, it has the advantage to describe valence-hole delocalization and multiplet splitting within one framework.

Summing up, in the hole notation the Hamilton operator that will be used in this thesis has the form (2.1)

$$H_{\rm XPS} = H + H_c \ .$$

H is multi-band model (2.6) which describes the valence holes of the CuO structures in absence of core holes, and at half filling (one valence hole per unit cell)

$$\begin{aligned} H &= H_0 + H_1 \ , \\ H_0 &= \Delta \sum_{j\sigma} n^p_{j\sigma} + U_d \sum_i n^d_{i\uparrow} n^d_{i\downarrow} \ , \\ H_1 &= t_{pd} \sum_{\langle ij\rangle\sigma} \phi^{ij}_{pd} \left(p^\dagger_{j\sigma} d_{i\sigma} + \text{h.c.} \right) + t_{pp} \sum_{\langle jj'\rangle\sigma} \phi^{jj'}_{pp} \, p^\dagger_{j\sigma} p_{j'\sigma} \ . \end{aligned}$$

As defined in Eq.(2.10), the term H_c describes the interaction between a Cu $2p_{3/2}$ core hole and valence holes on the same site $i = 0$

$$H_c = U_{dc} \sum_{\sigma\xi} n^d_{0\sigma} n^c_{0\xi} + I_{dc} \, \mathbf{S}^d_0 \cdot \mathbf{J}^c_0 \ .$$

To obtain this form, a constant energy ε_c has been subtracted that consists of the on-site energy $\epsilon_{\rm core}$ of the core-hole and the sum of all Cu on-site energies ϵ^d_i

$$\varepsilon_c = \epsilon_{\rm core} + \sum_i \epsilon^d_i \ . \tag{2.11}$$

This energy ε_c corresponds to a global shift of the calculated spectra. $H_{\rm XPS}$ contains six free parameters: the four parameters from H with standard values (2.9) in eV

Δ	U_d	t_{pd}	t_{pp}
3.5	8.8	1.3	0.65

and the two parameters U_{dc} and I_{dc} from H_c. These last two parameters will be obtained from the experiment in chapters 6 and 8. Finally, we note that $H_{\rm XPS}$ describes valence-hole delocalization and multiplet splitting within one framework.

2.2 Core-hole correlation function

Which microscopic quantity corresponds to the experimentally observed intensity? Within the Born approximation, the intensity $I(\omega)$, as a function of binding energy ω, is proportional to the Fourier transform of the time correlation function of core-hole creation and annihilation operators $c^\dagger_{0\xi}$, $c_{0\xi}$, i.e.

$$I(\omega) \sim \sum_\xi \mathrm{Re} \int_0^\infty dt\, e^{i(\omega+i\eta)t} \langle\Psi| c_{0\xi}\, c^\dagger_{0\xi}(-t) |\Psi\rangle \ . \tag{2.12}$$

The expression $i\eta$ symbolizes a limit $\eta \to 0$ which ensures convergence of the Fourier transform. $c^\dagger_{0\xi}$ creates a core hole at Cu site $i = 0$ with pseudo-spin 3/2 index ξ (see Sec. 2.1), where $\xi = \pm 1/2, \pm 3/2$. $|\Psi\rangle$ is the ground state before the creation of the core hole, that is the ground state of Hamiltonian H_{XPS} from Eq.(2.1) with ground-state energy E_G

$$H_{\mathrm{XPS}} |\Psi\rangle = (H + H_c) |\Psi\rangle = E_G |\Psi\rangle \ . \tag{2.13}$$

Notice that $|\Psi\rangle$ describes the system in the absence of core holes. Therefore, $|\Psi\rangle$ is an eigenstate of the core-hole part H_c from Eq.(2.10) with eigenvalue zero: $H_c |\Psi\rangle = 0$. Consequently, $|\Psi\rangle$ is the ground state of the valence part H from Eq.(2.6) as well

$$H |\Psi\rangle = E_G |\Psi\rangle \ . \tag{2.14}$$

In Eq.(2.12) we may use the same index ξ for both the core-hole creation and annihilation operator because the ground state $|\Psi\rangle$ is an eigenstate of the total number operator N_σ of valence holes with spin orientation σ. Thus, if a different core-hole pseudo spin ξ' is annihilated in Eq.(2.12) the resulting state does not belong to the same eigenspace of N_σ as the ground state, and the matrix element vanishes. Since the experiment does not allow to determine absolute intensities (see Fig. 1.9), we do not need to specify the proportionality factor in Eq.(2.12). In view of the fact that XPS measurements are usually carried out at room temperature, the use of the ground-state expectation value in Eq.(2.12) has to be motivated. The assumption that has been made here is that the difference between $T = 0$ K and $T = 300$ K should be insignificant in view of the typical width of the spectral features (Fig. 1.9) of the order 1 eV, i.e. 10000 K. Furthermore, as Cu $2p$ core-hole screening is a very local process (see Chap. 8), only the electronic configuration in the vicinity of the core-hole site is relevant. This local configuration should be roughly similar above and below the Néel temperature.

Next, Eq.(2.12) is reformulated in two different ways. First, we need the completeness relation in the $(N-1)$-electron subspace with one core hole

$$1^{(N-1)} = \sum_{\theta} |\theta\rangle \langle\theta| \ ,$$

where $|\theta\rangle$ are eigenstates of $H_{\rm XPS}$ (with eigenvalues E_θ) after the creation of the core hole

$$H_{\rm XPS} |\theta\rangle = E_\theta |\theta\rangle \ .$$

When this completeness relation is inserted, Eq.(2.12) leads to

$$\begin{aligned}
I(\omega) &\sim \sum_{\xi} \mathrm{Re} \int_0^\infty dt\, e^{i(\omega+i\eta)t} \langle\Psi| c_{0\xi}\, c_{0\xi}^\dagger (-t) |\Psi\rangle \\
&= \sum_{\xi} \mathrm{Re} \int_0^\infty dt\, e^{i(\omega+i\eta)t} \langle\Psi| c_{0\xi}\, e^{-itH_{\rm XPS}}\, c_{0\xi}^\dagger\, e^{itH_{\rm XPS}} |\Psi\rangle \\
&= \sum_{\xi} \mathrm{Re} \int_0^\infty dt\, e^{i(\omega+i\eta)t} \sum_{\theta} \langle\Psi| c_{0\xi}\, e^{-itH_{\rm XPS}} |\theta\rangle \langle\theta| c_{0\xi}^\dagger\, e^{itH_{\rm XPS}} |\Psi\rangle \\
&= \sum_{\xi} \mathrm{Re} \sum_{\theta} \langle\Psi| c_{0\xi} |\theta\rangle \langle\theta| c_{0\xi}^\dagger |\Psi\rangle \int_0^\infty dt\, e^{i(\omega+i\eta-E_\theta+E_G)t} \\
&= \sum_{\xi} \mathrm{Re} \sum_{\theta} \frac{i \left| \langle\theta| c_{0\xi}^\dagger |\Psi\rangle \right|^2}{\omega + i\eta - (E_\theta - E_G)} \\
&= \sum_{\xi} \sum_{\theta} \left| \langle\theta| c_{0\xi}^\dagger |\Psi\rangle \right|^2 \frac{\eta}{\left[\omega - (E_\theta - E_G)\right]^2 + \eta^2} \ ,
\end{aligned}$$

where E_G is the ground-state energy of $|\Psi\rangle$. Using

$$\lim_{\eta\to 0} \frac{\eta}{x^2+\eta^2} = \pi\, \delta(x) \ ,$$

and absorbing π into the proportionality factor we obtain

$$I(\omega) \sim \sum_{\xi} \sum_{\theta} \left| \langle\theta| c_{0\xi}^\dagger |\Psi\rangle \right|^2 \delta\left[\omega - (E_\theta - E_G)\right] \ . \tag{2.15}$$

Thus, the binding energy ω may be interpreted as the energy difference between the ground state $|\Psi\rangle$ of a N-electron system and the eigenstates $|\theta\rangle$ of a $(N-1)$-electron system. Equation (2.15) is especially useful when the eigenvectors $|\theta\rangle$ are known (see Chap. 6).

Another way to reformulate Eq.(2.12) consists in rewriting the core-hole creation operator in the Heisenberg picture

$$\begin{aligned} c_{0\xi}^{\dagger}(-t) &= e^{-itH_{\mathrm{XPS}}}\, c_{0\xi}^{\dagger}\, e^{itH_{\mathrm{XPS}}} \\ &= e^{-it\mathcal{L}_{\mathrm{XPS}}}\, c_{0\xi}^{\dagger}\ , \end{aligned} \tag{2.16}$$

where $\mathcal{L}_{\mathrm{XPS}}$ is the Liouville operator. It is defined for arbitrary operators A by

$$\mathcal{L}_{\mathrm{XPS}} A = [H_{\mathrm{XPS}}, A]\ . \tag{2.17}$$

Equation (2.16) can be easily proved using the corresponding equations of motion (that is, deriving both sides of Eq.(2.16) with respect to t). Using the Liouville operator we formally carry out the integration in Eq.(2.12) to obtain

$$\begin{aligned} I(\omega) &\sim \sum_{\xi} \mathrm{Re} \int_0^{\infty} dt\, e^{i(\omega+i\eta)t} \langle\Psi|\, c_{0\xi}\, c_{0\xi}^{\dagger}(-t)\, |\Psi\rangle \\ &= \sum_{\xi} \mathrm{Re} \int_0^{\infty} dt\ \langle\Psi|\, c_{0\xi}\, e^{it(\omega+i\eta-\mathcal{L}_{\mathrm{XPS}})}\, c_{0\xi}^{\dagger}\, |\Psi\rangle \\ &= \sum_{\xi} \mathrm{Re}\, \langle\Psi|\, c_{0\xi} \frac{i}{\omega+i\eta-\mathcal{L}_{\mathrm{XPS}}} c_{0\xi}^{\dagger}\, |\Psi\rangle \\ &= -\sum_{\xi} \mathrm{Im}\, \langle\Psi|\, c_{0\xi} \frac{1}{\omega+i\eta-\mathcal{L}_{\mathrm{XPS}}} c_{0\xi}^{\dagger}\, |\Psi\rangle\ . \end{aligned}$$

Thus, the intensity is proportional to the imaginary part of the single core hole correlation function G_{00}^{ξ}

$$I(\omega) \sim -\sum_{\xi} \mathrm{Im}\left[G_{00}^{\xi}(\omega+i\eta)\right]\ , \tag{2.18}$$

$$G_{00}^{\xi}(\omega+i\eta) = \langle\Psi|\, c_{0\xi} \frac{1}{\omega+i\eta-\mathcal{L}_{\mathrm{XPS}}} c_{0\xi}^{\dagger}\, |\Psi\rangle\ . \tag{2.19}$$

The poles of G_{00}^{ξ} (as a function of ω) correspond to the excitation energies of the system, the pole weights determine their contributions to the intensity. Equations (2.18) and (2.19) will be used for the calculation of XPS spectra in infinite systems (see Chap. 8). It follows from the structure of G_{00}^{ξ} that the calculation of the intensity involves the solution of two problems. First, one has to find an approximation for the ground state $|\Psi\rangle$ of Hamiltonian H_{XPS}, i.e. the ground state of the system before the creation of the core hole. As discussed above, $|\Psi\rangle$ is also ground state of Hamiltonian H from Eq.(2.6). This problem will be addressed in Part II of this thesis. Second, given $|\Psi\rangle$ one has to solve the dynamics $(\omega-\mathcal{L}_{\mathrm{XPS}})^{-1}$ after the creation of the core hole. This will be discussed in Part III. Before we proceed to solve these two problems, we shall give an overview of results obtained by other groups in the next section.

2.3 Previous results

The analysis of ground-state properties, as well as the investigation of Cu core-level XPS have been the subject of many publications, especially since the discovery of high-temperature superconductivity. In the following we try to give an overview of the works previously carried out by other groups on ground-state properties of Hamiltonian (2.2), and on Cu $2p$ core-level XPS in cuprates. With the present section we intend to offer the interested reader a brief chronological guide through the literature on the topics of this thesis. It can be skipped in a first reading.

2.3.1 Ground state

Due to its relevance for the high-T_c materials, model (2.2) has been studied mostly on CuO_2 planes. We begin by a short list of analytical approaches. In 1989, using a Hartree-Fock approximation and a Gutzwiller ansatz, Oles and Zaanen [77] calculated the Cu occupation number and the Cu magnetic moment as a function of the charge-transfer energy and the hole-doping. The doping dependence of these quantities has also been studied by Fedro and coworkers [33] in 1992. Using a mean-field approximation, they calculated the density of states, and compared their results to Quantum Monte Carlo calculations from Refs. [24] and [87]. In 1993, Luo and Bickers [62] used the fluctuation-exchange approximation (FLEX) to obtain the doping dependence of occupation numbers and the Néel temperature for the three-band model. Two years later, in 1995, Beatrici and Gusmão [7] obtained the density of states from perturbation theory around the atomic limit. Furthermore, they calculated the dependence of the magnetization on the doping concentration. In 1998, Sugihara, Ikeda, and Entel [93] analyzed the three-band model using a random-phase approximation. In qualitative agreement with experimental results [3], they found an asymmetry of the magnetic phase diagram with regard to electron vs. hole-doping. However, the theoretical Néel temperature was found to have its maximum at non-vanishing electron-doping. Recently, Maier and coworkers [65] investigated magnetic properties of the three-band model using dynamical mean-field theory. Again, the magnetic phase diagram was found to be asymmetric. Quantitatively, however, these results are still not satisfying, because the Néel temperature has its maximum at non-vanishing hole-doping, and its absolute value is too large.

Numerically, mostly exact diagonalization calculations and Quantum Monte Carlo simulations have been used to study model (2.2). In 1989, Stephan, von der Linden, and Horsch [92] performed exact diagonalizations of planar clusters con-

sisting of 2×2 plaquettes. In this way, occupation numbers and nearest-neighbour correlation functions were obtained. Quantum Monte Carlo simulations (using a grand-canonical ensemble) have been applied to a 4×4 plaquette system in 1990 by Dopf, Muramatsu, and Hanke [24]. They calculated occupation numbers, the magnetic structure factor, and other correlation functions. In 1991, Scalettar and coworkers [87] performed both exact diagonalization calculations (on a 2×2 plaquette cluster) and Quantum Monte Carlo simulations (4×4 plaquettes) to obtain occupation numbers as a function of doping and of the charge-transfer energy, as well as the magnetic structure factor and several susceptibilities. The spectral density for the three-band Hubbard model has been calculated in 1992 by Dopf and coworkers [25], using Quantum Monte Carlo for a system consisting of 4×4 plaquettes. In 1993, Bhattacharya and Wang [13] analyzed ground-state properties of Hamiltonian (2.2) on CuO_2 lattices using finite-temperature Monte Carlo and variational Monte Carlo. They analyzed the dependence of occupation numbers and the magnetic structure factor on the parameters t_{pp}, U_p, and V_{pd}, and on hole- and electron-doping. Finally, ground-state properties of Hamilton operator (2.2) on CuO_3 chain-clusters consisting of four plaquettes have been studied in 1997 by Drechsler, Málek, and Eschrig [27], using numerical exact diagonalization.

2.3.2 Cu $2p$ core-level XPS

In addition to the dominant main line, the Cu $2p$ core-level spectrum of many formally divalent Cu compounds – like CuF_2, $CuCl_2$, $CuBr_2$ [102], the high-T_c cuprates [36], [90], or CuO [90], [38] – shows a pronounced satellite structure. In analogy to an approach for metals by Kotani and Toyozawa in 1973 [58], Larsson and Braga [61], in 1977, assigned this satellite structure to a ("poorly screened") final state (denoted $3d^9$) in which the valence hole largely remains on the Cu site. In this way, the structure of the satellite could be explained by multiplet splitting due to the remaining d-hole. The main line was interpreted as originating from a final state in which the hole resides in the neighbouring ligands (denoted $3d^{10}\underline{\mathrm{L}}$).

Subsequently, in 1981 van der Laan and coworkers [102] corroborated this interpretation by an analysis based on a cluster approach in which the ground state is approximated by a superposition of the two states $3d^9$ and $3d^{10}\underline{\mathrm{L}}$. Models of this kind have been used by many other groups as well. For instance, Fujimori, Minami, and Sugano [35] in 1984, and Zaanen, Westra, and Sawatzky [112] in 1986 applied a cluster model to the valence-band photoemission of Ni compounds. In 1987, Shen and coworkers [90] used a cluster model to describe the spectra of several cuprates. In 1988, a cluster model has also been successfully applied to

CuO by Ghijsen and coworkers [38]. Furthermore, they showed that – in contrast to the divalent compounds – the closed-shell compound Cu_2O has no satellite and can be adequately described by one-electron band structure calculations.

Meanwhile, in 1984 Kakehashi, Becker, and Fulde [52] presented a purely theoretical analysis of core-level spectroscopy. In their model, valence electrons were described by one band, and exchange splitting was included in the form of a Heisenberg term. The spectra were calculated using Mori-Zwanzig projection technique (see Chap. 7). Later, in 1990, this method was applied by Becker, Brenig, and Fulde [10] to the valence band spectrum of the three-band model.

Another very popular model for the description of core-level spectroscopy is the single-site Anderson impurity model. In 1983 Gunnarsson and Schönhammer [42] [43] introduced this model for the study of Ce compounds, and applied it to calculate XPS, XAS (X-ray absorption spectroscopy), and BIS (bremsstrahlung isochromat spectroscopy). In 1989, using an impurity model with five filled bands, Okada and Kotani [71] analyzed the Cu $2p$ multiplet structure and its dependence on the hybridization in the spectra of La_2CuO_4 (measured by Nücker and coworkers [70]), and compounds from Ref.[102]. Later, in 1991, Tanaka, Okada, and Kotani [96] applied this model to other forms of spectroscopy, like X-ray emission spectroscopy (XES) and XAS. The doping dependence of the spectral weight in the high-T_c cuprates has been analyzed in 1991 by Eskes and Sawatzky [32] using an analogous model. In 1990, Eskes, Tjeng, and Sawatzky [31] had used this model to describe the spectrum of CuO. Furthermore, from their analysis these authors concluded that the influence of out-of-plane apex oxygens should be small. In contrast, Parmigiani and coworkers [81] showed in 1992 that the Cu $2p$ main line in copper oxides without apex-oxygen site (CuO, Nd_2CuO_4) is narrower than in compounds with one apex oxygen ($Bi_2Sr_2CaCu_2O_8$) or two apex oxygens (La_2CuO_4) per copper site. They attributed the additional spectral width to excitations into non-planar orbitals.

In particular, it is interesting to note that, in 1991, Parmigiani and coworkers [80] identified three substructures in the main line of the Cu $2p_{3/2}$ spectrum of $Bi_2Sr_2CaCu_2O_8$. An analogous substructure has been found in 1997 in the spectrum of $Sr_2CuO_2Cl_2$ [15], [16] (which will be analyzed in this thesis, see Secs. 8.2 and 8.3). In 1991, Tranquada and coworkers [99] measured the Cu $2p_{3/2}$ spectra of several compounds, including Bi_2CuO_4, and compared their results to unrestricted Hartree-Fock calculations for CuO_6 and CuO_{12} clusters. Both theoretically and experimentally, they found a positive correlation between the energy of the main line and the satellite to main-line intensity ratio I_s/I_m. The importance of the Cu valency for the strength of the satellite and the width of the main line was further underscored in 1992 by Karlsson, Gunnarsson, and

Jepsen [53] by means of a calculation within an impurity Anderson model. In 1994, Goldoni and coworkers [39] measured the Cu $2p_{3/2}$ spectrum of Bi_2CuO_4, and analyzed it in terms of an impurity cluster model. Another application of this model to the core-level spectra of high-T_c cuprates has been carried out by Chiaia and coworkers [19] in 1995.

Before 1993, the main line in the Cu $2p_{3/2}$ spectra had been attributed to a local $3d^{10}\underline{\mathrm{L}}$ excitation. However, this interpretation does not account for the asymmetry and the large width of the main line, which cannot be explained by experimental resolution or lifetime effects alone. Usually, this width had been associated with the oxygen bandwidth [43],[112]. Another proposal was a fluctuating charge state in which the bandwidth would be due to the superposition of several main lines, as suggested for CuO by Parmigiani and Samoggia [79] in 1988. It was the merit of van Veenendaal, Eskes, and Sawatzky [103],[104] to point out an alternative explanation in 1993. Using numerical exact diagonalization of a Cu_3O_{10} cluster (i.e. a chain of three plaquettes), these authors showed that the valence hole could delocalize further in the crystal. This leads to a lowest eigenstate of $3d^{10}$ character, in which the hole is mainly pushed out onto the neighbouring CuO_4 units, forming a Zhang-Rice singlet [113]. Furthermore, this approach led to more consistent values for the charge-transfer energy [104]. In 1994, van Veenendaal and Sawatzky [105] applied their model to a Cu_2O_7 cluster, including multiplet effects. An analogous approach was used by Tanaka and Jo [97] in 1997 to calculate the core level spectrum of a Cu_3O_{10} chain cluster.

Obviously, a screening due to surrounding CuO_4 units may lead to a dependence of the spectra on the geometry of the CuO network. This suggests the possibility of finite-size effects in cluster calculations. In fact, Okada and Kotani [72] showed in 1995 that there are differences between the spectra obtained by diagonalizing a Cu_5O_{16} chain cluster compared to a Cu_3O_{10} chain cluster. Furthermore, Ref. [72] contains cluster calculations for a planar Cu_5O_{16} cross-like cluster (see also Refs. [15] and [75]), and a short discussion of the influence of the (non-planar) Cu $3d_{3z^2-r^2}$ orbital in the presence of apical oxygens. In 1996, Okada and coworkers [73] measured the Cu $2p$ XPS of Sr_2CuO_3, and analyzed it using exact diagonalization of chain clusters with lengths of up to seven plaquettes (Cu_7O_{21}). The calculation for the largest cluster was found to be converged with respect to the system size. Okada and coworkers obtained a satisfactory agreement with the experimental results for a charge-transfer energy $\Delta = 2.5$ eV. The shoulder structure on the higher binding energy side of the main line was interpreted as being due to a final state of the following character: one half of the hole density pushed out from the core-hole site is transferred to the O sites just above and below the core-hole site, and the other half spreads over the

cluster. Consequently, the broad main-peak of Sr_2CuO_3 was attributed entirely to non-local screening.

In 1997, an analysis of spectral data for Sr_2CuO_3 by Maiti and coworkers [63],[64] using a configuration interaction model of a CuO_4 cluster resulted in an unusually small value for $\Delta \simeq 0.5$ eV. In the same year, Okada and Kotani [75] discussed the Cu $2p$ XPS of Bi_2CuO_4, Sr_2CuO_3, $Sr_2CuO_2Cl_2$, and other cuprates. They used exact diagonalization of edge-sharing chain clusters (Cu_5O_{12}), corner-sharing chain clusters (Cu_5O_{16}) and a Cu_5O_{16} cross-like cluster. More details about the chain calculations are given in a 1998 paper by the same authors [76]. These calculations will be compared with our results in chapters 6 and 8. Another paper by Okada and Kotani [74] from 1997 investigated the influence of intersite-Coulomb interactions V_{pd} and V_{pc} (see Sec. 2.1) on the spectrum of a Cu_4O_{12} chain cluster. They concluded that the influence of these parameters is small, especially as their effects seem to cancel each other out. Experimental work by Parmigiani and coworkers [82] in 1997 showed that the main line in the Cu $2p$ spectrum of $CuGeO_3$ consists of a single peak, similar to the one of Bi_2CuO_4 and Li_2CuO_2 (cf. Fig. 1.9). Also in 1997, Rosner and et al. [84] performed LDA band-structure calculations for Sr_2CuO_3 and Ca_2CuO_3. A fit of the result for Sr_2CuO_3 using an extended one-band Hubbard model resulted in a nearest-neighbour Cu-Cu hopping $t_1 = 0.55$ eV. Furthermore, magnetic properties of the two compounds were analyzed by means of an anisotropic Heisenberg model. Generally, the one-dimensional Heisenberg model has been successfully used to describe magnetic properties of Sr_2CuO_3 like, for instance, midinfrared optical absorption spectra (Suzuura and coworkers [94]), magnetic susceptibility (Motoyama, Eisaki, and Uchida [69]), or nuclear magnetic resonance (NMR) (Takigawa and coworkers [95]). For a discussion of exchange integrals in this compound see also the 1996 paper by Drechsler and coworkers [26].

The two publications by Böske et al. on the Cu $2p_{3/2}$ XPS of $Sr_2CuO_2Cl_2$ [15] and other model cuprates [16] have already been mentioned in Sec. 1.4, and in the following chapters we shall focus our attention on their results. These measurements have also been the topic of a recent theoretical study by Karlsson, Gunnarsson, and Jepsen [54] in which the Anderson impurity model has been used. Their conclusions will be discussed and compared to our results in chapters 6 and 8.

Part II

Ground state

Chapter 3

Basic ideas

In this chapter we describe the main properties of our approach towards the ground state $|\Psi\rangle$ of the multi-band Hamiltonian H from Eq.(2.6) at half-filling. This method has been published in Ref. [107]. A preliminary version can be found in Ref. [83]. In Sec. 3.1 we outline the general framework of the approach. It may be interpreted as a variational transformation of an approximate ground state $|\psi_0\rangle$ within the space spanned by certain fluctuation operators F_α. Thereby, variational parameters λ_α are used. As a demonstration, in Sec. 3.2 this formalism is applied to the (exactly solvable) problem of one hole on a single CuO_4 plaquette. This structure is the basic building block of all Cu-O networks that will be considered in the following (see Fig. 1.6). In Sec. 3.3 the relation between our approach and the cumulant formalism is discussed. Some advantages of the approach are presented in Sec. 3.4. One important result is that our formalism leads to exact solutions even in cases where naive perturbation theory would diverge.

3.1 General formalism for ground states

The formalism for ground states that we shall develop in the following consists of three basic ingredients. First, we need a state $|\psi_0\rangle$ that serves as a first approximation to the full ground state $|\Psi\rangle$. Second, we introduce fluctuation operators F_α that approximately transform $|\psi_0\rangle$ into the full ground state $|\Psi\rangle$. Third, there are fluctuation strengths λ_α corresponding to the operators F_α. These parameters λ_α will be determined from the condition that the resulting

state has to be an eigenstate of the Hamiltonian H of Eq.(2.6)

$$\begin{aligned} H &= H_0 + H_1 \ , \\ H_0 &= \Delta \sum_{j\sigma} n^p_{j\sigma} + U_d \sum_i n^d_{i\uparrow} n^d_{i\downarrow} \ , \\ H_1 &= t_{pd} \sum_{\langle ij\rangle\sigma} \phi^{ij}_{pd} \left(p^\dagger_{j\sigma} d_{i\sigma} + \text{h.c.} \right) + t_{pp} \sum_{\langle jj'\rangle\sigma} \phi^{jj'}_{pp} \, p^\dagger_{j\sigma} p_{j'\sigma} \ . \end{aligned}$$

Thus, the approach may be interpreted as a variational transformation of state $|\psi_0\rangle$ within the space spanned by the fluctuation operators F_α, using variational parameters λ_α.

Our main assumption about the ground state of H at half-filling is that each hole is localized within a small spatial region. This assumption is justified if the hopping part H_1 of Hamiltonian H is small compared to the atomic part H_0. It is, however, difficult to determine *a priori* under which circumstances H_1 is small enough to guarantee the local nature of the ground state. A local approach will be favoured if hopping parameters are small compared to on-site energy differences or Coulomb repulsions. Nevertheless, a perturbative treatment of the hopping may break down if it is based on a state in which the localization region of the holes is too small. This will be shown in Sec. 3.4 for the case of a single CuO_4 plaquette. For this reason we shall treat all fluctuations due to the hopping in a non-perturbative approximation. Fluctuations that lead beyond a certain spatial range will be neglected. Both the non-perturbative approximation and the neglect of far-reaching fluctuations will be justified *a posteriori*.

Since the ground state is predominantly of local character, we shall formulate the approach in position space. A natural choice for state $|\psi_0\rangle$ is the Néel-ordered ground state $|\psi_0\rangle$ of H_0

$$|\psi_0\rangle = \prod_i d^\dagger_{i,\sigma(i)} |0\rangle \ . \tag{3.1}$$

$|0\rangle$ is the 'vacuum' state (no holes), and $d^\dagger_{i,\sigma(i)}$ creates a hole on Cu site i, with spin $\sigma(i)$, depending on the site. Thus, in $|\psi_0\rangle$ every Cu site is singly occupied (with alternating spin direction) and all O sites are empty. As long as there are strong antiferromagnetic correlations a Néel-ordered state is a good starting point even if, like in the case of one dimension, the ground state does not possess long-range antiferromagnetic order [17].

For a non-vanishing hopping part of the Hamiltonian, $|\psi_0\rangle$ cannot be the full ground state because it does not contain charge fluctuations. These fluctuations are described by fluctuation operators F_α. For different geometries one needs different operators F_α. Therefore, we shall first outline the general way in which

the F_α enter the calculation, while their actual definition will be given later (see Secs. 3.2, 4.1, and Appendix A). Under quite general conditions it can be shown (see Sec. 3.3) that the transformation leading from $|\psi_0\rangle$ to the full ground state $|\Psi\rangle$ has to be of exponential form

$$|\Psi\rangle = \exp\left(\sum_\alpha \lambda_\alpha F_\alpha\right)|\psi_0\rangle \ . \tag{3.2}$$

From Eq.(3.2) all ground-state properties can be evaluated using

$$\langle A\rangle = \frac{\langle\Psi|\, A\,|\Psi\rangle}{\langle\Psi\mid\Psi\rangle} \ . \tag{3.3}$$

The ground-state energy, for instance, is calculated from Eq.(3.3) with $A = H$. The fluctuation strengths λ_α in Eq.(3.2) are determined using the following set of equations

$$0 = \langle\Psi|\left[H, F_\alpha^\dagger\right]|\Psi\rangle \ , \ \alpha = 1, 2, \ldots \qquad . \tag{3.4}$$

The r.h.s. of Eq.(3.4) depends on the fluctuation strengths λ_α, because they enter $|\Psi\rangle$ according to Eq.(3.2). Equation (3.4) follows from the condition that $|\Psi\rangle$ is an eigenstate of Hamiltonian H. If only a finite set of fluctuation operators F_α is used, Eq.(3.2) is only an approximate eigenstate of H. Compared to other conditions, Eq.(3.4) has several important advantages. This will be demonstrated not only for the evaluation of ground-state properties (Sec. 3.4), but also for the calculation of excitations (Sec. 7.3).

Due to the commutator on the r.h.s. of Eq.(3.4), only those contributions enter for which the F_α do not commute with the Hamiltonian. Thus, for fluctuation operators F_α that act on a limited spatial region all contributions from outside this region cancel. In a diagrammatic description this would correspond to the elimination of unconnected diagrams. It will guarantee that approximated extensive quantities (like the ground-state energy) still scale with system size, a property called *size consistency*. Furthermore, for the same reason the whole approach presented can equivalently be formulated in terms of cumulants. This relation to the cumulant formalism will be discussed in Sec. 3.3. Before, we shall apply the approach presented above to the (exactly solvable) problem of one hole on a single CuO_4 plaquette.

3.2 Application to a CuO_4 plaquette

In this section we use a one-particle problem – one hole on a single CuO_4 plaquette – to illustrate some features of the ground-state formalism that has been

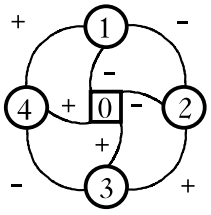

Figure 3.1: Definition of the phase factors ϕ_{pd}^{0j} and $\phi_{pp}^{jj'}$ for the CuO_4 plaquette.

introduced in Sec. 3.1. When applied to this system, the multi-band Hamiltonian (2.6) has the form $H = H_0 + H_1$, where

$$\begin{aligned} H_0 &= \Delta \sum_j n_j^p \ , \\ H_1 &= t_{pd} \sum_j \phi_{pd}^{0j} \left(p_j^\dagger d_0 + h.c \right) + t_{pp} \sum_{\langle jj' \rangle} \phi_{pp}^{jj'} \, p_j^\dagger p_{j'} \ . \end{aligned}$$

The Cu site is denoted by $i = 0$ while j and j' are the four O sites. There is only one hole, therefore the spin index has been suppressed. The phase factors ϕ_{pd}^{0j} and $\phi_{pp}^{jj'}$ are shown in Fig. 3.1.

The eigenvalue problem can be solved exactly. Since there are five sites, the system has five eigenstates. They are shown in Table 3.1. $|d\rangle$ is the state in which the hole is on the Cu site $i = 0$, and $|p_j\rangle$ are the states in which the hole is on O site j

$$\begin{aligned} |d\rangle &= d_0^\dagger \, |0\rangle \ , \\ |p_j\rangle &= p_j^\dagger \, |0\rangle \ . \end{aligned}$$

As always $|0\rangle$ denotes the "vacuum" state without holes. Furthermore $|p\rangle = \frac{1}{2} \left(|p_1\rangle + |p_2\rangle - |p_3\rangle - |p_4\rangle \right)$, and

$$E_\pm = \frac{1}{2} \left[\Delta - 2t_{pp} \pm \sqrt{\left(\Delta - 2t_{pp} \right)^2 + \left(4t_{pd} \right)^2} \right] . \tag{3.5}$$

Eigenstate	Norm	Eigenenergy
$\|E_-\rangle = 2t_{pd} \, \|d\rangle - E_- \, \|p\rangle$	$4t_{pd}^2 + (E_-)^2$	E_-
$\|E_+\rangle = 2t_{pd} \, \|d\rangle - E_+ \, \|p\rangle$	$4t_{pd}^2 + (E_+)^2$	E_+
$\|O_1\rangle = \|p_1\rangle - \|p_2\rangle + \|p_3\rangle - \|p_4\rangle$	4	Δ
$\|O_2\rangle = \|p_1\rangle + \|p_2\rangle + \|p_3\rangle + \|p_4\rangle$	4	Δ
$\|O_3\rangle = \|p_1\rangle - \|p_2\rangle - \|p_3\rangle + \|p_4\rangle$	4	$\Delta + 2t_{pp}$

Table 3.1: Eigenstates and eigenenergies of the single-plaquette system.

E_- is the ground-state energy of the system. Notice that E_- contains only a reduced effective charge-transfer energy $\Delta - 2t_{pp}$.

Let us now apply the formalism from Sec. 3.1 to this problem. The ground state (3.1) of H_0 is in this case just the state with pure Cu occupancy

$$|\psi_0\rangle = |d\rangle \ .$$

The fluctuations that transform this atomic ground state into the full ground state $|\Psi\rangle$ are charge fluctuations from the Cu to the four O sites. Since the ground state should have the same symmetry as the Hamiltonian, we may use a single fluctuation operator F_1 to describe these fluctuations, cf. Fig. 3.1

$$F_1 = -\sum_j \phi_{pd}^{0j} p_j^\dagger d_0 \ . \tag{3.6}$$

The minus sign in Eq.(3.6) has been introduced to guarantee a non-negative value of the fluctuation parameter λ_1 (see Eq.(3.10) and Sec. 4.1). According to Eq.(3.2), the full ground state of one hole on a single plaquette is given by

$$|\Psi\rangle = \exp\left(\lambda_1 F_1\right)|\psi_0\rangle \ . \tag{3.7}$$

The fluctuation strength λ_1 is determined from condition (3.4)

$$0 = \langle\Psi|\left[H, F_1^\dagger\right]|\Psi\rangle \ . \tag{3.8}$$

Since applying F_1 twice onto a singly occupied Cu site leads to zero, only terms up to order λ_1^2 contribute in Eq.(3.8)

$$\begin{aligned}\langle\Psi|\left[H, F_1^\dagger\right]|\Psi\rangle &= \langle\psi_0|\exp\left(\lambda_1 F_1^\dagger\right)\left[H, F_1^\dagger\right]\exp\left(\lambda_1 F_1\right)|\psi_0\rangle \\ &= \langle\psi_0|\left(1+\lambda_1 F_1^\dagger\right)\left[H, F_1^\dagger\right]\left(1+\lambda_1 F_1\right)|\psi_0\rangle \ .\end{aligned}$$

The first term $\left(HF_1^\dagger\right)$ of the commutator contributes only in order λ_1^2. It describes a process in which the hole first fluctuates from Cu to O and back via $F_1^\dagger F_1$. Then, the hole fluctuates a second time via $F_1^\dagger H$. Since there are four O sites, there are 16 different possibilities for this double fluctuation

$$\begin{aligned}\langle\psi_0|\left(1+\lambda_1 F_1^\dagger\right)HF_1^\dagger\left(1+\lambda_1 F_1\right)|\psi_0\rangle &= \lambda_1^2\langle\psi_0|F_1^\dagger H F_1^\dagger F_1|\psi_0\rangle \\ &= -16 t_{pd}\lambda_1^2 \ .\end{aligned}$$

The second part $\left(-F_1^\dagger H\right)$ of the commutator describes several processes. Either the hole fluctuates from Cu to O and back via $F_1^\dagger H$ (four possibilities), or from

	λ_1
$\Delta = 1.3$	0.500
$\Delta = 1.5$	0.481
$\Delta = 2.5$	0.398
$\Delta = 3.5$	0.331
$\Delta = 4.5$	0.279

Table 3.2: Fluctuation parameter λ_1 for the CuO_4 plaquette as a function of Δ.

Cu to O to another O and back via $F_1^\dagger H F_1$ (eight possibilities). In addition, there is a third process in which the hole moves from Cu to O – where H 'measures' the on-site energy Δ – and back via $F_1^\dagger H F_1$ (four possibilities)

$$\begin{aligned} -\langle\psi_0|\left(1+\lambda_1 F_1^\dagger\right) F_1^\dagger H\left(1+\lambda_1 F_1\right)|\psi_0\rangle &= -\langle\psi_0| F_1^\dagger H\left(1+\lambda_1 F_1\right)|\psi_0\rangle \\ &= 4t_{pd}+8t_{pp}\lambda_1-4\Delta\lambda_1 \ . \end{aligned}$$

If all terms are summed up, condition (3.8) assumes the form of a quadratic equation in λ_1

$$0 = t_{pd} - \left(\Delta - 2t_{pp}\right)\lambda_1 - 4t_{pd}\lambda_1^2 \ . \tag{3.9}$$

The positive solution is

$$\lambda_1 = \frac{\left(\Delta - 2t_{pp}\right) - \sqrt{\left(\Delta - 2t_{pp}\right)^2 + \left(4t_{pd}\right)^2}}{-8t_{pd}} \ . \tag{3.10}$$

If we use parameter set (2.9) with several different values for Δ, we obtain the λ_1-values in Table 3.2.

Equation (3.7), together with Eq.(3.10), is the exact ground state. This will be demonstrated by calculating the ground-state energy E_G and the Cu-occupation number $\langle n_{Cu}\rangle$. First we need the norm of state (3.7)

$$\begin{aligned} \langle\Psi \mid \Psi\rangle &= \langle\psi_0|\exp\left(\lambda_1 F_1^\dagger\right)\exp\left(\lambda_1 F_1\right)|\psi_0\rangle \\ &= \langle\psi_0|\left(1+\lambda_1 F_1^\dagger\right)\left(1+\lambda_1 F_1\right)|\psi_0\rangle \\ &= 1+4\lambda_1^2 \ . \end{aligned} \tag{3.11}$$

The ground-state energy is

$$\begin{aligned} E_G &= \frac{\langle\Psi|\, H\, |\Psi\rangle}{\langle\Psi \mid \Psi\rangle} \\ &= \frac{\langle\psi_0|\left(1+\lambda_1 F_1^\dagger\right) H\left(1+\lambda_1 F_1\right)|\psi_0\rangle}{1+4\lambda_1^2} \\ &= 4\lambda_1 \frac{\left(\Delta - 2t_{pp}\right)\lambda_1 - 2t_{pd}}{1+4\lambda_1^2} \ . \end{aligned}$$

Using Eq.(3.9) this expression can be transformed to give

$$E_G = 4\lambda_1 \frac{t_{pd} - 4t_{pd}\lambda_1^2 - 2t_{pd}}{1+4\lambda_1^2} = -4t_{pd}\lambda_1 \ . \tag{3.12}$$

Together with Eq.(3.10) this gives the exact ground-state energy E_- (see Eq.(3.5)); the negative solution for λ_1 gives E_+. Notice that we could have obtained this result more easily using the "mixed average"

$$E_G = \frac{\langle\psi_0|\, H\, |\Psi\rangle}{\langle\psi_0 \mid \Psi\rangle} \tag{3.13}$$

instead of Eq.(3.3). In fact

$$E_G = \frac{\langle\psi_0|\, H\, |\Psi\rangle}{\langle\psi_0 \mid \Psi\rangle} = \lambda_1 \langle\psi_0|\, H F_1\, |\psi_0\rangle = -4t_{pd}\lambda_1 \ .$$

However, in general the "shortcut" Eq.(3.13) leads to the same value for the ground-state energy as Eq.(3.3) only if $|\Psi\rangle$ is the exact ground state. On the other hand, as demonstrated above, Eq.(3.13) is much easier to evaluate. Therefore, in the following we will calculate ground-state energies using Eq.(3.13) instead of Eq.(3.3), even if $|\Psi\rangle$ is not the exact ground state.

The Cu occupation number $\langle n_{Cu}\rangle$ is the probability of finding the hole on the Cu site

$$\begin{aligned} \langle n_{Cu}\rangle &= \frac{\langle\Psi|\, n_d\, |\Psi\rangle}{\langle\Psi \mid \Psi\rangle} \\ &= \frac{\langle\psi_0|\left(1+\lambda_1 F_1^\dagger\right) n_d \left(1+\lambda_1 F_1\right)|\psi_0\rangle}{\langle\Psi \mid \Psi\rangle} \\ &= \frac{1}{\langle\Psi \mid \Psi\rangle} \\ &= \frac{1}{1+4\lambda_1^2} \ , \end{aligned} \tag{3.14}$$

which is again the exact result.

Summarizing, the application to the problem of a single CuO_4 plaquette shows that the formalism of Sec. 3.1 is an efficient tool for the calculation of ground-state properties. Further properties of the approach will be discussed in the following two sections.

3.3 Relation to the cumulant formalism

There is a close relation between the approach described in Sec. 3.1 and the cumulant formalism [8]. First, let us briefly repeat the basic concepts and statements of the cumulant formalism. The cumulant expectation value [59] of a product of operators A_i, with $i = 1, \ldots N$, for two states $|\varphi\rangle$ and $|\chi\rangle$ is defined by

$$\langle\varphi| A_1 \cdots A_N |\chi\rangle^c = \frac{\partial}{\partial\alpha_1} \cdots \frac{\partial}{\partial\alpha_N} \ln \langle\varphi| e^{\alpha_1 A_1} \ldots e^{\alpha_N A_N} |\chi\rangle \Big|_{\alpha_1=\ldots=\alpha_N=0} .$$

Here and in the following we always assume that the states involved in a cumulant have non-vanishing overlap, i.e. $\langle\varphi \mid \chi\rangle \neq 0$. For $N = 1$ the cumulant is just the usual expectation value divided by $\langle\varphi \mid \chi\rangle$. For $N > 1$ the cumulant is a linear combination of different factorizations of this expectation value. For example, for $N = 2$

$$\langle\varphi| A_1 A_2 |\chi\rangle^c = \frac{\langle\varphi| A_1 A_2 |\chi\rangle}{\langle\varphi \mid \chi\rangle} - \frac{\langle\varphi| A_1 |\chi\rangle \langle\varphi| A_2 |\chi\rangle}{\langle\varphi \mid \chi\rangle^2} .$$

When writing down a cumulant expression one has to determine which of the operators are subjected to the factorization process. In the following, if not indicated otherwise, all operators appearing within a cumulant are treated as separate entities with respect to the cumulant ordering. These operators are called *prime* operators, as opposed to *composite* operators which are products of prime operators [88]. The following identity [56] holds for any prime operator F and any (prime or composite) operator A

$$\langle\varphi| e^{F^\dagger} A e^F |\chi\rangle^c = \left\langle e^F\varphi\right| A \left|e^F\chi\right\rangle^c . \tag{3.15}$$

This equation allows to remove the exponential functions from the cumulant ordering and apply them directly onto the states. Finally, we note that one of the attractive features of cumulants is that they preserve size consistency [89].

The cumulant formalism for the calculation of ground-state properties may now be formulated as follows. By application of a (composite) operator Ω within the cumulant ordering, an approximate ground state $|\psi_0\rangle$ can be mapped onto the

full ground state $|\Psi\rangle$. Notice that in general Ω depends on $|\psi_0\rangle$. If one assumes that Ω can be represented by a universal analytic function of a prime operator, it follows [88] that Ω is of exponential form

$$|\Psi\rangle^c = \Omega\,|\psi_0\rangle^c = \exp\left(\sum_\alpha \lambda_\alpha F_\alpha\right)|\psi_0\rangle^c \quad . \tag{3.16}$$

Here, the exponential function should be understood in terms of a series expansion in which the first term (unity) is *not* subjected to the cumulant ordering. From Eq.(3.16) ground state properties can be calculated using

$$\langle A\rangle = \langle\varphi|\,A\Omega\,|\psi_0\rangle^c \quad , \tag{3.17}$$

with an arbitrary state $|\varphi\rangle$. The parameters λ_α in Eq.(3.16) are determined using the following set of equations [88]

$$0 = \langle\varphi|\,F_\alpha^\dagger H\Omega\,|\psi_0\rangle^c \tag{3.18}$$

for all α. Equation (3.18) follows [56] from the condition that $\Omega\,|\psi_0\rangle^c$ is an eigenstate of H.

Next we demonstrate the relation between the above equations and Eqs.(3.2), (3.3), and (3.4). If we choose $|\varphi\rangle = \Omega\,|\psi_0\rangle$ and use Eq.(3.15) we can directly transform Eq.(3.16) into Eq.(3.2), as well as Eq.(3.17) into Eq.(3.3). On the other hand, Eq.(3.4) is equivalent to a linear combination of Eq.(3.18) and its analogue with F_α instead of $F_\alpha^\dagger$

$$0 = \langle\varphi|\,F_\alpha H\Omega\,|\psi_0\rangle^c \quad . \tag{3.19}$$

Notice that, if $\Omega\,|\psi_0\rangle^c$ is an exact eigenstate of H, Eqs.(3.18) and (3.19) are equivalent. If, however, $\Omega\,|\psi_0\rangle^c$ is an approximate eigenstate of H it is possible that only one set of equations is fulfilled. This means that one may find (slightly) different values for the parameters λ_α if one uses Eq.(3.18) or Eq.(3.19) or some linear combination of both. In other words, the approximate ground state depends on the form of the equations for the determination of the λ_α. We now choose $|\varphi\rangle = \Omega\,|\psi_0\rangle$ in Eqs.(3.18) and (3.19), and we use Eq.(3.15) to obtain

$$\begin{aligned} 0 &= \langle\Omega\psi_0|\,F_\alpha^\dagger H\,|\Omega\psi_0\rangle^c \quad , \\ 0 &= \langle\Omega\psi_0|\,F_\alpha H\,|\Omega\psi_0\rangle^c \quad . \end{aligned}$$

Subtracting the first equation from the complex conjugate of the second equation leads to Eq.(3.4)

$$\begin{aligned} 0 &= \langle\Omega\psi_0|\,H F_\alpha^\dagger\,|\Omega\psi_0\rangle^c - \langle\Omega\psi_0|\,F_\alpha^\dagger H\,|\Omega\psi_0\rangle^c \\ &= \langle\Omega\psi_0|\left[H, F_\alpha^\dagger\right]|\Omega\psi_0\rangle \quad , \end{aligned}$$

where we have assumed that $|\Omega\psi_0\rangle$ is normalized. Since a commutator is always a prime operator within the cumulant ordering [56], the last expression is a simple expectation value. Note that the factorizing terms are now removed by the commutator, instead of the cumulant, which guarantees size consistency.

Summing up, the approach presented in Sec. 3.1 is a specific version of the cumulant formalism. In the next section we shall discuss some of its advantages.

3.4 Advantages

As we have seen in the preceding section, within the cumulant formalism the approach presented in Sec. 3.1 amounts to the following procedure. One applies the operator Ω onto both the bra- and ket-vector, transfers Ω out of the cumulant ordering with Eq.(3.15), and determines the values of the fluctuation parameters using a linear combination of Eqs.(3.18) and (3.19).

What difference does this make in comparison to other possible versions of Eqs.(3.16), (3.17), and (3.18)? For instance, one might choose $|\varphi\rangle = |\psi_0\rangle$, or, if $|\varphi\rangle = \Omega\,|\psi_0\rangle$, one might leave the operator Ω within the cumulant ordering.

To answer this question, let us first apply the cumulant formalism with $|\varphi\rangle = |\psi_0\rangle$ to the problem of a single CuO_4 plaquette from Sec. 3.2. In this case, Eq.(3.18) leads to the same quadratic equation (3.9), and to the same (exact) formula (3.12) for the ground-state energy as the approach from Sec. 3.1. This is due to the fact that the operator Ω appears only once in each expression, which leads to a truncation of the exponential function in λ_1. However, since $|\varphi\rangle = |\psi_0\rangle$, Eq.(3.17) gives an incorrect result for the Cu occupation number: $\langle n_{Cu}\rangle = 1$, independent of λ_1. The reason for this failure is that there are no operators to the left of n_d which could remove the fluctuations created by Ω. Therefore, the influence of fluctuations on $\langle n_{Cu}\rangle$ is completely neglected.

This problem does not occur if $|\varphi\rangle = \Omega\,|\psi_0\rangle$, because in this case the operator Ω appears twice in the cumulant

$$\langle n_{Cu}\rangle = \langle\psi_0|\,\Omega^\dagger n_d \Omega\,|\psi_0\rangle^c \quad .$$

Now, however, the exponential functions in λ_1 do not truncate. Instead, when the cumulants are evaluated the following infinite power series results

$$\langle n_{Cu}\rangle = 1 - 4\lambda_1^2 + 16\lambda_1^4 - 64\lambda_1^6 \pm \ldots \quad .$$

This is just the series expansion of the exact result (3.14)

$$\langle n_{Cu}\rangle = \frac{1}{1+4\lambda_1^2} \quad .$$

The expansion diverges for $\lambda_1 \geq 0.5$ (that is, for values of λ_1 that are still smaller than 1). This demonstrates that a perturbative treatment of F_1 fluctuations (i.e. an expansion in λ_1) is in general *not* possible. This should apply not only to the case of a single plaquette but also to infinite systems, in which charge fluctuations are even stronger (see Sec. 4.4). Notice that, typically, λ_1 is of the order 1/2 (see Table 3.2).

Thus, the transfer of operator Ω from the cumulant ordering into the state using Eq.(3.15) amounts to a *summation of all orders* in λ_1. In this sense the approach of Sec. 3.1 goes beyond the cumulant formalism as it is applicable even if – for the given state $|\psi_0\rangle$ – the operator Ω does not exist in the cumulant ordering, like in the case above for $\lambda_1 \geq 0.5$. The divergence of the series expansion for $\lambda_1 = 0.5$ may now be interpreted as follows. Condition $\lambda_1 = 0.5$ is equivalent to a vanishing effective charge-transfer energy $\Delta - 2t_{pp} = 0$, cf. Eqs.(3.5) and (3.9). Therefore, the series diverges when the O sites (effectively) become energetically equal to the Cu site. This can also be seen from the fact that the Cu-occupation number drops to 1/2 precisely when λ_1 reaches the value 0.5. The divergence in λ_1 has been observed previously [10], although its origin was unclear at that time. From a more formal point of view the divergence occurs when the condition [89]

$$|\langle \psi_0 \mid \Psi \rangle| > 1/2$$

is violated. All these equivalent conditions describe the same phenomenon: state $|\psi_0\rangle$ ceases to be a good approximation of $|\Psi\rangle$. These difficulties do not occur in the approach of Sec. 3.1 in which independent of state $|\psi_0\rangle$ all orders in λ_1 are exactly summed up. Further advantages of this approach will become clear when we approximate ground states of infinite systems in the following chapter.

Chapter 4

Infinite systems

In the following we apply the formalism of chapter 3 to infinite systems. The model system that we shall consider throughout this chapter is an infinite, half-filled CuO_2 plane. The CuO_3 chain is discussed in Appendices A and B. The CuO_2 plane has been chosen as an example because it has a high symmetry which will make our calculations more transparent. In addition, this system is of great interest in itself because CuO_2 planes are the essential structural part of all high-T_c superconducting compounds. In Sec. 4.1 we define the fluctuation operators F_α for the CuO_2 geometry. They allow for a multitude of so-called many-body effects which make an exact evaluation of expectation values impossible. Therefore, it is necessary to make approximations. They are introduced in Sec. 4.2, and used to calculate several expectation values in Sec. 4.3. Finally, the fluctuation parameters λ_α are determined in Sec. 4.4. The λ_α are found to decrease rapidly with increasing length of the fluctuation process.

4.1 Fluctuation operators

In this section we define the fluctuation operators for an infinite CuO_2 plane. First, operator F_1 from Eq.(3.6) is generalized to all N Cu sites i

$$F_{i,1} = -\sum_{j\sigma} \phi_{pd}^{ij} p_{j\sigma}^\dagger d_{i\sigma} \ , \tag{4.1}$$

where the sum is again over the four O sites that surround the Cu site i (see also Fig. 4.1). The remaining operators are constructed in accordance with the following principles: (i) All operators describe delocalizations of a hole initially located at Cu site i. (ii) The final site in the process is reached via the shortest path accessible by Cu-O hopping processes. (iii) A summation over all equivalent final sites is made. (iv) The signs of the hopping processes are chosen to be the

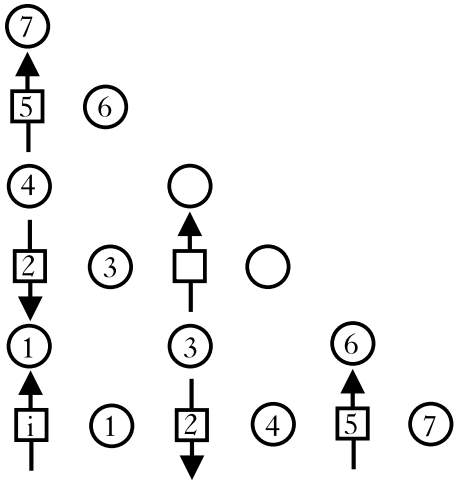

Figure 4.1: Final sites reached by fluctuation operators $F_{i,\alpha}$, with $\alpha = 1, \ldots 7$. For reasons of symmetry only one quarter of the allowed fluctuation range is shown.

negative of the phases ϕ_{pd}^{ij} in the multi-band Hamiltonian (2.6). The point of this last principle is to allow for an easy determination of the sign with which a given process contributes to an expectation value (see Sec. 4.4). In addition, one is led to non-negative values for the fluctuation strengths λ_α. The summation over equivalent final sites, together with the phase convention (iv), generates a ground state which has the same symmetry as the Hamiltonian. Figure 4.1 shows final sites reached by fluctuation operators $F_{i,\alpha}$, with $\alpha = 1, \ldots 7$. For reasons of symmetry only one quarter of the allowed fluctuation range is shown. The fluctuation operators are defined as follows

$$F_{i,2} = -\sum_{jk\sigma} d_{k\sigma}^\dagger \left(1 - n_{j\sigma}^p\right) d_{i\sigma} \ , \tag{4.2}$$

$$F_{i,3} = \sum_{jkl\sigma} \phi_{pd}^{kl}\, p_{l\sigma}^\dagger \left(1 - n_{k\sigma}^d\right) \left(1 - n_{j\sigma}^p\right) d_{i\sigma} \ , \tag{4.3}$$

$$F_{i,4} = \sum_{jkm\sigma} \phi_{pd}^{km}\, p_{m\sigma}^\dagger \left(1 - n_{k\sigma}^d\right) \left(1 - n_{j\sigma}^p\right) d_{i\sigma} \ . \tag{4.4}$$

j denotes the O sites between the two Cu sites i and k. The indices l , m label O sites on the nearest neighbour plaquettes (see Fig. 4.2). The expressions in brackets – e.g. $\left(1 - n_{j\sigma}^p\right)$ – make sure that the way to the final site of the fluctuation is not blocked by a hole with the same spin direction. Notice that the general phase factor for a nearest-neighbour Cu-Cu hopping is independent of the direction: $\phi_{pd}^{kj}\phi_{pd}^{ij} = -1$ (cf. Fig. 4.2).

Final states with doubly occupied Cu sites differ by the Coulomb energy U_d

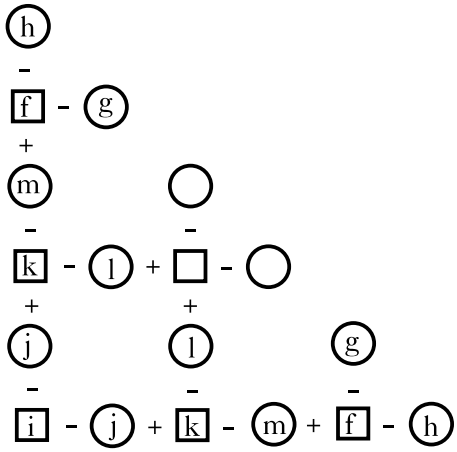

Figure 4.2: Labelling of Cu and O sites.

from states with singly occupied Cu sites. Since U_d is large, we have to distinguish between these two cases. Therefore, we further split $F_{i,2}$ into two operators that describe a process leading to a singly or a doubly occupied Cu site k, respectively (s stands for singly occupied, d for doubly occupied)

$$F_{i,2s} = -\sum_{jk\sigma} \left(1 - n^d_{k\overline{\sigma}}\right) d^\dagger_{k\sigma} \left(1 - n^p_{j\sigma}\right) d_{i\sigma} \ , \tag{4.5}$$

$$F_{i,2d} = -\sum_{jk\sigma} n^d_{k\overline{\sigma}} d^\dagger_{k\sigma} \left(1 - n^p_{j\sigma}\right) d_{i\sigma} \ , \tag{4.6}$$

where $\overline{\sigma}$ is $-\sigma$. Note that it is not necessary to introduce a fluctuation operator that leads to the nearest neighbor Cu sites in diagonal direction (e.g. the Cu site without a label in Fig. 4.1.). Due to the Pauli principle, fluctuations to these sites are largely suppressed because of antiferromagnetic order. The neglect of fluctuations that lead beyond the range shown in Fig. 4.1. will be justified *a posteriori*. In Sec. 4.4 we will show that the fluctuation strengths λ_α decrease rapidly with increasing length of the fluctuation processes. Therefore, the range covered by the operators $F_{i,1}, \ldots F_{i,4}$ defined above is already sufficiently large for a good description of delocalization effects in the ground state. To demonstrate this, in Sec. 4.4 and Appendix A we will use fluctuation operators that have a range even beyond the next-nearest neighbour plaquette

$$F_{i,5} = \sum_{jkmf\sigma} d^\dagger_{f\sigma} \left(1 - n^p_{m\sigma}\right) \left(1 - n^d_{k\sigma}\right) \left(1 - n^p_{j\sigma}\right) d_{i\sigma} \ , \tag{4.7}$$

$$F_{i,6} = -\sum_{jkmfg\sigma} \phi^{fg}_{pd} \, p^\dagger_{g\sigma} \left(1 - n^d_{f\sigma}\right) \left(1 - n^p_{m\sigma}\right) \left(1 - n^d_{k\sigma}\right) \left(1 - n^p_{j\sigma}\right) d_{i\sigma} \ , \tag{4.8}$$

$$F_{i,7} = -\sum_{jkmfh\sigma} \phi_{pd}^{fh}\, p_{h\sigma}^{\dagger} \left(1 - n_{f\sigma}^{d}\right) \left(1 - n_{m\sigma}^{p}\right) \left(1 - n_{k\sigma}^{d}\right) \left(1 - n_{j\sigma}^{p}\right) d_{i\sigma} \ . \tag{4.9}$$

Here, f denotes the next-nearest Cu sites, and g and h are O sites on the next-nearest plaquettes (see Fig. 4.2). The general phase factor for a next-nearest neighbour Cu-Cu hopping again does not depend on the direction

$$\phi_{pd}^{fm}\, \phi_{pd}^{km}\, \phi_{pd}^{kj} \phi_{pd}^{ij} = 1 \ .$$

Next, the operators $F_{i,\alpha}$ are applied onto the state $|\psi_0\rangle$ from Eq.(3.1). This requires several approximations which will be discussed in the following section.

4.2 Approximations

In this section we approximate the ground state of a half-filled, infinite CuO_2 plane using the fluctuation operators $F_{i\alpha}$ that have been defined in Sec. 4.1. Following the reasoning of Sec. 3.1, our ground-state ansatz has an exponential form

$$|\Psi\rangle = \exp\left(\sum_{i\alpha} \lambda_\alpha F_{i\alpha}\right) |\psi_0\rangle \ , \tag{4.10}$$

cf. Eq.(3.2). The sum in Eq.(4.10) is over all Cu sites i and all fluctuation operators α. $|\psi_0\rangle$ is the Néel-ordered ground state of H_0

$$|\psi_0\rangle = \prod_i d_{i,\sigma(i)}^{\dagger} |0\rangle \ . \tag{4.11}$$

$|\psi_0\rangle$ is shown in Fig. 4.3. Due to translational symmetry the fluctuation strengths λ_α in Eq.(4.10) do not depend on the Cu-site index i. The values of the λ_α are determined using Eq.(3.4) for an arbitrary site $i = 0$

$$0 = \langle\Psi| \left[H, F_{0,\alpha}^{\dagger}\right] |\Psi\rangle \ , \ \alpha = 1, 2, \ldots \quad . \tag{4.12}$$

Unfortunately, Eq.(4.10) is far too complicated to allow for the exact calculation of expectation values like those in Eq.(4.12). Therefore, further approximations are necessary. All following approximations are based on the assumption that the strengths of far-reaching fluctuations $F_{i,\alpha>0}$ from Eqs.(4.2)-(4.9) are small compared to the strength of the on-plaquette fluctuation $F_{i,1}$ from Eq.(4.1). This means we assume that the ground state is of mainly local nature. To simplify

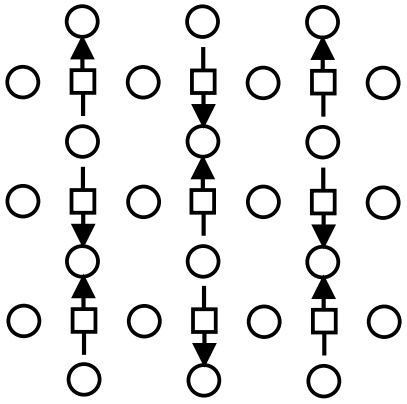

Figure 4.3: The Néel-ordered ground state $|\psi_0\rangle$.

Eq.(4.10) we approximately factorize the exponential function with respect to fluctuations $F_{i\alpha}$ ($\alpha > 1$) and $F_{i',1}$

$$|\Psi\rangle = \exp\left(\sum_{i,\alpha>1} \lambda_\alpha F_{i\alpha}\right) \exp\left(\sum_{i'} \lambda_1 F_{i',1}\right) |\psi_0\rangle \ . \tag{4.13}$$

This approximation amounts to the assumption that far-reaching fluctuations $F_{i,\alpha>1}$ occur on the background of $F_{i,1}$-fluctuations, which in turn are influenced only indirectly (i.e. via λ_1) by the former. The second exponential function in Eq.(4.13) can be exactly rewritten as a product with respect to i'

$$|\Psi\rangle = \exp\left(\sum_{i,\alpha>1} \lambda_\alpha F_{i\alpha}\right) \prod_{i'} (1 + \lambda_1 F_{i',1}) |\psi_0\rangle \ . \tag{4.14}$$

Here we have used the fact that the $F_{i,1}$-fluctuations, when applied to $|\psi_0\rangle$, cannot create double occupancies on Cu sites. Thus, they do not lead to correlation effects. Moreover, due to the Néel-order of state $|\psi_0\rangle$, the ranges on which holes with equal spin delocalize via $F_{i,1}$-fluctuations do not overlap. Therefore, it does not matter in which order the $F_{i,1}$-fluctuations take place. Then, the exponential function in Eq.(4.13) is equivalent to the product in Eq.(4.14). As in the case of the single CuO_4 plaquette (Sec. 3.2), only terms up to order λ_1^2 contribute, since applying F_1 twice onto a singly occupied Cu site leads to zero.

In Eq.(4.14) every hole may fluctuate over a total range of five plaquettes (or even nine plaquettes, if we include fluctuation operators with $\alpha > 4$). Notice that all holes fluctuate simultaneously. This leads to a multitude of *many-body effects*[1]. Basically there are three types of many-body effects. They are exempli-

[1] In this thesis we mean by a many-body effect the case when the fluctuation of a hole is influenced by the configuration of other holes.

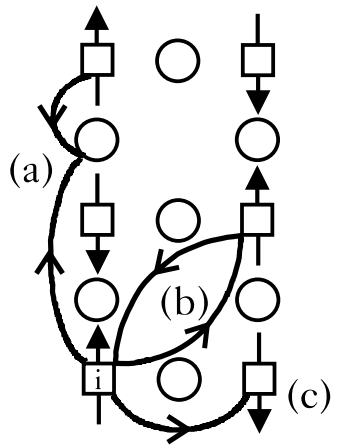

Figure 4.4: Examples for many-body effects. There are three types of effects: (a) processes that are excluded by the Pauli principle, (b) site-changing processes, and (c) correlations due to the Hubbard U_d on doubly occupied Cu sites.

fied in Fig. 4.4. First, due to the Pauli principle the fluctuation of a hole may be blocked by the presence of other holes with the same spin, as in the fluctuation process labelled (a) in Fig. 4.4. Second, there are processes in which holes with the same spin direction change their place, cf. process (b). In the following we will call these processes *site-changing processes*. Third, there are strong correlations due to the Hubbard U_d on doubly occupied Cu sites, as in process (c). One common feature of all these many-body effects is that they suppress fluctuations (see Sec. 4.3). This multitude of many-body effects makes an exact evaluation of expectation values using Eq.(4.14) impossible. Further approximations are therefore necessary. Let us consider processes in which two or more holes simultaneously leave their original plaquette. The fluctuation strengths λ_α for such far-reaching fluctuations turn out to be small compared to λ_1. Therefore, it should be possible to neglect the many-body effects arising in these processes (except for site-changing processes in diagonal direction, see below). Let us take the case of $F_{i,2d}$ fluctuations as an example. For these fluctuations we neglect the possibility that the O site j between the starting and final Cu sites i and k (see Fig. 4.2) may already be occupied by a hole with the same spin. This amounts to the following simplification

$$F_{i,2d} = -\sum_{jk\sigma} n^d_{k\overline{\sigma}} d^\dagger_{k\sigma} d_{i\sigma} \ ,$$

instead of Eq.(4.6). In this way all of the aforementioned processes are included, some of them however only in a simplified way (i.e. by neglecting some of the many-body effects). Notice that the neglect of many-body effects allows for

unphysical fluctuations that may decrease the calculated ground-state energy below the exact value. Thus, no upper limit to the exact ground-state energy is guaranteed (see Sec. 5.3). Furthermore, no spin-flip effects are included, as these occur only in processes in which two holes (with opposite spins) simultaneously leave their original plaquette. Thus, we cannot expect our approach to give a detailed description of magnetic properties.

In addition to all many-body effects that are due to processes where only one hole leaves its original plaquette, we take account of all site-changing processes in diagonal direction. One of these processes is shown in Fig. 4.4(b). It is not necessary to introduce a special fluctuation operator for this process, because it can be described by the operators $F_1$and F_3. In Sec. 4.4 the suppression of charge fluctuations due to the diagonal sites will be shown to be important. On the other hand, site-changing processes involving next-nearest Cu neighbours in horizontal or vertical direction (Cu sites i and f in Fig. 4.2) can be neglected. This has the following reason: During these processes the paths of the holes have to cross at the intermediate O sites (sites j and m in Fig. 4.2). However, since the holes have the same spin, they have to avoid each other due to the Pauli principle. Site-changing processes in horizontal or vertical direction are therefore unlikely.

4.3 Calculation of expectation values

The approximations described in Sec. 4.2 may be summarized in short: We neglect many-body effects arising in processes for which two or more holes simultaneously leave their original plaquette. Following this reasoning we now evaluate expectation values. Our first example is the calculation of the norm $\langle \Psi \mid \Psi \rangle$ of state (4.14)

$$\langle \Psi \mid \Psi \rangle = \left(1 + \sum_{\alpha} z_\alpha p_\alpha \lambda_\alpha^2 \right)^N = \nu^N \ . \tag{4.15}$$

A derivation of this result will be given below. N is the number of holes (which is at half filling equal to the number of Cu sites). z_α is the number of equivalent final sites of the given process (see Fig. 4.1)

$$\begin{aligned} z_1 &= 4 \quad , \quad z_{2s} = 4 \quad , \\ z_{2d} &= 4 \quad , \quad z_3 = 8 \quad , \quad z_4 = 4 \ . \end{aligned} \tag{4.16}$$

p_α is the probability that the configuration of the other holes makes the process possible. This probability is defined by

$$p_\alpha = \frac{\langle\Psi| P_{i,\alpha} |\Psi\rangle}{\langle\Psi \mid \Psi\rangle} \ , \tag{4.17}$$

where $P_{i,\alpha}$ is a projection operator on all configurations that allow for process α. For example, $P_{i,2s}$ projects on states in which the target Cu site of fluctuation $F_{i,2s}$ (site k in Fig. 4.2) is empty, whereas $P_{i,2d}$ is the projector on states with a singly occupied final site. Due to translational symmetry, the probabilities p_α do not depend on the site index i. Obviously, Eqs.(4.15) and (4.17) have to be solved self-consistently since $|\Psi\rangle$ in Eq.(4.17) depends on the parameters λ_α. In particular, one obtains

$$\begin{aligned} p_1 &= 1 \quad , \quad p_{2s} = 1 - 1/\nu \quad , \quad p_{2d} = 1/\nu \\ p_3 &= 1 - 2\lambda_1^2/\nu \quad , \quad p_4 = 1 - \lambda_1^2/\nu \ . \end{aligned} \tag{4.18}$$

The interpretation of the probabilities in Eq.(4.18) is straightforward. $p_1 = 1$ holds since we assume that far-reaching fluctuations occur on the background of $F_{i,1}$-fluctuations. Remember that $F_{i,1}$-fluctuations alone do not lead to correlation effects (see Sec. 4.2). $1/\nu$ is the probability of finding a given hole at its original Cu site (cf. Eq.(3.14)). p_{2d} is, therefore, the probability that a target Cu site is singly occupied. p_{2s}, on the other hand, is the probability that a target Cu site is empty, as required for fluctuation process F_{2s}. The probability of finding a given hole at a specific O site on its original plaquette is λ_1^2/ν. Thus, p_4 is the probability that the target O site of fluctuation F_4 is not blocked by the hole of same spin which resides on the neighbouring Cu site, as shown in Fig. 4.4(a). Analogously, p_3 is the probability that the target O site of fluctuation F_3 is not blocked. The additional factor 2 in p_3 (as compared to p_4) is due to site-changing processes. This is illustrated in Fig. 4.5. There are two processes that both contribute a term $-\lambda_1^2/\nu$ to p_3. The first process is shown in Fig. 4.5(a). This process is excluded by the Pauli principle. Therefore, its contribution has to be subtracted. This leads to a correction $-\lambda_1^2/\nu$ which is analogous to the one in p_4. The second process is shown in Fig.4.5(b). The contribution of this site-changing process is the same as for the one in Fig. 4.5(a). The negative sign in process (b), however, is due to the fact that in its final state two fermions have changed places (i.e. Cu sites). Thus, strictly speaking it is not possible to distinguish between hole i and the surrounding holes. Nevertheless, the contribution of process (b) can be formally included into the probabilities p_α which otherwise describe the configuration of surrounding holes. Notice that both the Pauli principle and

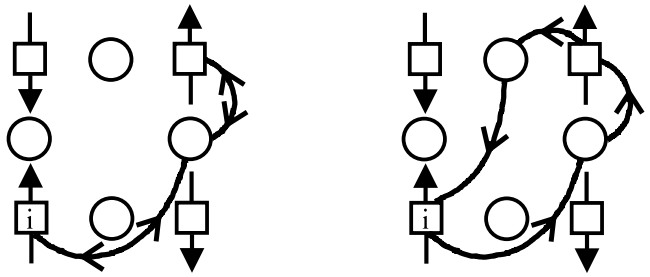

Figure 4.5: Two contributions to p_3. Process (a) is excluded by the Pauli principle. Process (b) is a site-changing process.

exchange processes reduce the probability for fluctuation processes, and that the amount of this reduction is the same in both cases.

Let us now derive Eq.(4.15). We start by factorizing all operators in Eq.(4.14) with respect to α as well as i. This means

$$\begin{aligned} \langle \Psi \mid \Psi \rangle &= \langle \psi_0 | \prod_i \left(1 + \sum_\alpha \lambda_\alpha^2 F_{i,\alpha}^\dagger F_{i,\alpha} \right) | \psi_0 \rangle \\ &= \left(1 + \sum_\alpha \langle \psi_0 | \, F_{i',\alpha}^\dagger F_{i',\alpha} \, | \psi_0 \rangle \; \lambda_\alpha^2 \right)^N \quad , \end{aligned} \tag{4.19}$$

where, due to translational symmetry, Cu site i' is arbitrary. The matrix elements with state $|\psi_0\rangle$ are easy to evaluate. The result is

$$\langle \Psi \mid \Psi \rangle = \left(1 + \sum_\alpha z_\alpha \lambda_\alpha^2 \right)^N \quad . \tag{4.20}$$

This is a generalization of Eq.(3.11) for the single plaquette. Notice that, in contrast to Eq.(4.15), Eq.(4.19) does not yet contain the probabilities p_α. All holes fluctuate independently of the configuration of the other holes. This shows that in Eq.(4.20) all many-body effects have been neglected. We now improve the approximation by treating the many-body effects in a mean-field way. This means we replace $|\psi_0\rangle$ in Eq.(4.20) by the normalized full ground state $|\Psi\rangle$

$$\langle \Psi \mid \Psi \rangle = \left(1 + \sum_\alpha \frac{\langle \Psi | \, F_{i',\alpha}^\dagger F_{i',\alpha} \, | \Psi \rangle}{\langle \Psi \mid \Psi \rangle} \lambda_\alpha^2 \right)^N \quad . \tag{4.21}$$

The denominator on the r.h.s. is necessary, because – in contrast to $|\psi_0\rangle$ – state $|\Psi\rangle$ is not normalized. This is already the final result of Eq.(4.15), if we define

the projectors $P_{i',\alpha}$ by

$$P_{i',\alpha} = \frac{1}{z_\alpha} F^\dagger_{i',\alpha} F_{i',\alpha} \ .$$

Equation (4.21) describes a state in which the movement of a given hole does not directly depend on the configuration of the surrounding holes. However, there is an indirect influence of the surrounding holes in the form of probability factors attached to the fluctuation parameters λ_α. As discussed above, these factors describe the probability that the configuration of the surrounding holes makes a given process possible. Since this probability itself depends on the full ground state $|\Psi\rangle$, the problem has to be solved self-consistently.

The explicit form of the probabilities p_α is obtained in an analogous way as the norm. For instance, for p_{2s} we obtain

$$\begin{aligned} p_{2s} &= \frac{\langle\Psi| P_{i',2s} |\Psi\rangle}{\nu^N} \\ &= \frac{1}{\nu} \sum_\alpha z_\alpha p_\alpha \lambda_\alpha^2 \\ &= 1 - 1/\nu \ . \end{aligned}$$

We now calculate other ground-state properties using state (4.14). The ground-state energy per Cu site has the same form as in the case (3.12) of a single plaquette

$$E_G = \frac{\langle\psi_0| H |\Psi\rangle}{\langle\psi_0 \mid \Psi\rangle} = -4 t_{pd} \lambda_1 \ . \tag{4.22}$$

Notice that in contrast to the single plaquette λ_1 is now strongly renormalized. This is due to far-reaching fluctuations, as we will see in Sec. 4.4. The Cu-occupation number is

$$\langle n_{Cu} \rangle = \frac{\langle\Psi| n_i^d |\Psi\rangle}{\langle\Psi \mid \Psi\rangle} = \frac{1}{\nu} \left(1 + 4\lambda_{2s}^2 p_{2s} + 4\lambda_{2d}^2 p_{2d}\right) \ . \tag{4.23}$$

For vanishing long-range fluctuations ($\alpha > 1$) this result reduces to Eq.(3.14) for the single plaquette. All terms in Eq.(4.23) have a clear interpretation. The first term $(1/\nu)$ is due to processes in which the hole remains on its original Cu site. The second term $(4\lambda_{2s}^2 p_{2s}/\nu)$ describes processes in which this hole leaves its original Cu site which in turn is occupied by one of the nearest-neighbour holes. Finally, the last term $(4\lambda_{2d}^2 p_{2d}/\nu)$ in Eq.(4.23) is associated with processes in which the hole remains on its original Cu site where one of the nearest-neighbour holes creates a double occupancy.

For the O-occupation number one finds

$$\langle n_O \rangle = \frac{\langle \Psi | \, n_i^p \, | \Psi \rangle}{\langle \Psi \mid \Psi \rangle} = \frac{2}{\nu} \left(\lambda_1^2 + 2\lambda_3^2 p_3 + \lambda_4^2 p_4 \right) \ . \tag{4.24}$$

The number of holes is conserved, i.e. $\langle n_{Cu} \rangle + 2 \langle n_O \rangle = 1$. The double occupancies of Cu and O sites are

$$\langle d_{Cu} \rangle = \frac{\langle \Psi | \, n_{i\uparrow}^d n_{i\downarrow}^d \, | \Psi \rangle}{\langle \Psi \mid \Psi \rangle} = \frac{1}{\nu} \left(4\lambda_{2d}^2 p_{2d} \right) \ , \tag{4.25}$$

and

$$\langle d_O \rangle = \frac{\langle \Psi | \, n_{i\uparrow}^p n_{i\downarrow}^p \, | \Psi \rangle}{\langle \Psi \mid \Psi \rangle} = \frac{1}{4} \langle n_O \rangle^2 \ . \tag{4.26}$$

The last relation holds because there is no Hubbard-U on O sites in model (2.6). Therefore, the expectation value factorizes

$$\begin{aligned} \frac{\langle \Psi | \, n_\uparrow^p n_\downarrow^p \, | \Psi \rangle}{\langle \Psi \mid \Psi \rangle} &= \frac{\langle \Psi | \, n_\uparrow^p \, | \Psi \rangle}{\langle \Psi \mid \Psi \rangle} \frac{\langle \Psi | \, n_\uparrow^p \, | \Psi \rangle}{\langle \Psi \mid \Psi \rangle} \\ &= \frac{\langle \Psi | \, n^p \, | \Psi \rangle}{2 \langle \Psi \mid \Psi \rangle} \frac{\langle \Psi | \, n^p \, | \Psi \rangle}{2 \langle \Psi \mid \Psi \rangle} \\ &= \frac{1}{4} \left(\frac{\langle \Psi | \, n^p \, | \Psi \rangle}{\langle \Psi \mid \Psi \rangle} \right)^2 \ . \end{aligned}$$

Notice that Eqs.(4.23) to (4.26) depend on the fluctuation parameters λ_α. Their values will be determined in the next section.

4.4 Determination of fluctuation strengths

To evaluate the fluctuation parameters λ_α we use Eq.(3.4) for an arbitrary site $i = 0$

$$0 = \langle \Psi | \left[H, F_{0,\alpha}^\dagger \right] | \Psi \rangle \ , \ \alpha = 1, 2, \ldots \qquad .$$

For reasons of clearness we will first present the whole system of equations explicitly, and discuss details of the calculation afterwards. For the first five fluctuation

operators one obtains the following nonlinear system of equations

$$\begin{aligned}
0 &= (E_G - \Delta + 2t_{pp})\,\lambda_1 + t_{pd} + t_{pd}\lambda_{2s}p_{2s} \\
&\quad + t_{pd}\lambda_{2d}p_{2d} + 2t_{pp}\lambda_3 p_3 - 2t_{pp}\lambda_1^2\lambda_3/\nu \ , \qquad (4.27)\\
0 &= E_G\lambda_{2s} + 4t_{pd}\lambda_{2d}\lambda_1/\nu + t_{pd}\lambda_1 p_{2s} \\
&\quad + 2t_{pd}\lambda_3 p_3 p_{2s} + t_{pd}\lambda_4 p_4 p_{2s} \ , \qquad (4.28)\\
0 &= (2E_G - U_d)\,\lambda_{2d} + 4t_{pd}\lambda_{2s}\lambda_1 \\
&\quad + t_{pd}\lambda_1 + 2t_{pd}\lambda_3 p_3 + t_{pd}\lambda_4 p_4 \ , \qquad (4.29)\\
0 &= (E_G - \Delta + t_{pp})\,\lambda_3 p_3 + t_{pp}\lambda_1 p_3 + t_{pd}\lambda_{2s}p_{2s}p_3 \\
&\quad + t_{pd}\lambda_{2d}p_{2d}p_3 + t_{pp}\lambda_4 p_3 - (t_{pd} + 2t_{pp}\lambda_1)\,\lambda_1\lambda_3/\nu \ , \qquad (4.30)\\
0 &= (E_G - \Delta)\,\lambda_4 p_4 + t_{pd}\lambda_{2s}p_{2s}p_4 + t_{pd}\lambda_{2d}p_{2d}p_4 \\
&\quad + 2t_{pp}\lambda_3 p_3 - (t_{pd} + 2t_{pp}\lambda_1)\,\lambda_1\lambda_4/\nu \ . \qquad (4.31)
\end{aligned}$$

$E_G = -4t_{pd}\lambda_1$ is the ground-state energy per Cu site from Eq.(4.22). This system of equations, together with Eqs.(4.15) and (4.18) can be solved self-consistently for all λ_α, and for ν. The solution with the lowest value of E_G is then used in Eq.(4.14) for the ground state. Due to the choice of the phase factors for the fluctuation operators (Sec. 4.1), this solution turns out to be one where all λ_α are positive. The best practical way to obtain a solution is to linearize the above equations by replacing some of the variables λ_1 and ν by constants, which are then tuned until self-consistency is obtained.

Let us first discuss some general features of Eqs.(4.27) to (4.31). In every equation there is a term $E_G\lambda_\alpha$ that results form the first part of the commutator $\left[H, F^\dagger_{0,\alpha}\right]$ in Eq.(3.4). All other contributions are due to the second part of the commutator, except the last term $-(t_{pd} + 2t_{pp}\lambda_1)\,\lambda_1\lambda_3/\nu$ in Eq.(4.30) and $-(t_{pd} + 2t_{pp}\lambda_1)\,\lambda_1\lambda_4/\nu$ in (4.31). These two expressions describe processes in which H acts on other holes than the one from site $i = 0$. In addition to these two terms and to the ones with Δ and U_d, there is one more expression with a negative sign. This is the last term in Eq.(4.27) which describes a site-changing processes (see below).

Generally, expressions with a positive sign lead to an enhancement of fluctuations while terms with a negative sign suppress fluctuations. The contribution of the phase factors ϕ^{ij}_{pd} to the sign of a given term is easy to determine according to the following rule. If the motion of the holes in the process is exclusively due to fluctuation operators the sign remains unchanged. If, on the other hand, one of the hoppings is caused by the Hamiltonian the phases contribute a factor -1. This rule is a consequence of the way in which the signs of the fluctuation operators have been defined in Sec. 4.1.

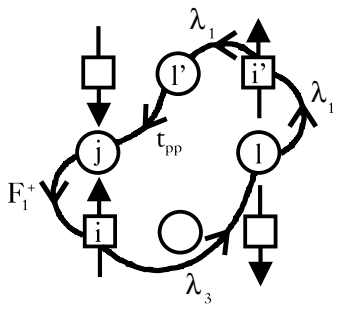

Figure 4.6: A site-changing process that contributes to Eq.(4.27).

As an illustration we now explicitly discuss Eq.(4.27) in some detail. First we note that, for the sake of clarity, all equations have been multiplied by ν and divided by the number of equivalent sites. In the case of $\lambda_\alpha = 0$ for all $\alpha > 1$ Eq.(4.27) reduces to Eq.(3.9) for the single plaquette. The additional terms in Eq.(4.27) describe the coupling between λ_1 and far-reaching fluctuations. Term $(t_{pd}\lambda_{2s}p_{2s})$, for instance, is due to a process in which the hole from site $i = 0$ first fluctuates onto one of its nearest-neighbour Cu sites k using λ_{2s} (see Fig. 4.2). p_{2s} is the probability that this site k has been empty before the fluctuation. Next, with t_{pd} the hole hops back onto the O site j between the two Cu sites. Finally, $F_1^\dagger$ brings the hole back onto its original Cu site. The last term $(-2t_{pp}\lambda_1^2\lambda_3/\nu)$ in Eq.(4.27) is associated with a site-changing process in diagonal direction which is shown in Fig. 4.6. First, using λ_3 the hole from Cu site i fluctuates onto O site l while the hole from Cu site i' fluctuates onto O site l' using λ_1. Then, H moves the hole from O site l' to O site j (contribution t_{pp}). Finally, using $F_1^\dagger$ this hole is transferred from O site j to Cu site i while the hole from O site l moves to Cu site i' using λ_1.

Let us now discuss the results for the parameters λ_α: How does the fluctuation strength depend on the length of the fluctuation process? Table 4.1 shows the values for ν and for the λ_α using parameter set (2.9) for different values for Δ. The comparison with Table 4.2 shows that the parameter λ_1 is larger by at least 10% as compared to the case of a single plaquette (Sec. 3.2).

For all used values of Δ the fluctuation parameters decrease rapidly with increasing distance. Parameter λ_4 is always at least five times smaller than λ_1. Notice, furthermore, that physical properties like occupation numbers, Eqs.(4.23) to (4.26), depend on the *square* of the λ_α. This suggests that contributions from fluctuations beyond the range of $F_{i,4}$ can be neglected.

To check this hypothesis, we now introduce fluctuations that lead beyond the range of operators $F_1, \ldots, F_4$. When the fluctuations F_5 and F_6 are added, Eqs.(4.27) to (4.30) remain unchanged. However, two additional terms contribute

	ν	λ_1	λ_{2s}	λ_{2d}	λ_3	λ_4
$\Delta = 1.5$	2.828	0.568	0.320	0.148	0.179	0.110
$\Delta = 2.5$	2.166	0.464	0.268	0.118	0.128	0.076
$\Delta = 3.5$	1.719	0.377	0.210	0.090	0.087	0.048
$\Delta = 4.5$	1.455	0.309	0.159	0.069	0.059	0.030

Table 4.1: Decrease of fluctuation strength with distance in the CuO_2 plane: ν and λ_α for different Δ.

	λ_1(plaquette)
$\Delta = 1.5$	0.481
$\Delta = 2.5$	0.398
$\Delta = 3.5$	0.331
$\Delta = 4.5$	0.279

Table 4.2: λ_1 as a function of Δ for the single-plaquette system.

to Eq.(4.31) which now reads

$$\begin{aligned} 0 &= (E_G - \Delta)\,\lambda_4 p_4 + t_{pd}\lambda_{2s} p_{2s} p_4 + t_{pd}\lambda_{2d} p_{2d} p_4 + 2t_{pp}\lambda_3 p_3 \\ &\quad + t_{pd}\lambda_5 p_5 + 2t_{pp}\lambda_6 p_6 - (t_{pd} + 2t_{pp}\lambda_1)\,\lambda_1\lambda_4/\nu \ . \end{aligned} \tag{4.32}$$

Furthermore, there are two new equations for the parameters λ_5 and λ_6

$$\begin{aligned} 0 &= E_G\lambda_5 p_5 + t_{pd}\lambda_4 p_5 + 2t_{pd}\lambda_6 p_6 \\ &\quad - (3t_{pd} + 2t_{pp}\lambda_1)\,\lambda_1\lambda_5/\nu \ , \end{aligned} \tag{4.33}$$

$$\begin{aligned} 0 &= (E_G - \Delta)\,\lambda_6 p_6 + t_{pp}\lambda_4 p_6 + t_{pd}\lambda_5 p_6 \\ &\quad - 2\,(t_{pd} + t_{pp}\lambda_1)\,\lambda_1\lambda_6/\nu \ , \end{aligned} \tag{4.34}$$

with the probabilities

$$p_5 = 1 - \left(1 + \lambda_1^2\right)/\nu \quad , \quad p_6 = 1 - \left(1 + 2\lambda_1^2\right)/\nu \ . \tag{4.35}$$

It turns out that the change in the parameter values due to these two new fluctuations is small. In Table 4.3 we show a comparison between the results with 5 and with 7 fluctuation operators using parameter set (2.9).

It is found that ν, as well as the parameters λ_1 to λ_4 show only a small increase when the long-range parameters λ_5 and λ_6 are included. These results retrospectively justify the neglect of far-reaching fluctuations and many-body effects. The same conclusion can be drawn for the CuO_3 chain, see Appendix A. As a consequence of the decrease of fluctuation strength with distance the

	ν	λ_1	λ_{2s}	λ_{2d}	λ_3	λ_4	λ_5	λ_6
5 operators	1.719	0.377	0.210	0.090	0.087	0.048	0	0
7 operators	1.724	0.377	0.211	0.091	0.087	0.051	0.016	0.007

Table 4.3: Influence of far-reaching fluctuations in the CuO_2 plane: ν and λ_α for 5 and 7 fluctuation operators.

holes in the ground state are found to be rather localized. Figure 4.7 shows the delocalization probability $p_\alpha \lambda_\alpha^2/\nu$ of a given hole summed over equivalent final sites as a function of fluctuation length for parameter set (2.9). The probability of finding the hole on its original plaquette is $74.5\% + 16.5\% = 91.0\%$. The delocalization to nearest-neighbour plaquettes has a probability of $8.4\%+0.57\% = 8.97\%$. The contribution of more far-reaching fluctuations amounts to less than 0.1 percent.

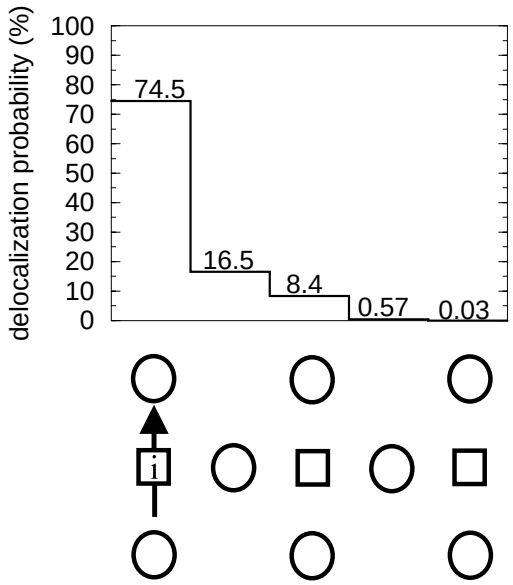

Figure 4.7: Delocalization probability as a function of fluctuation length. The graph shows the delocalization probability of a hole which originates from Cu site i. The probability is summed over the sites displayed beneath the bars, and over all equivalent final sites. The hole is found to remain predominantly on its original plaquette. Delocalization beyond the nearest-neighbour plaquette is negligible small.

	ν	λ_1	λ_{2s}	λ_{2d}	λ_3	λ_4
with diag. Cu sites	1.719	0.377	0.210	0.090	0.087	0.048
without diag. Cu sites	1.873	0.393	0.255	0.108	0.108	0.064

Table 4.4: Influence of diagonal Cu sites in the CuO_2 plane: ν and λ_α with and without taking account of the diagonal Cu sites.

Thus, ground state (4.14) may be visualized as a superposition of mutually correlated but localized "hole clouds" (like the one shown in Fig. 4.7) around the Cu sites.

Finally, we discuss the suppression of fluctuations due to site-changing processes with the diagonal Cu sites. This effect is illustrated in Table 4.4 by comparing the λ_α obtained for parameter set (2.9) with or without taking account of the diagonal Cu sites.

If the diagonal Cu sites are neglected the parameters λ_{2s} to λ_4 are found to increase by at least 20%. Consequently, the probability to find a hole outside of its original plaquette raises from 0.09 to 0.14. This shows that the diagonal sites play an important role in the suppression of fluctuations in the CuO_2 plane.

In Appendices A and B the formalism outlined above is applied to the geometry of a CuO_3 chain. More properties of the ground state will be discussed in Chap. 5.

Chapter 5

Ground-state properties

In this chapter we analyze ground-state properties of Hamiltonian (2.6) for half-filled CuO_3 chains and CuO_2 planes obtained within the formalism outlined in Chap. 4 and Appendix A. In order to compare with other methods we first employ a numerical approach, the Projector Quantum Monte Carlo (PQMC) method. The principles of the PQMC are explained in Appendix C. In Secs. 5.1 and 5.2 we investigate finite-size effects as well as the convergence of the results with respect to other parameters. Furthermore, we compare the PQMC results with exact diagonalization calculations. In Sec. 5.3 we compare our analytical results with those of the numerical simulations. We find good agreement for a wide range of model parameters, from small to very large charge fluctuations. Similarities and differences between Cu-O networks of varying dimensionality are discussed. In Sec. 5.4 we investigate properties of the analytical ground state in several special parameter ranges. Finally, the chapter is concluded with an outlook.

5.1 Numerical results for CuO_3 chains

The Projector Quantum Monte Carlo method (PQMC) is a numerical approach that can be used to calculate ground-state properties of finite clusters. For an introduction to this method see Appendix C. In the PQMC the ground state $|\Psi\rangle$ is projected out from a suitable trial state $|\psi_{\rm trial}\rangle$. Since this projection is not exact, it has to be investigated whether the results are converged with respect to the projection parameter β. Furthermore, since in the PQMC finite clusters are used to draw conclusions about infinite systems, one has to check the numerical results for finite-size effects.

In the present work, a mean-field version of the analytical ground state (3.2) has been used as trial state $|\psi_{\rm trial}\rangle$ in the PQMC for CuO_3 chains as well as for

cluster	# Cu sites	# $O^{\perp}$ sites	# $O^{\parallel}$ sites	total # sites
1×4	4	8	4	16
1×6	6	12	6	24
1×8	8	16	8	32
1×10	10	20	10	40
1×12	12	24	12	48
1×14	14	28	14	56
1×16	16	32	16	64

Table 5.1: Size of CuO_3 chain clusters used in the QMC simulations.

CuO_2 planes. For this purpose we have constructed a state in the form of a Slater determinant using the delocalization probabilities $p_\alpha \lambda_\alpha^2/\nu$ from Appendix A and Sec. 4.4 in Eq.(C.3). It turns out that the results of the PQMC do not depend on the details of the test state. No sign problem occurred.

We have investigated ground-state properties of Hamiltonian (2.6) for 7 different half-filled CuO_3 chain clusters with periodic boundary conditions. The cluster size ranges from a chain of 4 plaquettes to a chain of 16 plaquettes, as shown in Table 5.1. $O^{\perp}$ and $O^{\parallel}$ are the O sites out of chain direction, and in chain direction (see Fig. A.1). In Fig. 5.1 we show the convergence with respect to the projection parameter β for a chain of length 1×4. For parameter set (2.9) with $\Delta = 2.5$ the ground-state energy per Cu site E_G, the Cu occupancy $\langle n_{Cu} \rangle$, the Cu-double occupancy $\langle d_{Cu} \rangle$, and the in-chain O-double occupancy $\left\langle d_O^{\parallel} \right\rangle$ are shown as a function of $1/\beta$. Thereby $m = 64$ for $\beta = 2$, $m = 128$ for $\beta = 4, 8$, and $m = 256$ for $\beta = 12$. The crosses denote the exact values that have been calculated using numerical exact diagonalization (ED) by S.-L. Drechsler [28]. In general, the results of the PQMC are in excellent agreement with the exact results. For $\beta = 8$ and larger most of the exact results lie within the error bars of the PQMC. The number of holes is conserved within the statistical error. We find an analogous agreement between PQMC and ED for a chain of length 1×6, see also Fig. 5.2. Therefore, it is safe to conclude that the results of the PQMC for CuO_3 chains are converged for $\beta \geq 8$.

The CuO_3 chain clusters have interesting finite-size effects. In Fig. 5.2 we show the ground-state energies and several occupancies for chains from length 1×4 up to 1×16 as a function of $1/L^2$, where L is the system length. The model parameters are those of set (2.9) with $\Delta = 2.5$, the parameters of the PQMC are $\beta = 12$ and $m = 256$. The exact results for the 1×4 and 1×6 systems [28] are shown as crosses.

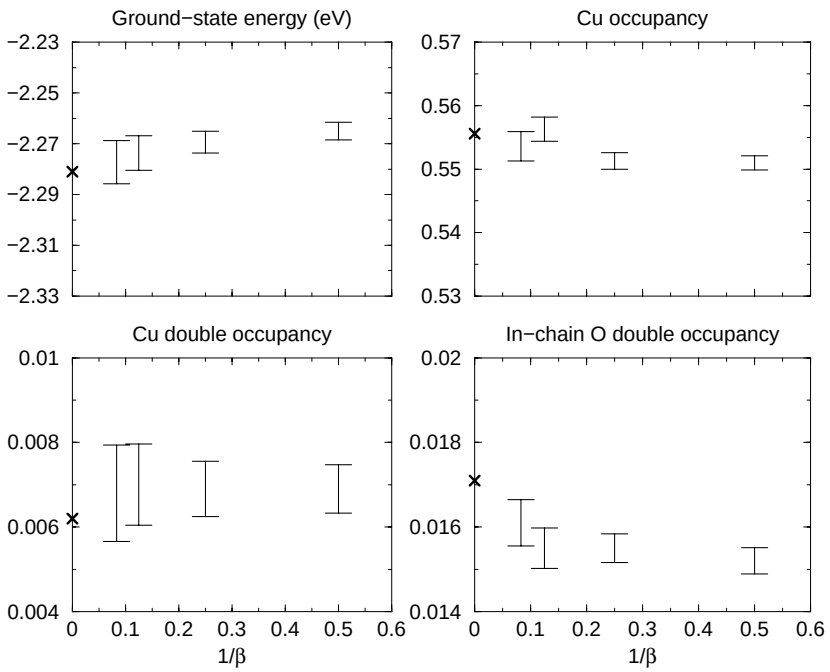

Figure 5.1: 1×4 system: Convergence with respect to β. Crosses denote the exact results from Ref. [28].

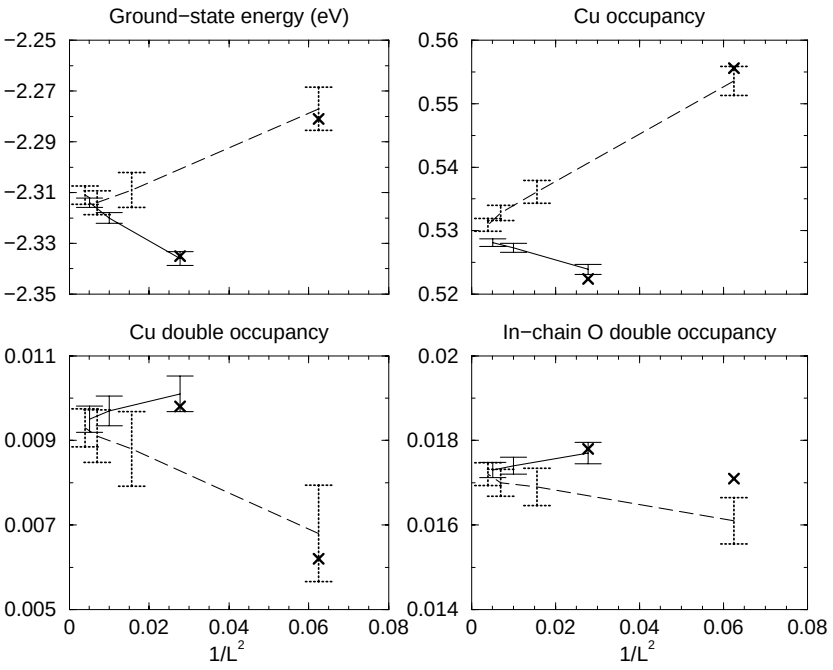

Figure 5.2: Convergence with respect to system length L. Dashed lines connect open shell configurations, solid lines closed shell configurations.

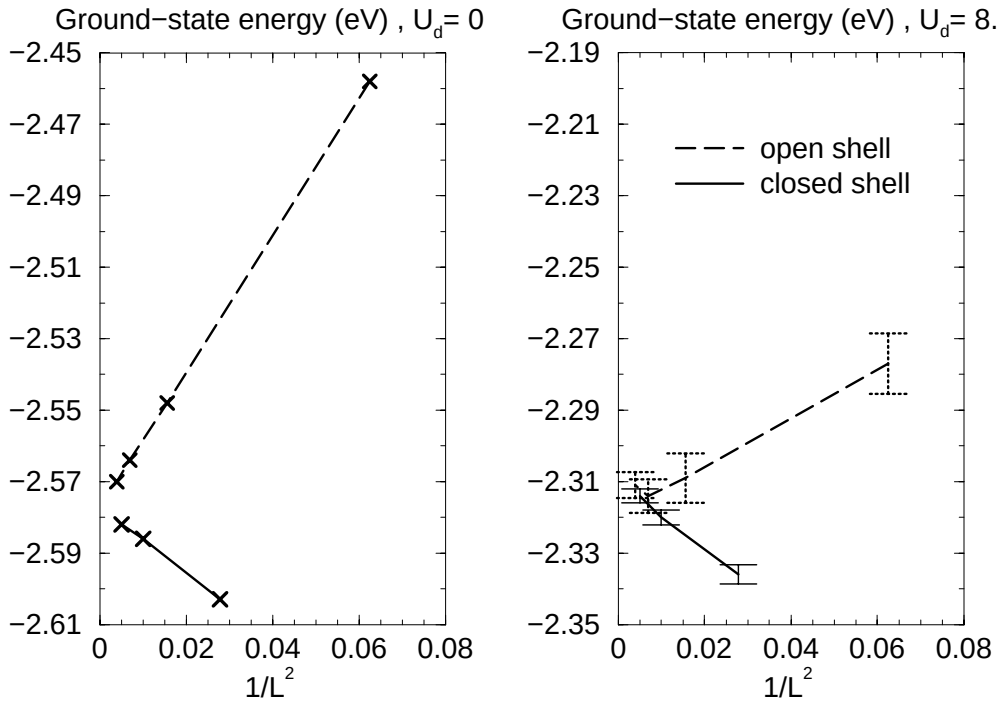

Figure 5.3: Ground-state energy: Convergence with respect to system size for vanishing and non-vanishing U_d.

It is found that the values for chains of length $1 \times (4n)$, $n = 1, \ldots 4$ (connected by broken lines) show a completely different scaling behaviour than the values for chains of length $1 \times (4n + 2)$, $n = 1, \ldots 3$ (connected by solid lines). The $1 \times (4n)$ results approach the limit $L \to \infty$ from a more localized regime with higher ground-state energy and Cu occupancy, and smaller O- and double occupancies.

The $1 \times (4n + 2)$ results, on the other hand, lie in a more delocalized regime with lower ground-state energy etc. This phenomenon can be explained by an analysis of the same systems with $U_d = 0$. In this case one deals with uncorrelated holes, and the many-hole problem is reduced to a single-hole problem (in the sense of a Fermi sea). Therefore, the exact solution for all clusters can be easily obtained numerically. The results for the ground-state energy are compared to those for $U_d = 8.8$ in Fig. 5.3. Again, one observes a different behaviour for $1 \times (4n)$ systems and $1 \times (4n + 2)$ systems. Notice that for $U_d = 0$ and for $U_d = 8.8$ intervals of the same length are displayed on the y-axes. Thus, Fig. 5.3 shows that for $U_d = 0$ the difference is even more pronounced than for $U_d = 8.8$. This difference is caused by different symmetry properties of the distribution of holes in the Brillouin zone at half filling. For the $1 \times (4n)$ systems the states at the Fermi level are only partly occupied ("open shell"). For the $1 \times (4n + 2)$

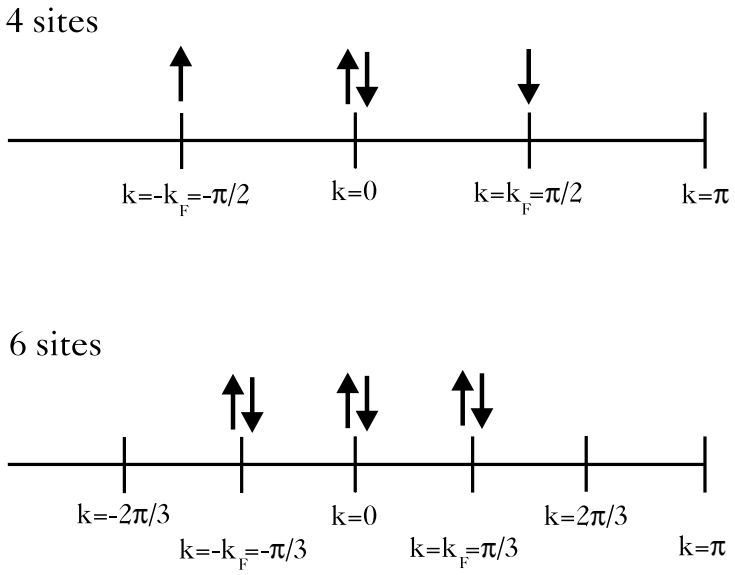

Figure 5.4: Open shell / closed shell effect: Brillouin zones of a 4-site chain and a 6-site chain at half filling.

systems, on the other hand, all states at the Fermi level are occupied ("closed shell").

This has the following mathematical reason. In contrast to the "open shell" case, for the "closed shell" configuration the number $(4n+2)/2$ is odd. Therefore, these states are distributed symmetrically around the state with zero momentum. This fact is illustrated in Fig. 5.4 where we show the Brillouin zones of a 4-site chain (open shell) and a 6-site chain (closed shell) at half filling. For simplicity, the O sites have been neglected. The Fermi momentum for the 4-site chain is $k_F = \pi/2$. At half filling, only two holes are available for the 4 states with momentum $\pm k_F$ on the "surface" of the Brillouin zone. Therefore, the ground state of the system is degenerate. The situation is different for the 6-site chain. In this case, at half filling there are 4 holes which occupy the 4 states with momentum $\pm k_F$ $(= \pm\pi/3)$. Consequently, the ground state is non-degenerate, and has a lower ground-state energy. As the system size increases the states in the "volume" of the Brillouin zone outnumber the states at the "surface", and the effect disappears. Qualitatively, the same phenomenon remains visible for finite U_d, although the resulting correlations tend to localize the holes. This leads to a quantitative reduction of finite-size effects. Furthermore, the degeneracy of the open-shell ground state leads to error bars that are consistently larger than in the closed-shell case (see Fig. 5.2).

Summarizing, there are some lessons to be learned from (apparently trivial)

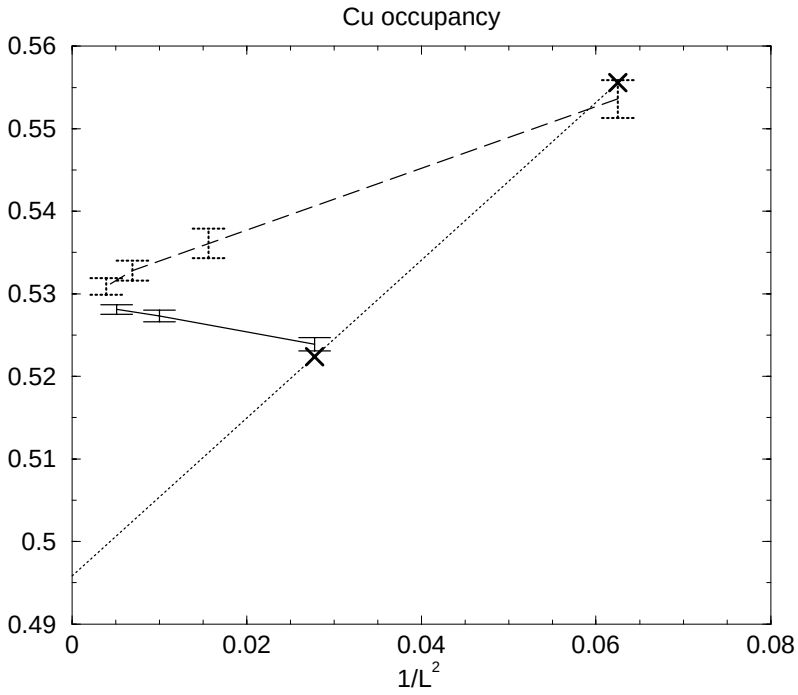

Figure 5.5: Finite-size effects: A naive linear extrapolation (dotted line) of the exact results for small system size (crosses) leads to a value for the Cu occupancy that is far off the correct result. The PQMC results are shown as error bars connected by dashed and solid lines.

systems with $U_d = 0$. These systems allow to investigate geometric properties of finite clusters without the additional complication of correlation effects. Thus, for instance, the results for $U_d = 0$ in Fig. 5.3 show that $1/L^2$ is indeed the correct scaling behaviour for CuO_3 chains. For non-vanishing correlations information of this kind is more difficult to obtain since the results are approximations and/or the size of the clusters is very limited (see also Sec. 5.2). Notice, also, that a naive linear extrapolation of the exact values for the 1×4 and 1×6 systems leads to incorrect results, as exemplified for the Cu occupancy with $U_d = 8.8$ in Fig. 5.5. Already the solutions for $U_d = 0$, on the other hand, show that extrapolated values should lie *between* those of the 1×4 and 1×6 system.

Finally, returning to the question of convergence with system size, from Fig. 5.2 we may conclude that convergence is obtained for the 1×12 chain system.

5.2 Numerical results for CuO_2 planes

Two different clusters with periodic boundary conditions have been used for the simulation of half-filled CuO_2 planes. They are shown in Table 5.2.

cluster	# Cu sites	# O sites	total # sites
4×4	16	32	48
6×6	36	72	108

Table 5.2: Size of CuO_2 plane clusters used in the QMC simulations.

Notice that clusters with an odd number of Cu sites have a non-vanishing total spin (which might distort the results), and have therefore not been investigated. The smallest cluster that we consider is a 4×4 system. With 48 sites this system has the same size as a 1×12 CuO_3 chain. Unfortunately, even the 4×4 system is far too large to allow for numerical exact diagonalization. The next-largest system is a cluster of 6×6 plaquettes. This system is the largest cluster that is still accessible to the PQMC within acceptable computation time. Notice that all clusters of the form $n \times n$ with even n have an "open shell" configuration (see Sec. 5.1).

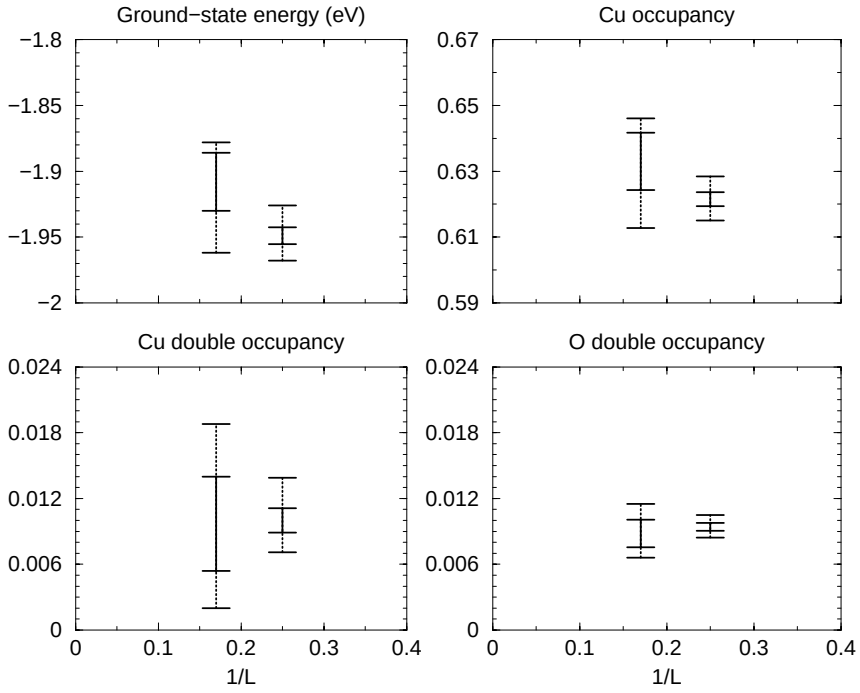

Figure 5.6: Convergence with respect to β and linear system size L. Solid error bars denote the results for $\beta = 4$, dotted error bars the results for $\beta = 8$.

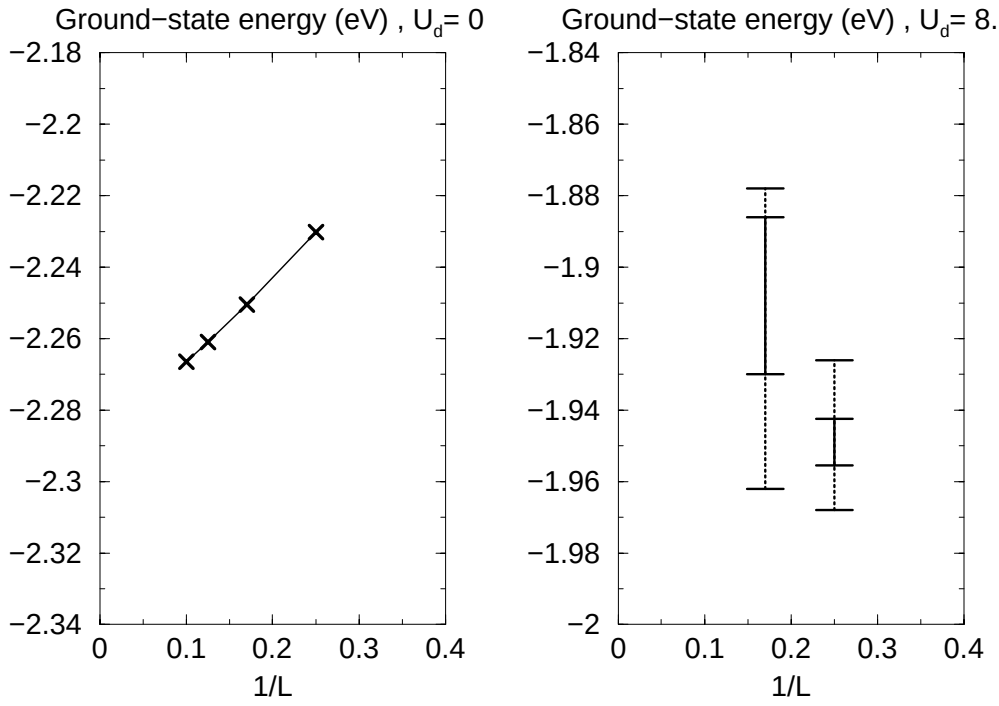

Figure 5.7: Ground-state energy: Convergence with respect to system size for vanishing and non-vanishing U_d. Solid error bars denote the results for $\beta = 4$, dotted error bars the results for $\beta = 8$.

In view of the small number of different clusters and the restrictions imposed on the PQMC by limited computation time it is more difficult to analyze the convergence of the results in the two-dimensional than in the one-dimensional case. Figure 5.6 shows the convergence with respect to β and system size. For parameter set (2.9) the ground-state energy and several occupation numbers are plotted against $1/L$, where L is the linear size of the system (i.e. $L = 4, 6$). Solid error bars denote the results for $\beta = 4$, dotted error bars the results for $\beta = 8$. In both cases $m = 128$. Notice that the intervals displayed on the y-axes of Fig. 5.6 are (upper row) twice, and (lower row) four times as large as in Figs. 5.1 and 5.2.

The results of the 4×4 system seem to be converged with respect to β for $\beta = 4$. On the other hand, the results of the 6×6 system are apparently not yet fully converged with respect to β. Unfortunately, it is not possible to investigate the 6×6 system for larger values of β and m within acceptable computation time using present-day hardware (IBM RS-6000 workstation). Therefore, we may only make a rough estimate of finite size effects. Figure 5.7 shows a comparison of the ground-state energies for $U_d = 0$ and $U_d = 8.8$. In the former case the exact results for clusters of 4×4, 6×6, 8×8, and 10×10 plaquettes are shown. The

fact that the exact ground-state energies lie on a straight line justifies the choice of $1/L$ as scaling parameter (in contrast to $1/L^2$ in the one-dimensional case, see Sec. 5.1). Notice that intervals of the same length are displayed on the y-axes of Figs. 5.7 and 5.3. It seems sensible to assume that, like in the one-dimensional case, the results for $U_d = 0$ give an upper estimate for finite size effects in the case $U_d = 8.8$. Therefore we estimate that the errors due to finite size effects for the 4×4 system are of the same order as the error bars. Consequently, we may conclude that the results of the 4×4 system for $U_d = 8.8$ are already reasonably well converged with respect to system size.

5.3 Numerical vs. analytical results

We now compare the numerically calculated ground-state energies and several occupation numbers with the analytical predictions from Sec. 4.3 and Appendix A. According to the analysis of the PQMC results in Secs. 5.1 and 5.2, the following configurations will be used. For the CuO_3 chain we use a 1×16 cluster (periodic boundary conditions), with parameters $\beta = 12$ and $m = 256$. For the CuO_2 plane, on the other hand, we use a 4×4 cluster (periodic boundary conditions), with parameters $\beta = 4$ and $m = 128$. Using parameter set (2.9) we vary the charge-transfer energy Δ between 1.5 and 4.5 eV, in order to cover the range of very large to fairly small charge fluctuations.

In Fig. 5.8 we show the ground-state energies per Cu site E_G as a function of Δ. For both geometries E_G is found to increase with increasing Δ. This is due to the suppression of fluctuations for larger values of the charge-transfer energy. Interestingly, the values of E_G for the CuO_2 plane are found to lie only about 5 percent below those for the CuO_3 chain, although the holes in the plane may delocalize into twice as many directions as in the chain. This can be interpreted as an effect of the locality of Hamiltonian (2.6) in which on-plaquette fluctuations dominate the ground-state energy, see also Sec. 5.4. Furthermore, in the plane there are diagonal Cu neighbour sites which suppress fluctuations, see Fig. 4.5 and Sec. 4.4. The relatively small reduction of ground-state energy per site with increasing dimension (5% reduction from one to two dimensions) may be compared to the case of the Heisenberg model

$$H_{\text{Heisenberg}} = J \sum_{\langle i,j \rangle} \mathbf{S}_i \mathbf{S}_j \ . \tag{5.1}$$

For one dimension, the exact ground-state energy per site has been calculated for (5.1) by Hulthén [50] seven years after the derivation of the exact ground state

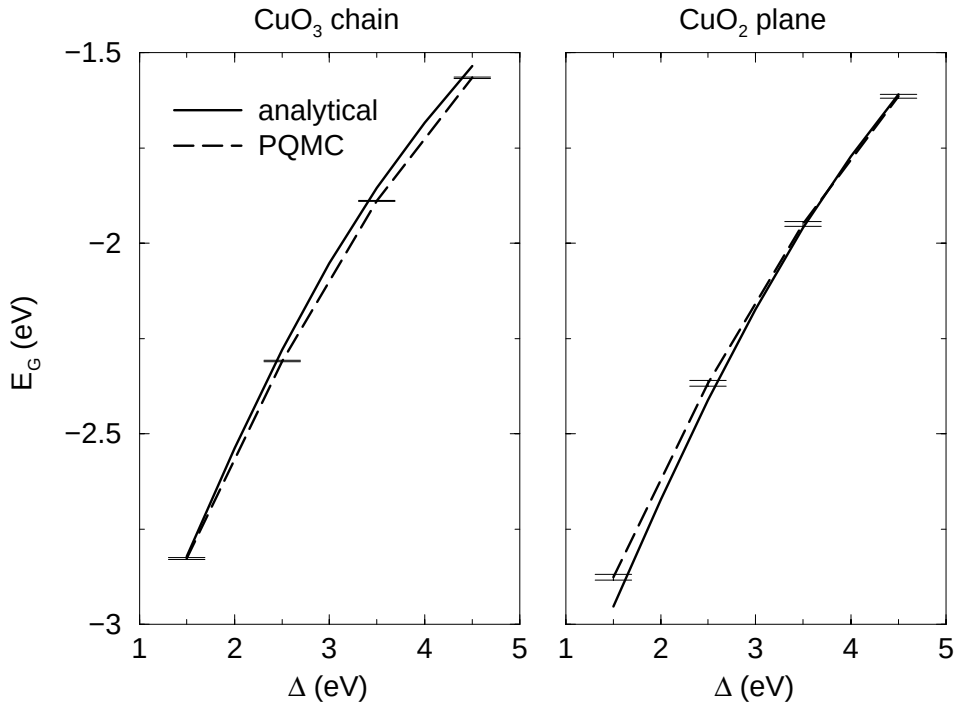

Figure 5.8: Ground-state energies per Cu site as a function of Δ: Analytical results (solid lines) vs. PQMC simulations (error bars, connected by broken lines).

by Bethe [12]

$$E^{1d}_{\text{Heisenberg}} = J\,(-\ln(2) + 1/4) = -0.443\,J\ .$$

For two dimensions, on the other hand, the ground-state energy of the Heisenberg model is not exactly known. The value that is currently favoured by both numerical and analytical methods [111] is

$$E^{2d}_{\text{Heisenberg}} = -0.669\,J\ .$$

Thus, in the Heisenberg model the ground state energy per site for two dimensions lies about 50% below the value for one dimension.

Returning to the multi-band model (2.6) we notice that the agreement between the analytical and numerical results is generally very good, especially in the case of the CuO_2 plane for larger values of Δ. For smaller Δ the analytical ground-state energy is smaller than the PQMC result. This can be explained by the neglect of many-body effects in the analytical approach (see Sec. 4.2) which allows for more unphysical fluctuations when Δ becomes smaller.

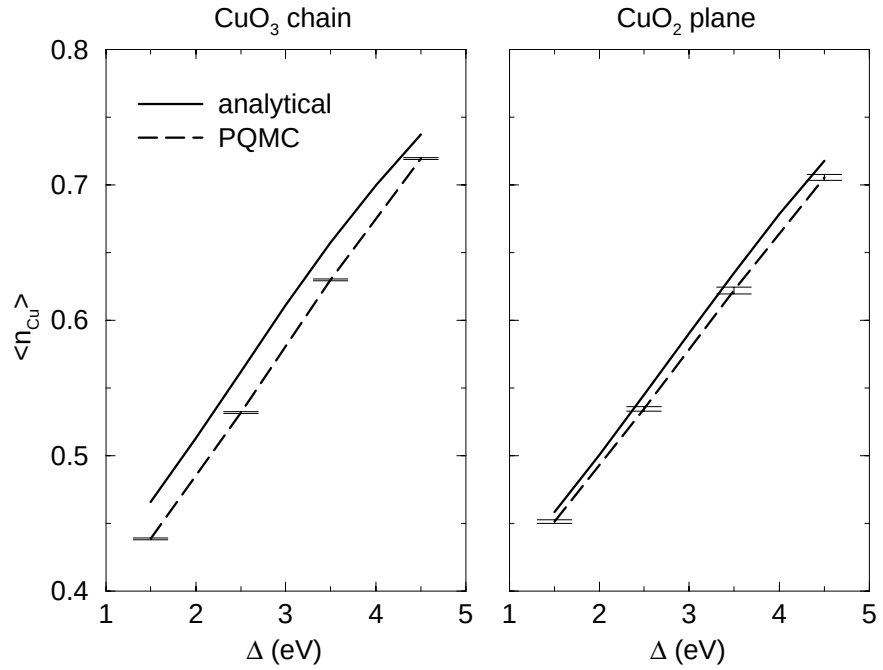

Figure 5.9: Cu occupancy as a function of Δ: Analytical results (solid lines) vs. PQMC simulations (error bars, connected by broken lines).

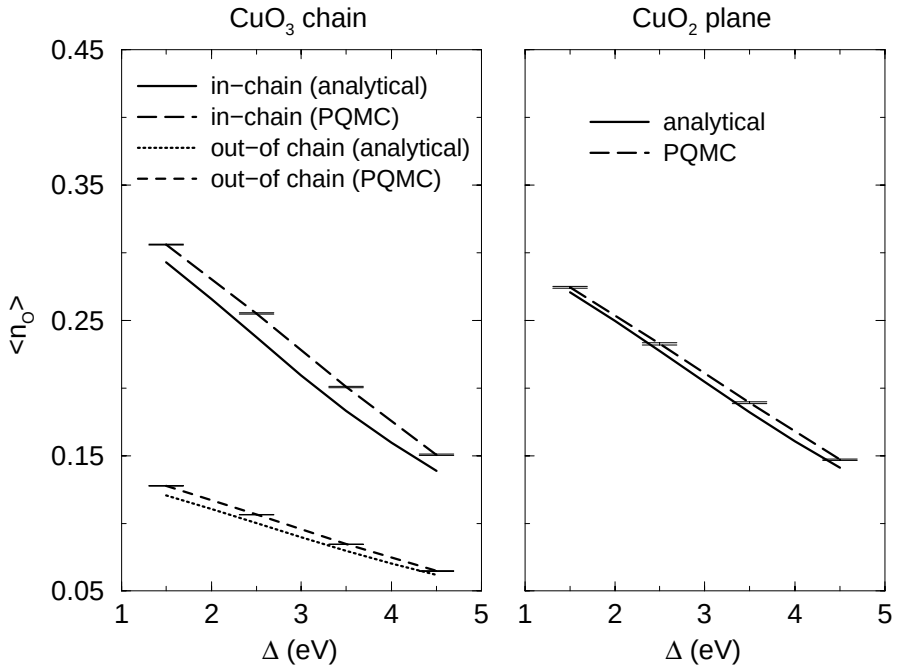

Figure 5.10: O occupancy as a function of Δ: Analytical results (solid lines) vs. PQMC simulations (error bars, connected by broken lines).

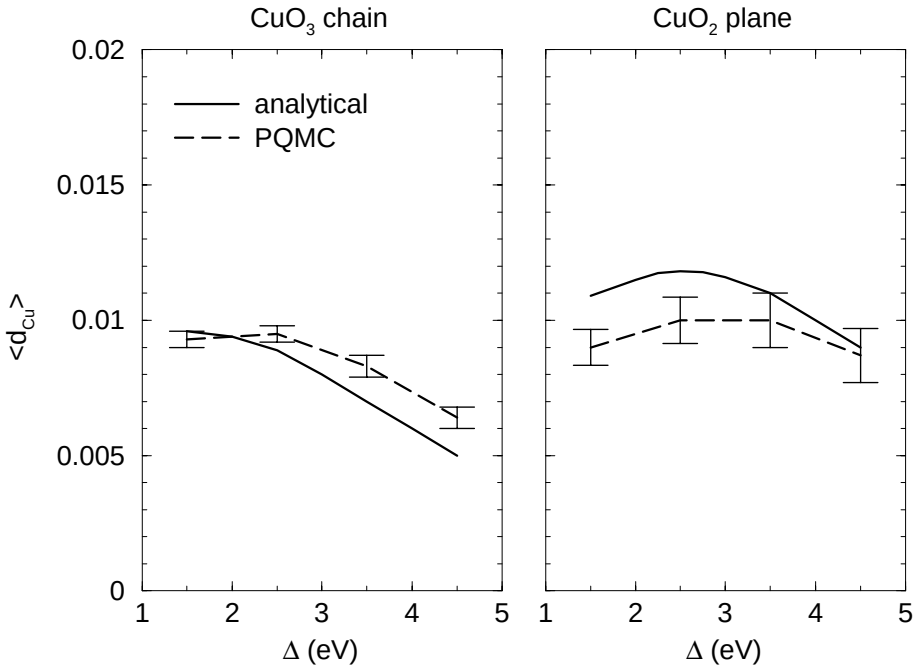

Figure 5.11: Cu double occupancy as a function of Δ: Analytical results (solid lines) vs. PQMC simulations (error bars, connected by broken lines).

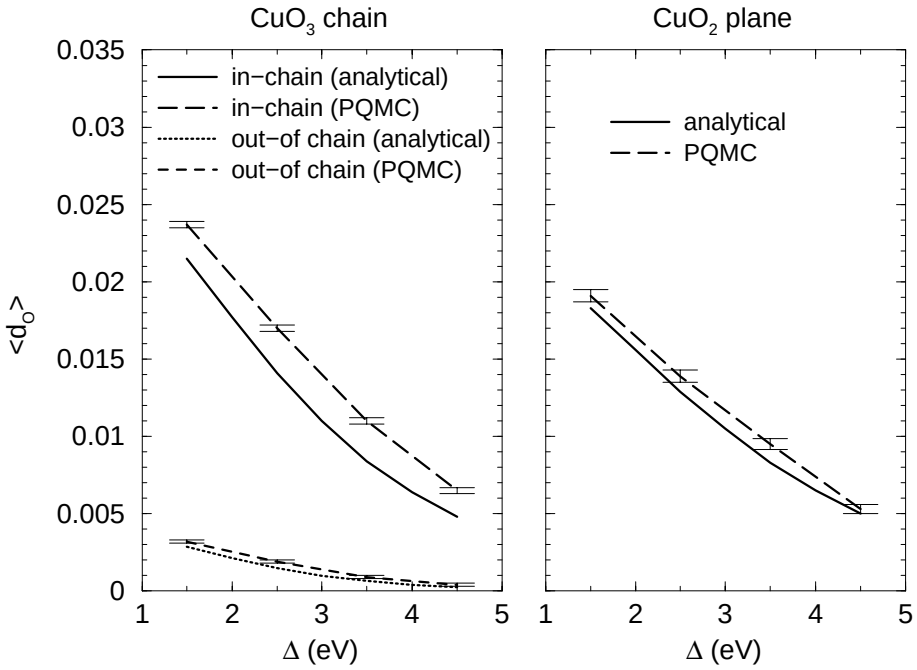

Figure 5.12: O double occupancy as a function of Δ: Analytical results (solid lines) vs. PQMC simulations (error bars, connected by broken lines).

Figure 5.9 shows the Cu occupancy $\langle n_{Cu} \rangle$ as a function of Δ. For both geometries, the suppression of fluctuations for larger charge-transfer energies leads to an increase of $\langle n_{Cu} \rangle$ with increasing Δ. As in the case of the ground-state energies there are only minor differences between the Cu occupancies of the chain and the plane system for the same value of Δ . This can again be attributed to the locality of the model and to the influence of diagonal Cu neighbour sites in the case of the CuO_2 plane. As compared to the numerical results, the analytical predictions slightly overestimate $\langle n_{Cu} \rangle$. Since the number of holes is conserved, the O occupancies (which are shown in Fig. 5.10) are linear functions of $\langle n_{Cu} \rangle$. Therefore, the only new information which Fig. 5.10 contains compared to Fig. 5.9 is the ratio between inner $\left\langle n_O^{\parallel} \right\rangle$ and outer $\langle n_O^{\perp} \rangle$ O-site occupancies in the chain. The agreement between analytical and numerical results is again good.

In Fig. 5.11 we show the Cu double occupancy $\langle d_{Cu} \rangle$ as a function of Δ. The analytical predictions agree well with the numerical results. In contrast to the curves in Figs. 5.8 to 5.10, $\langle d_{Cu} \rangle$ depends non-monotonically on Δ. This is due to the finite value of U_d which suppresses double occupancies on Cu sites. Thus, for small Δ the holes avoid double occupancies on Cu sites, and occupy O sites instead. For large Δ, on the other hand, the holes become localized on their own Cu sites, which again leads to a reduction of Cu double occupancies. There is a region of intermediate values of Δ in which both these effects are simultaneously minimized. In this region $\langle d_{Cu} \rangle$ has a maximum. These results agree with Quantum Monte Carlo simulations of CuO_2 clusters by Scalettar and coworkers [87], and Bhattacharya and coworkers [13].

Figure 5.12 shows the O double occupancies $\left\langle d_O^{\parallel\perp} \right\rangle$, $\langle d_O^{\perp} \rangle$ (chain), and $\langle d_O \rangle$ (plane) as a function of Δ. Like in the case of single occupancies the agreement between analytical and numerical results is somewhat better for two than for one dimension. However, in both cases the differences are rather small. All double occupancies increase monotonously with decreasing Δ. This is a consequence of the fact that model (2.6) contains no Hubbard-U on the O sites. Thus, in contrast to the Cu sites there is no effect that reduces the $\langle d_O \rangle$ for small Δ. The relation $\langle d \rangle = \langle n \rangle^2 / 4$ (see Eqs.(4.26) and (A.25)) is fulfilled by the PQMC data within the statistical error for $\langle d_O \rangle$, and with high accuracy for $\left\langle d_O^{\parallel} \right\rangle$. Only the values for $\left\langle d_O^{\perp} \right\rangle$ show deviations from this rule. For larger values of Δ the decrease of $\langle d_O \rangle$ with increasing Δ is about two times as large as the decrease of $\langle d_{Cu} \rangle$ (see Fig. 5.11). The reason for this weaker dependence of $\langle d_{Cu} \rangle$ on Δ is that an increase in the charge-transfer energy affects $\langle d_{Cu} \rangle$ only indirectly by reducing the effective Cu-Cu hopping, while – in contrast to $\langle d_O \rangle$ – the on-site energy of the final site is not changed.

Summing up, the comparison with PQMC simulations shows that the analytical expressions from Chap. 4 and Appendix A give a reliable description of charge properties in Cu-O networks. We find good agreement for a wide range of model parameters, from small to very large charge fluctuations. One and two-dimensional networks are found to have very similar charge properties. This result can be explained by the influence of the diagonal Cu sites which suppress charge fluctuations in the plane. Generally, the agreement between analytical and numerical results is somewhat better for the CuO_2 plane. In the next section we investigate other properties of the analytical ground state for several limiting cases of parameter values.

5.4 Limiting cases

In this section we discuss properties of Eq.(A.11) to Eq.(A.16) for chains, and Eq.(4.27) to Eq.(4.31) for planes in special parameter ranges.

5.4.1 Limit of vanishing O-O hopping: $t_{pp} = 0$

In Sec. 3.2, when investigating the problem of a single CuO_4 plaquette, we have noticed that λ_1 is a function of a reduced effective charge-transfer energy $\Delta - 2t_{pp}$, see Eq.(3.5). Since all ground-state properties of this system depend exclusively on λ_1, the only influence of the parameter t_{pp} is to renormalize the charge-transfer energy. Therefore, we get the same results for a plaquette with parameter values (Δ, t_{pp}) as for a plaquette with reduced charge-transfer energy and vanishing O-O hopping $(\Delta - 2t_{pp}, 0)$. On the other hand, for infinite systems the O-O hopping makes additional delocalization processes possible. Therefore, it should have an influence that goes beyond a simple renormalization of Δ. Nevertheless, if one is interested in purely local properties, a system with renormalized charge-transfer energy and vanishing O-O hopping $(\Delta - 2t_{pp}, 0)$ still represents a first

	$\lambda_1(\Delta, t_{pp})$	$\lambda_1(\Delta - 2t_{pp}, 0)$	rel. difference
$\Delta = 1.5$	0.568	0.524	0.08
$\Delta = 2.5$	0.464	0.429	0.08
$\Delta = 3.5$	0.377	0.353	0.07
$\Delta = 4.5$	0.309	0.294	0.05

Table 5.3: λ_1: Comparison between a system with non-vanishing O-O hopping (Δ, t_{pp}) and a system with vanishing O-O hopping and renormalized charge-transfer energy $(\Delta - 2t_{pp}, 0)$.

	$\lambda_4(\Delta, t_{pp})$	$\lambda_4(\Delta - 2t_{pp}, 0)$	rel. difference
$\Delta = 1.5$	0.110	0.071	0.55
$\Delta = 2.5$	0.076	0.046	0.65
$\Delta = 3.5$	0.048	0.029	0.66
$\Delta = 4.5$	0.030	0.018	0.67

Table 5.4: λ_4: Comparison between a system with non-vanishing O-O hopping (Δ, t_{pp}) and a system with vanishing O-O hopping and renormalized charge-transfer energy $(\Delta - 2t_{pp}, 0)$.

approximation to a system with non-vanishing hopping (Δ, t_{pp}). In Table 5.3 this is demonstrated by the solution of Eq.(4.27) to Eq.(4.31) for a CuO_2 plane with parameter set (2.9) for different values of Δ. The relative difference in the last column of Table 5.3 is defined by $(\lambda_1(\Delta, t_{pp}) - \lambda_1(\Delta - 2t_{pp}, 0))/\lambda_1(\Delta, t_{pp})$. We find that the λ_1-values of the plane with renormalized charge-transfer energy and vanishing O-O hopping $(\Delta - 2t_{pp}, 0)$ differ by less than 10% from the λ_1-values of the plane with parameters (Δ, t_{pp}). The difference decreases with increasing Δ (i.e. with increasing localization).

However, as shown in Table 5.4, the non-local properties of the plane with (Δ, t_{pp}) are grossly underestimated by the plane with $(\Delta - 2t_{pp}, 0)$. The relative difference between the λ_4 is large, and it increases with increasing Δ.

5.4.2 Local limit: $t_{pd} \ll \Delta$

If the charge-transfer energy Δ is large compared to the hopping strength the system becomes localized. In this local limit the Cu occupancy approaches 1 (see Fig. 5.9), and the O and double occupancies vanish (Figs. 5.10 to 5.12). Many-hole fluctuations are suppressed, and the ground-state energy is dominated by one-hole on-plaquette fluctuations.

	E_G	E_-	$(E_G - E_-)/E_-$
$\Delta = 1$	-1.938	-1.562	0.24
$\Delta = 2$	-1.346	-1.236	0.09
$\Delta = 4$	-0.875	-0.828	0.06
$\Delta = 10$	-0.395	-0.385	0.03
$\Delta = 100$	-0.040	-0.040	0.00

Table 5.5: Local limit: comparison between the ground-state energies of the plane E_G and the single plaquette E_- with increasing Δ.

This is illustrated in Table 5.5 by the solution of Eq.(4.27) to Eq.(4.31) for a CuO_2 plane with the parameter set $t_{pd} = 1$, $t_{pp} = 0$, and $U_d = 4$, for increasing values of Δ. As Δ increases, the ground-state energy of the plane E_G approaches the ground-state energy of a single plaquette E_- from Eq.(3.5). In the local limit, E_- is dominated by the term $-4t_{pd}^2/\Delta$.

5.4.3 Heisenberg limit with small repulsion: $t_{pd}, U_d \ll \Delta$

As we have seen in the previous subsection, for $t_{pd} \ll \Delta$ the ground-state energy is dominated by one-hole fluctuations. We now discuss the contribution of two-hole fluctuations in this local limit. For simplicity we set $t_{pp} = 0$. If Δ is the largest parameter in Hamiltonian (2.6), final states with O occupation are improbable. Thus, Hamiltonian (2.6) should become equivalent to a model that contains only Cu sites coupled by an effective hopping strength

$$t_{\text{eff}} = t_{pd}^2/\Delta \ . \tag{5.2}$$

This is a one-band Hubbard model [47]

$$H_{1-\text{band}} = -t_{\text{eff}} \sum_{\langle i,i'\rangle\sigma} \left(d_{i\sigma}^\dagger d_{i'\sigma} + h.c. \right) + U_d \sum_i n_{i\uparrow}^d n_{i\downarrow}^d \ . \tag{5.3}$$

In this subsection we assume that the Coulomb repulsion U_d is small: $U_d \simeq t_{pd}$. Notice, however, that for large Δ the parameter U_d is nevertheless large compared to the effective hopping: $t_{\text{eff}} \ll U_d$. In this case, $H_{1-\text{band}}$ maps onto the Heisenberg model [44]

$$H_{1-\text{band}} \to J_1 \left(\sum_{\langle i,j\rangle} \mathbf{S}_i \mathbf{S}_j - \frac{b}{4} \right) \ , \tag{5.4}$$

where $\mathbf{S}$ is the spin operator on the Cu sites.

	$E_G - E_-$	J_1	$(J_1 - \lvert E_G - E_- \rvert)/J_1$
$\Delta = 4$	-0.4693×10^{-1}	0.6250×10^{-1}	0.25
$\Delta = 10$	-0.9398×10^{-2}	0.1000×10^{-1}	0.06
$\Delta = 100$	-0.9992×10^{-4}	0.1000×10^{-3}	0.00

Table 5.6: Heisenberg limit in the plane: with increasing Δ the difference $E_G - E_-$ approaches J_1.

	$E_G - E_-$	$J_1/2$	$(J_1 - 2\,\lvert E_G - E_-\rvert)\,/J_1$
$\Delta = 4$	-0.2357×10^{-1}	0.3125×10^{-1}	0.25
$\Delta = 10$	-0.4699×10^{-2}	0.5000×10^{-2}	0.06
$\Delta = 100$	-0.4996×10^{-4}	0.5000×10^{-4}	0.00

Table 5.7: Heisenberg limit in the chain: with increasing Δ the difference $E_G - E_-$ approaches $J_1/2$.

In Eq.(5.4), the exchange parameter is

$$J_1 = \frac{4t_{\rm eff}^2}{U_d} = \frac{4t_{pd}^4}{\Delta^2 U_d} \ , \tag{5.5}$$

and b is the number of bonds, i.e. $b = N$ in one dimension, and $b = 2N$ in two dimensions. The expectation value of this Hamiltonian in the Néel state $|\psi_0\rangle$ is

$$\begin{aligned} \langle\psi_0|\, J_1 \left(\sum_{\langle i,j\rangle} \mathbf{S}_i \mathbf{S}_j - \frac{b}{4} \right) |\psi_0\rangle &= -J_1 \frac{b}{2} \\ &= -N\, J_1 \begin{cases} \frac{1}{2} & \cdots 1 \text{ dimension} \\ 1 & \cdots 2 \text{ dimensions} \end{cases} . \end{aligned} \tag{5.6}$$

Since we have neglected spin-flip effects in our approximations (see Sec. 4.2), in the local limit our ground state is reduced to the Néel state (3.1). Therefore, the two-hole contribution to the ground-state energy (i.e. $E_G - E_-$) approaches the expectation value (5.6) of the Heisenberg Hamiltonian in the Néel state. In Table 5.6 this is shown by solving Eq.(4.27) to Eq.(4.31) for the CuO_2 plane with parameter set $t_{pd} = 1$, $t_{pp} = 0$, and $U_d = 4$, for increasing values of Δ.

The same result is obtained in one dimension by solving Eq.(A.11) to Eq.(A.16) for the CuO_3 chain with the same parameter values, as shown in Table 5.7.

5.4.4 Heisenberg limit with large repulsion: $t_{pd} \ll \Delta, U_d$

If the Coulomb repulsion U_d is not smaller than the charge-transfer energy Δ, one has to take account of terms in order $(1/\Delta^3)$ as well. Again, we set $t_{pp} = 0$. Up to order $(1/\Delta^3)$ in perturbation theory Hamiltonian (2.6) has the form [48]

$$\begin{aligned} H_{\rm eff} &= \frac{-4t_{pd}^2}{\Delta} \sum_i n_i^d + \frac{16 t_{pd}^4}{\Delta^3} \sum_i n_i^d + \frac{2t_{pd}^4}{\Delta^3} \sum_{\langle i,j\rangle} n_i^d n_j^d \\ &\quad + \frac{4t_{pd}^4}{\Delta^2} \left(\frac{1}{U_d} + \frac{1}{\Delta} \right) \sum_{\langle i,j\rangle} \left(\mathbf{S}_i \mathbf{S}_j - \frac{n_i^d n_j^d}{4} \right) \ , \end{aligned} \tag{5.7}$$

	$E_G - E_-$	J_1	$(J_1 - \lvert E_G - E_- \rvert)/J_1$
$U_d = 10$	-0.3997×10^{-4}	0.4000×10^{-4}	0.0008
$U_d = 100$	-0.3998×10^{-5}	0.4000×10^{-5}	0.0005

Table 5.8: Heisenberg limit: with increasing U_d the difference $E_G - E_-$ approaches J_1.

where $\mathbf{S}$ is again the spin operator on the Cu sites. The first two terms on the r.h.s. of Eq.(5.7) are one-hole terms that describe the (repeated) hopping of a hole from its Cu site onto the surrounding four O sites and back. These terms are contributions from the single-plaquette energy E_-, see Eq.(3.5). The third term in Eq.(5.7) is a two-hole term. It describes a process in which a hole hops onto an O site and back, to be followed by a neighbouring hole which hops onto the same O site and back. The last term in Eq.(5.7) has the form of a Heisenberg Hamiltonian with the exchange parameter [30]

$$J_2 = \frac{4t_{pd}^4}{\Delta^2}\left(\frac{1}{U_d} + \frac{1}{\Delta}\right) \ . \tag{5.8}$$

Note that Ref.[113] gives an incorrect value for J_2. If Δ is large compared to U_d, the exchange parameter J_2 reduces to J_1 from Eq.(5.5). As in the previous subsection we now calculate the expectation value of Hamiltonian (5.7) in the Néel state $|\psi_0\rangle$, and subtract N times the energy E_- of the single plaquette, where N is the number of Cu sites. Up to order $(1/\Delta^3)$ this gives

$$\begin{aligned} \langle\psi_0|\, H_{\text{eff}}\, |\psi_0\rangle - N\, E_- &= \frac{2t_{pd}^4}{\Delta^3} b - J_2 \frac{b}{2} \\ &= -\frac{4t_{pd}^4}{\Delta^2 U_d}\,\frac{b}{2} \\ &= -J_1 \frac{b}{2} \ , \end{aligned}$$

where b is again the number of bonds. Thus, interestingly, in the expectation value with the Néel state the terms of order $(1/\Delta^3)$ cancel exactly. This is also seen from the solution of Eq.(4.27) to Eq.(4.31) for CuO_2 planes ($b = 2N$). In Table 5.8 we show the results using the parameters $t_{pd} = 1$, $t_{pp} = 0$, $\Delta = 100$ for increasing U_d.

5.4.5 Mott-Hubbard limit: $U_d \ll t_{pd}$

After having discussed several localized parameter regimes we conclude this section with a look at a delocalized case: the case of vanishing Coulomb repulsion.

	λ_1	λ_{2s}	λ_{2d}	$(\lambda_{2s} - \lambda_{2d})/\lambda_{2d}$
$U_d = 4$	0.22	0.10	0.06	0.67
$U_d = 1$	0.25	0.27	0.21	0.29
$U_d = 0.5$	0.26	0.36	0.32	0.13
$U_d = 0.1$	0.28	0.45	0.44	0.02
$U_d = 0$	0.29	0.47	0.47	0.00

Table 5.9: Mott-Hubbard limit: behaviour of several fluctuation parameters with decreasing U_d.

As U_d becomes small compared to t_{pd}, the ground state of model (2.6) should change from an insulating (localized) to a metallic (delocalized) state. Since all our approximations are based on the assumption of locality (see Chap. 3), we cannot expect correct results in this limit. Nevertheless, the behaviour of our ground state is interesting from a formal point of view. In Table 5.9 we show the results for λ_1, λ_{2s}, and λ_{2d} in the case of a CuO_2 plane with $t_{pd} = 1$, $t_{pp} = 0$, $\Delta = 4$, and decreasing U_d.

As U_d becomes smaller than t_{pd}, the parameters λ_{2s} and λ_{2d} exceed λ_1. Furthermore, λ_{2d} approaches the value of λ_{2s}. For $U_d = 0$ both parameters λ_{2d} and λ_{2s} are exactly equal. Of course, already for $\lambda_{2s} \simeq \lambda_1$ the system is so delocalized that the results of our ground state are expected to differ strongly from the correct values.

5.5 Outlook

In Chaps. 3 and 4 we have developed an approximate analytical ground state for the multi-band Hamiltonian (2.6). The comparison with numerical simulations has shown that this approximation reliably describes charge properties of the ground state for different geometries and in a wide range of model parameters. In principle, there are three ways to proceed from this point. First, one may try to improve the results presented in this thesis. Obviously, a crude approximation has been made with regard to the magnetic properties of the ground state. Since spin-flip processes have been neglected (Sec. 4.2), the approximation describes spin properties only by means of a Néel configuration. Thus, a better treatment of magnetic properties is clearly a worthy goal, especially in one dimension. There is also room for improvement in the description of charge properties. For instance, it would be fascinating to obtain a clearer picture of the limit of small U_d, i.e. the Mott-Hubbard transition (Sec. 5.4).

The second possible way for a further development of the ideas presented here

is the investigation of more complicated Hamiltonians than (2.6). According to Sec. 2.1, one might introduce a Coulomb repulsion U_p on O sites, and/or an intersite-Coulomb repulsion V_{pd} between neighbouring Cu and O sites (see Eq.(2.2)). In both cases, an additional difficulty will be the fact that now already λ_1-fluctuations lead to many-body effects.

Finally, the third way to proceed would be to allow for hole numbers away from half-filling. An analysis of the doping behaviour of Hamiltonian (2.6) might be a step towards a better understanding of high-temperature superconductivity (Sec. 1.1). For instance, experimentally, the antiferromagnetic order is more stable in electron-doped than in hole-doped cuprates [3]. Using dynamical mean-field theory [65], random phase approximation [93], and a slave-boson approach [6] it has been argued that this result can be explained by an asymmetry of Hamiltonian (2.6) with respect to electron or hole doping [1]. An analysis using the formalism presented here might help to clarify this matter.

Part III

Excitations

Chapter 6

CuO_4 plaquette

In this chapter we investigate the Cu $2p_{3/2}$ core-level XPS for a hole on a single CuO_4 plaquette (see Sec. 3.2), using Hamiltonian (2.1). It turns out that this simple system already allows for a principal interpretation of the experimentally observed structures. For reasons of simplicity, in Sec. 6.1 we first discuss the case of vanishing exchange splitting: $I_{dc} = 0$. The generalization to finite exchange splitting is presented in Sec. 6.2. Although the single-plaquette system is a one-particle problem which can be easily solved exactly, it may nevertheless be compared successfully with experimental results for Bi_2CuO_4 and Li_2CuO_2. This is shown in Sec. 6.3. Results of this chapter have been published in Refs. [5], [108], and [109].

6.1 Basic features

Since the problem of a hole on a single CuO_4 plaquette can be readily solved exactly, it is appropriate to use the form (2.15) for the calculation of the spectral intensity $I(\omega)$

$$I(\omega) \sim \sum_{\theta} \left| \langle \theta | \, c^{\dagger} \, | E_{-} \rangle \right|^2 \, \delta \left[\omega - (E_{\theta} - E_{-}) \right] \; . \tag{6.1}$$

$|E_{-}\rangle$ is the ground state of the full Hamiltonian H_{XPS} from Eq.(2.1) before the creation of the core hole on the Cu site. As explained in Sec. 2.2, $|E_{-}\rangle$ is also the ground state of Hamilton operator H from Eq.(2.6). In the case of a CuO_4 plaquette, the ground state $|E_{-}\rangle$ and the ground-state energy E_{-} are (see Sec. 3.2)

$$\begin{aligned} |E_{-}\rangle &= 2t_{pd} \, |d\rangle - E_{-} \, |p\rangle \; , \\ E_{-} &= \frac{1}{2} \left[\Delta - 2t_{pp} - \sqrt{(\Delta - 2t_{pp})^2 + (4t_{pd})^2} \right] . \end{aligned}$$

Eigenstate	Norm	Eigenenergy
$\left\|E_-^c\right\rangle = c^\dagger \left(2t_{pd}\left\|d\right\rangle + \left(U_{dc} - E_-^c\right)\left\|p\right\rangle\right)$	$4t_{pd}^2 + \left(U_{dc} - E_-^c\right)^2$	E_-^c
$\left\|E_+^c\right\rangle = c^\dagger \left(2t_{pd}\left\|d\right\rangle + \left(U_{dc} - E_+^c\right)\left\|p\right\rangle\right)$	$4t_{pd}^2 + \left(U_{dc} - E_+^c\right)^2$	E_+^c
$\left\|O_1^c\right\rangle = c^\dagger \left(\left\|p_1\right\rangle - \left\|p_2\right\rangle + \left\|p_3\right\rangle - \left\|p_4\right\rangle\right)$	4	Δ
$\left\|O_2^c\right\rangle = c^\dagger \left(\left\|p_1\right\rangle + \left\|p_2\right\rangle + \left\|p_3\right\rangle + \left\|p_4\right\rangle\right)$	4	Δ
$\left\|O_3^c\right\rangle = c^\dagger \left(\left\|p_1\right\rangle - \left\|p_2\right\rangle - \left\|p_3\right\rangle + \left\|p_4\right\rangle\right)$	4	$\Delta + 2t_{pp}$

Table 6.1: Eigenstates and eigenenergies of the single-plaquette system with core hole.

The norm of $\left|E_-\right\rangle$ is $4t_{pd}^2 + \left(E_-\right)^2$.

The vectors $\left|\theta\right\rangle$ in Eq.(6.1), on the other hand, are the five excited eigenstates of H_{XPS} after the creation of the core hole. These states will be determined below. In Eq.(6.1), the pseudo-spin index ξ of the core hole has been suppressed because, for the moment, we restrict ourselves to the case of $I_{dc} = 0$. This means that the resulting states are 4-fold degenerate with respect to ξ, and 2-fold degenerate with respect to the spin σ of the valence hole. Non-vanishing exchange splitting will be discussed in the next section.

We already know the ground-state $\left|E_-\right\rangle$. Thus, for the calculation of $I\left(\omega\right)$ we only need to determine the final states $\left|\theta\right\rangle$ of the system after the creation of the core hole. In the presence of a core hole, the valence hole on the Cu site feels the additional Coulomb repulsion U_{dc}. Formally, this effect is equivalent to an enhanced Cu on-site energy. Therefore, the vectors $\left|\theta\right\rangle$ have the same structure as the eigenvectors before the creation of the core hole (Sec. 3.2). The only difference is an additional Cu on-site energy U_{dc}. The eigenstates and eigenenergies are shown in Table 6.1. State $\left|E_-^c\right\rangle$ is the ground state of the system with core hole. The eigenenergies $E_\pm^c$ are obtained from the energies $E_\pm$ of Eq.(3.5) by formally adding U_{dc} to the Cu on-site energy

$$E_\pm^c = \frac{1}{2}\left[\Delta - 2t_{pp} + U_{dc} \pm \sqrt{\left(\Delta - 2t_{pp} - U_{dc}\right)^2 + \left(4t_{pd}\right)^2}\right].$$

The eigenstates $\left|O_1^c\right\rangle$, $\left|O_2^c\right\rangle$, and $\left|O_3^c\right\rangle$ have pure O character. Consequently, they remain unaffected by the creation of the core hole, and they are orthogonal to $c^\dagger\left|E_-\right\rangle$. However, in Eq.(6.1) only states $\left|\theta\right\rangle$ with a non-vanishing matrix element $\left\langle\theta\right| c^\dagger \left|E_-\right\rangle$ contribute to $I\left(\omega\right)$. Thus, only the two states $\left|E_\pm^c\right\rangle$ lead to a non-

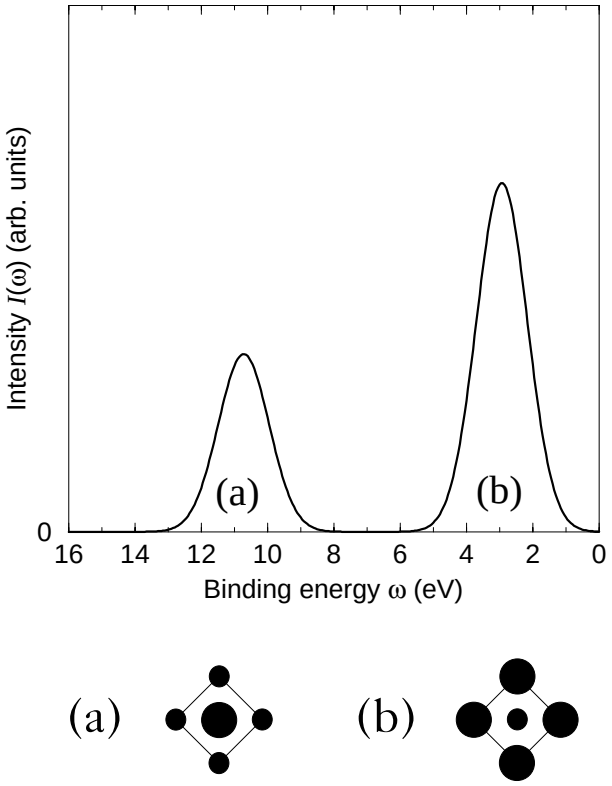

Figure 6.1: Single plaquette spectrum with vanishing exchange interaction. The lower part shows the two final states which correspond to the two peaks in the spectrum. Larger dots symbolize a larger valence hole density.

vanishing spectral intensity

$$\begin{aligned} I(\omega) &\sim \sum_{\pm} \left|\left\langle E_{\pm}^{c}\right| c^{\dagger} \left|E_{-}\right\rangle\right|^{2} \delta\left[\omega - \left(E_{\pm}^{c} - E_{-}\right)\right] \\ &= \sum_{\pm} \frac{\left|4t_{pd}^{2} - \left(U_{dc} - E_{\pm}^{c}\right) E_{-}\right|^{2}}{\left[4t_{pd}^{2} + \left(U_{dc} - E_{\pm}^{c}\right)^{2}\right]\left[4t_{pd}^{2} + \left(E_{-}\right)^{2}\right]} \delta\left[\omega - \left(E_{\pm}^{c} - E_{-}\right)\right] \ . \end{aligned}$$

In Fig. 6.1 we show the resulting spectrum $I(\omega)$ for parameter set (2.9) and $U_{dc} = 8$ eV. The spectral lines have been convoluted with a Gaussian function of width $\Gamma = 1.8$ eV. One observes two peaks that correspond to the two final states $\left|E_{\pm}^{c}\right\rangle$. The peak at lower binding energy (2.92 eV) is due to an excitation into the final state $\left|E_{-}^{c}\right\rangle$. This state has a Cu weight of only 13%, as compared

to 69% in the ground state without core hole $|E_-\rangle$. On the other hand, the final state $\left|E_+^c\right\rangle$, which leads to the peak at higher binding energy (10.71 eV), has a Cu weight of 87%. Thus, the Coulomb repulsion U_{dc} leads to a more pronounced distribution of Cu weight in the two final states. The valence hole distribution in the final states is shown in the lower part of Fig. 6.1, where larger dots symbolize a larger density. The analysis of the Cu weight in the final states allows for a simple interpretation of the energetic positions in the spectrum. In the final state $\left|E_-^c\right\rangle$ the valence hole is predominantly on the O sites. Thus, the Coulomb repulsion U_{dc} is largely avoided at the cost of the charge-transfer energy Δ. On the other hand, in the final state $\left|E_+^c\right\rangle$ the valence hole remains on the Cu site where it is exposed to the Coulomb repulsion U_{dc}. Consequently, the excitation that corresponds to $\left|E_+^c\right\rangle$ is found at higher binding energies. It is separated from the $\left|E_-^c\right\rangle$-excitation by the energy difference

$$E_+^c - E_-^c = \sqrt{(\Delta - 2t_{pp} - U_{dc})^2 + (4t_{pd})^2} \ . \tag{6.2}$$

For small hopping parameters t_{pd} and t_{pp} this difference scales as $U_{dc} - \Delta$. In the following chapters it will become transparent that this characterization remains valid for other CuO structures as well: the excitations at higher (lower) binding energy are due to final states with a high (low) valence-hole density at the core-hole site. It turns out that this is also the basic explanation of the experimentally observed structures at higher binding energy (the satellite), and at lower binding energy (the main line), as discovered by Larsson and Braga [61].

The dependence of the spectrum on the value of the charge-transfer energy Δ is shown in Fig. 6.2. Again, we use parameter set (2.9) and $U_{dc} = 8$ eV. With increasing Δ peak (a) shifts to lower binding energies, and peak (b) to higher binding energies. Consequently, the separation between the two peaks decreases as described by Eq.(6.2). Furthermore, the intensity ratio I_a/I_b increases with increasing Δ. This effect may be interpreted as follows. With increasing Δ the Cu weight in the ground state $|E_-\rangle$ grows. Thus, in Eq.(6.1) the overlap with the final state $\left|E_+^c\right\rangle$ increases, and the intensity of peak (a) becomes larger. This leads to a larger value for I_a/I_b.

For the comparison with experimental spectra it is useful to change parameter values in such a way that the intensity ratio I_a/I_b is influenced, while the separation between (a) and (b) remains constant. This can be achieved if Δ is varied, while the difference $U_{dc} - \Delta$ is kept constant. For $U_{dc} - \Delta = 4.5$ the resulting spectra are shown in Fig. 6.3. Peak (b) is found to behave as in Fig. 6.2. Peak (a), on the other hand, shifts to higher binding energies. Since larger values of U_{dc} lead to a more pronounced distribution of Cu weight in the final states, the ratio

I_a/I_b is influenced even stronger than in Fig. 6.2. The results of Figs. 6.2 and 6.3 agree with the positive correlation between the energy of the main line and the satellite to main-line intensity ratio I_s/I_m found by Tranquada and coworkers [99] both experimentally and theoretically. Later, we will determine the value of Δ by comparing I_a/I_b with the experimental value of the satellite to main line intensity ratio (see Sec. 6.3).

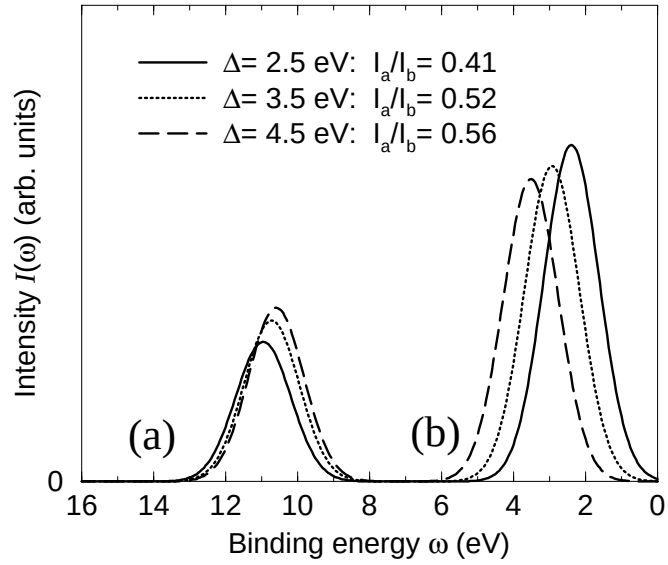

Figure 6.2: Δ-dependence of the single plaquette spectrum.

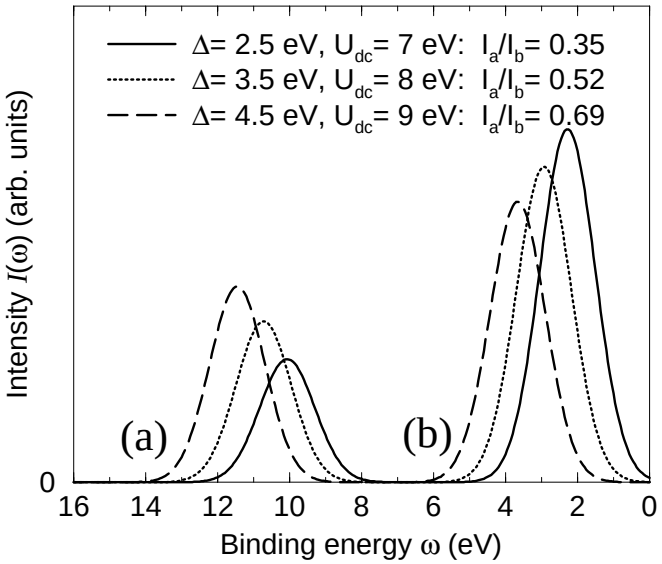

Figure 6.3: Δ- and U_{dc}-dependence of the single plaquette spectrum.

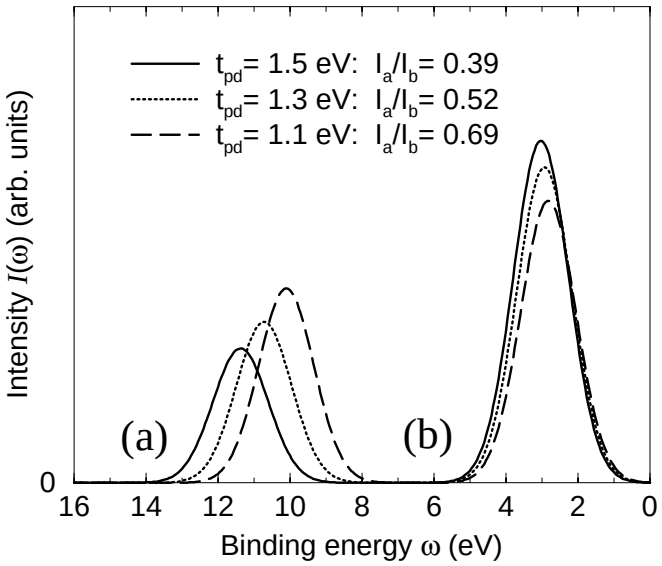

Figure 6.4: t_{pd}-dependence of the single plaquette spectrum.

In Fig. 6.4 we show the influence of the hopping t_{pd} on the spectrum. The parameters are those of set (2.9), with $U_{dc} = 8$ eV. With decreasing t_{pd} the intensity ratio I_a/I_b between peak (a) and (b) increases. Again, the reason for this increase in I_a/I_b is the increase of the Cu weight in the ground state with decreasing t_{pd}. However, in contrast to Figs. 6.2 and 6.3, the value of t_{pd} has almost no influence on the position of feature (b).

6.2 Exchange splitting

We now investigate XPS for non-vanishing exchange coupling: $I_{dc} \neq 0$. In this case, the spectral intensity $I(\omega)$ has the form (2.15)

$$I(\omega) \sim \sum_{\theta} \sum_{\xi,\sigma} \left| \langle \theta(\xi,\sigma)| \, c_{\xi}^{\dagger} \, |E_{-}(\sigma)\rangle \right|^2 \delta\left[\omega - \left(E_{\theta}^{\xi,\sigma} - E_{-}\right)\right] . \qquad (6.3)$$

In Eq.(6.3) the ground state $|E_{-}(\sigma)\rangle$, with energy E_{-}, and the final states $|\theta(\xi,\sigma)\rangle$, with energies $E_{\theta}^{\xi,\sigma}$, depend on the spin index σ and the pseudo-spin index ξ. We have assumed that both spin orientations σ and $-\sigma$ in the ground state have equal probability. Again, the problem is solved if all final states after the creation of the core hole are determined. If all (pseudo-) spin degrees of freedom are taken into account, the single CuO_4 plaquette has 40 eigenstates after the creation of a Cu $2p_{3/2}$ core hole: (5 sites) $\times$ (2 values for σ) $\times$ (4 values for ξ). Obviously, all eigenstates of the problem with $I_{dc} = 0$ that have zero Cu weight

Eigenstate	Norm	Eigenenergy
$\|O_1^c(\xi,\sigma)\rangle = c_\xi^\dagger\left(\|p_1^\sigma\rangle - \|p_2^\sigma\rangle + \|p_3^\sigma\rangle - \|p_4^\sigma\rangle\right)$	4	Δ
$\|O_2^c(\xi,\sigma)\rangle = c_\xi^\dagger\left(\|p_1^\sigma\rangle + \|p_2^\sigma\rangle + \|p_3^\sigma\rangle + \|p_4^\sigma\rangle\right)$	4	Δ
$\|O_3^c(\xi,\sigma)\rangle = c_\xi^\dagger\left(\|p_1^\sigma\rangle - \|p_2^\sigma\rangle - \|p_3^\sigma\rangle + \|p_4^\sigma\rangle\right)$	4	$\Delta + 2t_{pp}$

Table 6.2: Eigenstates and eigenenergies with vanishing Cu weight.

are eigenstates of the problem with $I_{dc} \neq 0$ as well. This gives 24 eigenstates with pure O character: (3 states) $\times$ (2 values for σ) $\times$ (4 values for ξ). They are shown in Table 6.2. However, in analogy to the case $I_{dc} = 0$, these states do not contribute to the spectral intensity of the XPS in Eq.(6.3).

The remaining 16 eigenstates have non-vanishing Cu weight. Therefore, these states have to be eigenstates of the exchange term in Hamilton operator H_{XPS} from Eq.(2.1). They can be found by decomposing the exchange term

$$\mathbf{S}_d \cdot \mathbf{J}_c = S_d^z J_c^z + \frac{1}{2}\left(S_d^+ J_c^- + S_d^- J_c^+\right) \ ,$$

with

$$\begin{aligned} S_d^z &= \frac{1}{2}\left(n_\uparrow^d - n_\downarrow^d\right) \ , \\ S_d^+ &= d_\uparrow^\dagger d_\downarrow \ , \\ S_d^- &= d_\downarrow^\dagger d_\uparrow \ , \end{aligned}$$

and

$$\begin{aligned} J_c^z &= \frac{3}{2}\left(n_{3/2}^c - n_{-3/2}^c\right) + \frac{1}{2}\left(n_{1/2}^c - n_{-1/2}^c\right) \ , \\ J_c^+ &= \sqrt{3}\left(c_{3/2}^\dagger c_{1/2}\right) + 2\left(c_{1/2}^\dagger c_{-1/2}\right) + \sqrt{3}\left(c_{-1/2}^\dagger c_{-3/2}\right) \ , \\ J_c^- &= \sqrt{3}\left(c_{1/2}^\dagger c_{3/2}\right) + 2\left(c_{-1/2}^\dagger c_{1/2}\right) + \sqrt{3}\left(c_{-3/2}^\dagger c_{-1/2}\right) \ . \end{aligned}$$

The factors in these expressions can be calculated using the general formula for ladder operators $J^\pm$ with total angular momentum s and z-component m

$$\left(J^\pm\right)^{s\pm m}|s,\mp s\rangle = \sqrt{\frac{(2s)!\,(s\pm m)!}{(s\mp m)!}}\,|s,m\rangle \ .$$

Generally, the addition of an angular momentum $3/2$ and an angular momentum $1/2$ gives three triplet states (total momentum 1, z-values $\{\pm 1, 0\}$, $\mathbf{S}\cdot\mathbf{J}$ eigenvalue $-5/4$) and five quintet states (total momentum 2, z-values $\{\pm 2, \pm 1, 0\}$, $\mathbf{S}\cdot\mathbf{J}$

eigenvalue 3/4). Thus, the remaining 16 eigenstates of $H_{\rm XPS}$ have to consist of triplet or quintet Cu and O states. The Cu states with triplet symmetry are

$$\begin{aligned}
\left|T_1^d\right\rangle &= \frac{1}{2}c^\dagger_{1/2}\left|d_\uparrow\right\rangle - \frac{\sqrt{3}}{2}c^\dagger_{3/2}\left|d_\downarrow\right\rangle \ , \\
\left|T_0^d\right\rangle &= \frac{1}{\sqrt{2}}c^\dagger_{-1/2}\left|d_\uparrow\right\rangle - \frac{1}{\sqrt{2}}c^\dagger_{1/2}\left|d_\downarrow\right\rangle \ , \\
\left|T_{-1}^d\right\rangle &= \frac{\sqrt{3}}{2}c^\dagger_{-3/2}\left|d_\uparrow\right\rangle - \frac{1}{2}c^\dagger_{-1/2}\left|d_\downarrow\right\rangle \ .
\end{aligned}$$

The quintet Cu states are

$$\begin{aligned}
\left|Q_2^d\right\rangle &= c^\dagger_{3/2}\left|d_\uparrow\right\rangle \ , \\
\left|Q_1^d\right\rangle &= \frac{\sqrt{3}}{2}c^\dagger_{1/2}\left|d_\uparrow\right\rangle + \frac{1}{2}c^\dagger_{3/2}\left|d_\downarrow\right\rangle \ , \\
\left|Q_0^d\right\rangle &= \frac{1}{\sqrt{2}}c^\dagger_{-1/2}\left|d_\uparrow\right\rangle + \frac{1}{\sqrt{2}}c^\dagger_{1/2}\left|d_\downarrow\right\rangle \ , \\
\left|Q_{-1}^d\right\rangle &= \frac{1}{2}c^\dagger_{-3/2}\left|d_\uparrow\right\rangle + \frac{\sqrt{3}}{2}c^\dagger_{-1/2}\left|d_\downarrow\right\rangle \ , \\
\left|Q_{-2}^d\right\rangle &= c^\dagger_{-3/2}\left|d_\downarrow\right\rangle \ .
\end{aligned}$$

The O states with triplet and quintet symmetry, $|T_m^p\rangle$ and $|Q_m^p\rangle$, are obtained from the above expressions by replacing the vector $|d_\sigma\rangle$ with $|p_\sigma\rangle = |p_1^\sigma\rangle + |p_2^\sigma\rangle - |p_3^\sigma\rangle - |p_4^\sigma\rangle$. Thus,

$$\left|T_1^p\right\rangle = \frac{1}{2}c^\dagger_{1/2}\left|p_\uparrow\right\rangle - \frac{\sqrt{3}}{2}c^\dagger_{3/2}\left|p_\downarrow\right\rangle \ ,$$

and so on. All these states are mutually orthogonal, and they are eigenstates of the exchange term $\mathbf{S}_d \cdot \mathbf{J}_c$ in $H_{\rm XPS}$. Therefore, they can be used to construct the remaining 16 eigenstates of $H_{\rm XPS}$ in analogy to the case $I_{dc} = 0$. This gives six triplet states $|T_m^\pm\rangle$ with $m = \{-1, 0, +1\}$, and ten quintet states $|Q_m^\pm\rangle$ with $m = \{-2, -1, 0, 1, +2\}$. They are shown in Table 6.3. The norms of the eigenstates from Table 6.3 are

$$\begin{aligned}
N_\pm^T &= 4t_{pd}^2 + \left(U_{dc} - 5/4I_{dc} - E_\pm^T\right)^2 \ , \\
N_\pm^Q &= 4t_{pd}^2 + \left(U_{dc} + 3/4I_{dc} - E_\pm^Q\right)^2 \ ,
\end{aligned}$$

and the eigenenergies are

$$\begin{aligned}
E_\pm^T &= \frac{1}{2}\left[\Delta - 2t_{pp} + U_{dc} - \frac{5I_{dc}}{4} \pm \sqrt{\left(\Delta - 2t_{pp} - U_{dc} + \frac{5I_{dc}}{4}\right)^2 + (4t_{pd})^2}\right] \ , \\
E_\pm^Q &= \frac{1}{2}\left[\Delta - 2t_{pp} + U_{dc} + \frac{3I_{dc}}{4} \pm \sqrt{\left(\Delta - 2t_{pp} - U_{dc} - \frac{3I_{dc}}{4}\right)^2 + (4t_{pd})^2}\right] \ .
\end{aligned}$$

Eigenstate	Norm	Eigenenergy
$\left\|T_m^-\right\rangle = 2t_{pd}\left\|T_m^d\right\rangle + \left(U_{dc} - 5/4I_{dc} - E_-^T\right)\left\|T_m^p\right\rangle$	N_-^T	E_-^T
$\left\|T_m^+\right\rangle = 2t_{pd}\left\|T_m^d\right\rangle + \left(U_{dc} - 5/4I_{dc} - E_+^T\right)\left\|T_m^p\right\rangle$	N_+^T	E_+^T
$\left\|Q_m^-\right\rangle = 2t_{pd}\left\|Q_m^d\right\rangle + \left(U_{dc} + 3/4I_{dc} - E_-^Q\right)\left\|Q_m^p\right\rangle$	N_-^Q	E_-^Q
$\left\|Q_m^+\right\rangle = 2t_{pd}\left\|Q_m^d\right\rangle + \left(U_{dc} + 3/4I_{dc} - E_+^Q\right)\left\|Q_m^p\right\rangle$	N_+^Q	E_+^Q

Table 6.3: Eigenstates and eigenenergies with non-vanishing Cu weight.

With these final states, the spectral intensity from Eq.(6.3) becomes

$$\begin{aligned} I(\omega) \;\sim\; & \sum_{\pm} \delta\left[\omega - \left(E_{\pm}^T - E_-\right)\right] \sum_{m,\xi,\sigma} \left|\left\langle T_m^{\pm}\right| c_\xi^\dagger \left|E_-(\sigma)\right\rangle\right|^2 \\ & + \sum_{\pm} \delta\left[\omega - \left(E_{\pm}^Q - E_-\right)\right] \sum_{m,\xi,\sigma} \left|\left\langle Q_m^{\pm}\right| c_\xi^\dagger \left|E_-(\sigma)\right\rangle\right|^2 \;. \end{aligned}$$

The matrix elements in this expression can be evaluated

$$\begin{aligned} \left\langle T_m^{\pm}\right| c_\xi^\dagger \left|E_-(\sigma)\right\rangle &= 4t_{pd}^2 \frac{\left\langle T_m^d\right| c_\xi^\dagger \left|d_\sigma\right\rangle}{N_{\pm}^T\left[4t_{pd}^2 + (E_-)^2\right]} \\ &\quad + \left(U_{dc} - 5/4I_{dc} - E_{\pm}^T\right) E_- \frac{\left\langle T_m^p\right| c_\xi^\dagger \left|p_\sigma\right\rangle}{N_{\pm}^T\left[4t_{pd}^2 + (E_-)^2\right]} \\ &= \left[4t_{pd}^2 + \left(U_{dc} - 5/4I_{dc} - E_{\pm}^T\right) E_-\right] \frac{\left\langle T_m^d\right| c_\xi^\dagger \left|d_\sigma\right\rangle}{N_{\pm}^T\left[4t_{pd}^2 + (E_-)^2\right]} \;, \end{aligned}$$

where we have used

$$\left\langle T_m^p\right| c_\xi^\dagger \left|p_\sigma\right\rangle = \left\langle T_m^d\right| c_\xi^\dagger \left|d_\sigma\right\rangle \;.$$

The quintet-matrix element has an analogous form. With

$$\begin{aligned} \sum_{m,\xi,\sigma} \left|\left\langle T_m^d\right| c_\xi^\dagger \left|d_\sigma\right\rangle\right|^2 &= 3 \;, \\ \sum_{m,\xi,\sigma} \left|\left\langle Q_m^d\right| c_\xi^\dagger \left|d_\sigma\right\rangle\right|^2 &= 5 \;, \end{aligned}$$

this finally leads to

$$\begin{aligned} I(\omega) \;\sim\; & \sum_{\pm} \frac{3\left[4t_{pd}^2 + \left(U_{dc} - 5/4I_{dc} - E_{\pm}^T\right) E_-\right]^2}{N_{\pm}^T\left[4t_{pd}^2 + (E_-)^2\right]} \delta\left[\omega - \left(E_{\pm}^T - E_-\right)\right] \\ & + \sum_{\pm} \frac{5\left[4t_{pd}^2 + \left(U_{dc} + 3/4I_{dc} - E_{\pm}^Q\right) E_-\right]^2}{N_{\pm}^Q\left[4t_{pd}^2 + (E_-)^2\right]} \delta\left[\omega - \left(E_{\pm}^Q - E_-\right)\right] \;. \end{aligned}$$

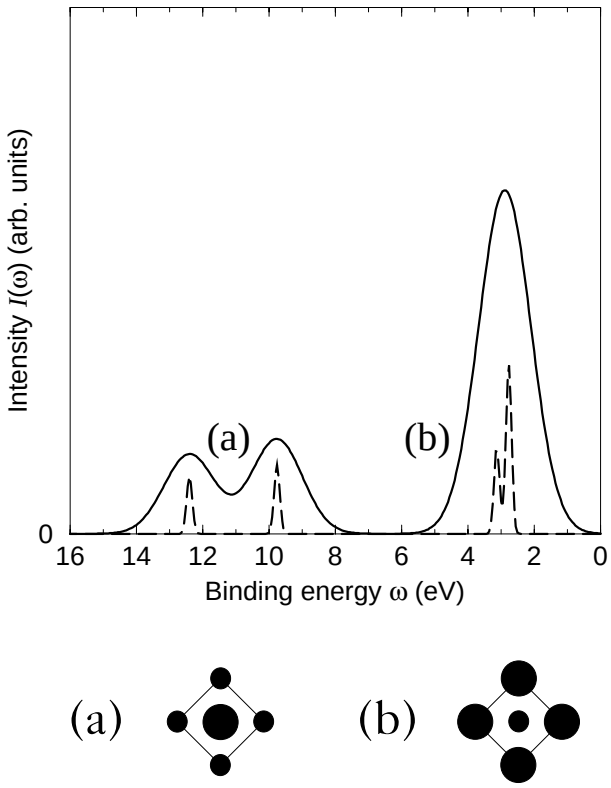

Figure 6.5: Single plaquette spectrum with non-vanishing exchange interaction. The same spectrum is shown with two different line widths: $\Gamma = 1.8$ eV (solid line), and $\Gamma = 0.2$ eV (dashed line). The lower part shows the final states which correspond to the peaks in the spectrum. Larger dots symbolize a larger valence hole density.

The structure of this expression allows for at most four different excitations in the spectrum. In Fig. 6.5 we show $I(\omega)$ for parameter set (2.9) and $U_{dc} = 8$ eV, $I_{dc} = -1.5$ eV. The spectral lines have been convoluted with a Gaussian function of width $\Gamma = 1.8$ eV (solid line), and $\Gamma = 0.2$ eV (dashed line). For larger broadening the spectrum consists of a low-energy peak (b), and a high-energy double peak structure (a).

The valence hole distribution in the final states is shown in the lower part of Fig. 6.5. Comparison with Fig. 6.1 shows that the final states which correspond to structures (a) and (b) have the same characteristics for $I_{dc} \neq 0$ as for $I_{dc} = 0$. For $\Gamma = 1.8$ eV, peak (b) in Fig. 6.5 has practically the same form and position

as peak (b) in Fig. 6.1. Furthermore, the intensity ratio between (a) and (b) is almost the same for $I_{dc} = 0$ and for $I_{dc} \neq 0$. However, the non-vanishing exchange I_{dc} affects the form of peak (a), which formerly had been located at 10.71 eV (see Fig. 6.1). Now, this peak is split *antisymmetrically* (by -0.95 eV and $+1.69$ eV) into two sub-peaks at 9.76 eV and 12.40 eV binding energy. These correspond to the (+)-quintet and (+)-triplet excitations, with an energy separation

$$\begin{aligned} E_+^T - E_+^Q &= -I_{dc} + \frac{1}{2}\sqrt{\left(\Delta - 2t_{pp} - U_{dc} + \frac{5I_{dc}}{4}\right)^2 + (4t_{pd})^2} \\ &\quad -\frac{1}{2}\sqrt{\left(\Delta - 2t_{pp} - U_{dc} - \frac{3I_{dc}}{4}\right)^2 + (4t_{pd})^2} \ . \end{aligned} \tag{6.4}$$

For small hopping parameter t_{pd} this separation is approximately equal to the 'atomic' triplet-quintet separation $(5/4 + 3/4)\,|I_{dc}| = 2\,|I_{dc}|$

$$\left|E_+^T - E_+^Q\right| \simeq 2\,|I_{dc}| \ .$$

There is an analogous splitting of the structure (b) as well. However, for small hopping parameters this splitting vanishes approximately

$$\left|E_-^T - E_-^Q\right| \simeq 0 \ .$$

Therefore, it is only visible for small broadening (dashed line in Fig. 6.5). This fact has an obvious physical interpretation. Since structure (b) is associated with a final state with small Cu weight, there is only a small exchange splitting due to the interaction with the core hole. On the other hand, the large Cu weight in the final states of structure (a) leads to a sizable exchange splitting in the spectrum. We finally note that, compared to the Cu $2p_{3/2}$ spectrum, the exchange splitting for small t_{pd} in the Cu $2p_{1/2}$ spectrum turns out to be half as large: $(3/4 + 1/4)\,|I_{dc}|$. This agrees with the experimental observation that the splitting in the Cu $2p_{1/2}$ spectra is smaller than in the Cu $2p_{3/2}$ spectra (see, for example, Refs. [90] and [71]).

Summing up, the Cu $2p_{3/2}$ core-level spectrum of a single CuO_4 plaquette generally consists of two features: (a) a higher energy structure which is due to a final state with high Cu weight, and (b) a lower energy feature with a final state with small Cu weight. For exchange coupling $I_{dc} \neq 0$ the form of feature (b), and the intensity ratio between (a) and (b) are almost the same as for $I_{dc} = 0$. Non-vanishing exchange coupling does, however, lead to an asymmetric splitting of structure (a) with a separation of approximately $2\,|I_{dc}|$. The two sub-peaks correspond to a quintet and a triplet excitation. The fact that structure (a)

splits asymmetrically is important for the comparison with the experiment: If the exchange splitting is neglected (as in Fig. 6.1), the positioning of the single peak (a) with respect to the broad experimental satellite structure is problematic. For $I_{dc} \neq 0$ this problem is avoided, as will be shown in the next section.

6.3 Comparison with experiments

Although the model of a single CuO_4 plaquette is very simple, it can nevertheless be compared successfully with experimental results of Bi_2CuO_4 and Li_2CuO_2. At this point it is useful to count the degrees of freedom in the experimental spectra and in the theoretical model. The Cu $2p_{3/2}$ XPS spectra of Bi_2CuO_4 and Li_2CuO_2 consist of a symmetric main line and a broader, essentially double-peaked, satellite structure (see Fig. 1.9). Thus, each spectrum has at least six degrees of freedom: the energy position of the main line, the energy difference between main line and satellite, the splitting of the two satellite features, the intensity ratio between main line and satellite, the intensity ratio between the two satellite sub-features, and the width of all spectral peaks. On the other hand, the theoretical CuO_4 plaquette model (see Sec. 2.1) has at first glance seven free parameters: the five parameters Δ, t_{pd}, t_{pp}, U_{dc}, and I_{dc} from Hamiltonian H_{XPS}, the global energy shift ε_c of the spectrum, and the artificial line width Γ that describes finite resolution and lifetime effects. However, as described in Sec. 3.2, Δ and t_{pp} contribute only in the form of an effective charge-transfer energy: $\Delta - 2t_{pp}$. Therefore, they have to be considered as a single free parameter. In addition, it has to be stressed that two or more of the free parameters may have the same influence on the theoretical spectra. Thus, different free parameters are not necessarily independent degrees of freedom for the description of the experiment. A successful description of six experimental degrees of freedom using a model with six free parameters is, therefore, in general a non-trivial achievement. Nevertheless, it is desirable to remove as much arbitrariness from the model as possible. Our strategy in doing this will be twofold. First, if available, we will try to use standard values for the parameters, for instance those of set (2.9). Second, we will try to describe as many different experimental results as possible with the same parameter values. Thus, from the spectrum of Bi_2CuO_4 we determine the value of the global energy shift ε_c, the artificial line width Γ, and the exchange parameter I_{dc}. These parameters should be rather independent of the actual material. Therefore, the same values will then be used for the spectra of Li_2CuO_2 (present section), Sr_2CuO_3 (Sec. 8.1), and $Sr_2CuO_2Cl_2$(Sec. 8.2).

Figure 6.6 shows a comparison of the theoretical spectrum with the experi-

mental result for Bi_2CuO_4 from Ref. [16]. The parameter values for the charge-transfer energy and the hopping amplitudes are those of set (2.9): $\Delta = 3.5$ eV, $t_{pd} = 1.3$ eV, and $t_{pp} = 0.65$ eV. Since there is only one hole, the parameter U_d does not contribute. The values for the core-hole parameters have been adjusted to the experiment: $U_{dc} = 8.5$ eV and $I_{dc} = -1.5$ eV. The energy shift ε_c has been set equal to 931.1 eV, and the line width is $\Gamma = 1.8$ eV. The last three parameter values will be used in the remainder of this thesis (all values are in eV)

I_{dc}	ε_c	Γ
-1.5	931.1	1.8

(6.5)

As can be seen from Fig. 6.6, the agreement between theory and experiment is excellent. The calculated ratio I_s/I_m of the satellite to the main line intensity is 0.56, which compares well to the experimental upper estimate of 0.58 (see Table 1.4). Only in two regions there is a slight mismatch. Region one is between 942 eV and 943 eV binding energy, where the detailed form of the satellite structure is not reproduced correctly. This is due to the rather simple structure of the exchange term in $H_{\rm XPS}$ from Eq.(2.1). A better description of the satellite can be obtained if all spin-orbit and exchange contributions are taken into account, as demonstrated by Goldoni and coworkers [39]. Region two is between 936 eV and 940 eV binding energy, where the theoretical intensity is too small. However, this is explained by the emission from the Bi $4s$ core level which contributes around 940 eV [16]. Since we use a model that consists only of Cu and O sites, this emission is not included in the theoretical spectrum. At this point it should be noted that Karlsson, Gunnarsson, and Jepsen [54] have interpreted the somewhat broader main structure of Bi_2CuO_4 (as compared with Li_2CuO_2) as an effect of the influence of the Bi ions.

The interpretation of the spectral features in Fig. 6.6 has already been given in Sec. 6.2 (see Fig. 6.5). The main line corresponds to a final state with small Cu weight and small exchange splitting. The satellite structure, on the other hand, is due to a final state with large Cu weight and large exchange splitting. These results support the assumption that the CuO_4 plaquettes in Bi_2CuO_4 are rather isolated with respect to their electronic properties.

An analogous conclusion can be drawn for the electronic structure of Li_2CuO_2, as shown in Fig. 6.7. Using the same parameter values as for Bi_2CuO_4 – that is, sets (2.9) and (6.5), as well as $U_{dc} = 8.5$ eV – we obtain again a very good agreement between theory and experiment. The theoretical intensity ratio $I_s/I_m = 0.56$ is identical to the experimental one (see Table 1.4). Only the detailed form of the satellite structure, and the line width of the main peak differ somewhat from the theoretical result. Thus, the hypothesis that the CuO_4

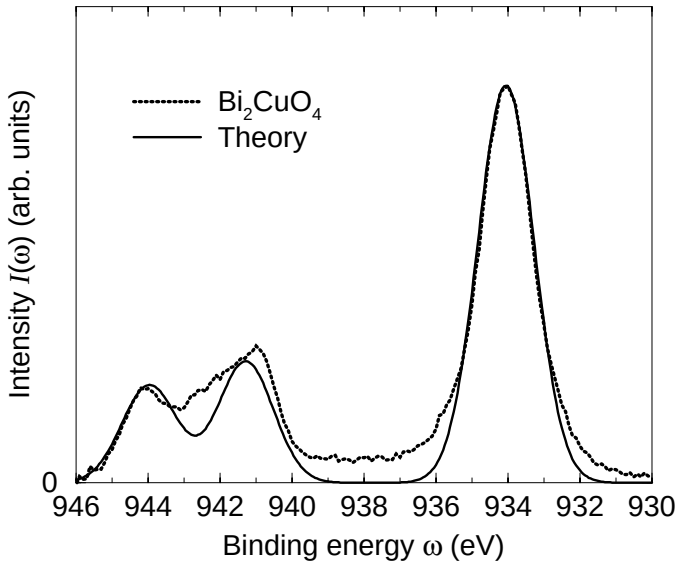

Figure 6.6: Comparison of the theoretical spectrum (solid line) with the experimental result for Bi_2CuO_4 (dots) from Ref. [16].

subunits in Li_2CuO_2 (see Fig. 1.6(b)) are electronically separated seems to be justified. This is supported by exact diagonalization calculations on chain clusters of five edge-sharing plaquettes, where only small finite-size effects have been found [75],[76].

So far we have tried to restrict the number of free parameters in our model by choosing standard values. However, the values of set (2.9) have been determined from LDA band-structure calculations for La_2CuO_4. Although the atomic distances in this compound are more or less similar to those of Li_2CuO_2 (see Sec. 1.2), the values of the parameters may differ from material to material. As mentioned above, another approach is to describe as much experimental information as possible using one single (not necessarily standard-) parameter set. Of course, these parameter values still have to remain within certain acceptable bounds. We have applied this strategy to the electron-energy loss spectrum (EELS) of Li_2CuO_2 [5]. (For an introduction to this experimental method see [34].) It turns out that both the Cu $2p_{3/2}$ XPS and the EELS of Li_2CuO_2 can be described by the CuO_4 plaquette model with one single parameter set: $\Delta = 2.97$ eV, $t_{pd} = 1.28$ eV, $t_{pp} = 0.47$ eV, together with set (6.5) and $U_{dc} = 8.31$ for the core hole. Notice that this set differs only slightly from the one used in Fig. 6.7. There is only a small difference between the effective charge-transfer energy used in Fig. 6.7 ($\Delta - 2t_{pp} = 2.2$ eV), and the above parameter set: ($\Delta - 2t_{pp} = 2.03$ eV). Thus, the additional information of the EELS has essentially removed the

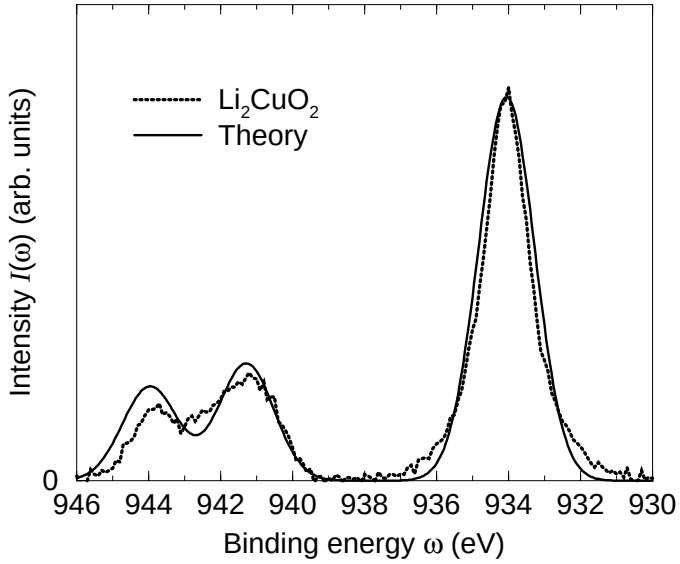

Figure 6.7: Comparison of the theoretical spectrum (solid line) with the experimental result for Li_2CuO_2 (dots) from Ref. [16].

arbitrariness of the individual values for Δ and t_{pp}. Although the calculated ratio $I_s/I_m = 0.52$ for the XPS is somewhat smaller than the experimental one, this result is a strong argument for the locality of the electronic properties of Li_2CuO_2 [5].

Chapter 7

Projection technique

In this chapter we present an analytical method, the Mori-Zwanzig projection technique, which allows to approximately calculate correlation functions in infinite systems. Section 7.1 sketches the basic principles of this method. In Sec. 7.2 we specify the dynamic variables that will be needed for the application of the projection technique to the calculation of Cu core level spectra. The corresponding matrix elements are evaluated in Secs. 7.3 and 7.4. We conclude with a short discussion of the convergence of the method for the case of the CuO_3 chain in Sec. 7.5.

7.1 General

In Quantum Mechanics, dynamic physical quantities can be written in the form of a correlation function

$$G_{AB}(z) = \left\langle A \frac{1}{z - \mathcal{L}} B \right\rangle \ . \tag{7.1}$$

A and B are operators, and $z = \omega + i\eta$. The brackets symbolize the expectation value. $\mathcal{L}$ is the Liouville operator. For arbitrary operators A, $\mathcal{L}$ is defined by

$$\mathcal{L}A = [H, A] \ , \tag{7.2}$$

where H is the Hamilton operator of the system. One example for a correlation function of the form (7.1) is the single core hole correlation function G^{ξ}_{00} from Eq.(2.19)

$$G^{\xi}_{00}(z) = \langle \Psi | \, c_{0\xi} \frac{1}{z - \mathcal{L}_{\mathrm{XPS}}} c^{\dagger}_{0\xi} \, | \Psi \rangle \ ,$$

which determines the intensity of the Cu $2p_{3/2}$ XPS via Eq.(2.18).

The Mori-Zwanzig projection technique [68][114] allows to evaluate (approximately) correlation functions of the form (7.1). The basic concept of this method is to separate the Hilbert space $\mathcal{H}$ of the system into the orthogonal direct sum of a "relevant" part $\mathcal{P}$ and the "rest" $\mathcal{Q}$

$$\mathcal{H} = \mathcal{P} \oplus \mathcal{Q} \; .$$

Subsequently, the part of the problem which belongs to the subspace $\mathcal{P}$ will be solved exactly, while the contribution of $\mathcal{Q}$ will be treated in some form of approximation. This approach encompasses, for instance, several variants of perturbation theory, if $\mathcal{P}$ is identified with the eigenspace of the unperturbed part of the Hamiltonian [37]. The concept of the projection technique is, however, more general, as it may be applied even if there is no obvious "small parameter" in the Hamiltonian. There are orthogonal projection operators P and Q projecting on the subspaces $\mathcal{P}$ and $\mathcal{Q}$, with

$$Q = 1 - P. \tag{7.3}$$

One now generates a set of vectors that span the relevant subspace $\mathcal{P}$. This is achieved by applying operators D_i, the so-called dynamic variables, onto a state $|\Psi\rangle$. Later, we will choose state $|\Psi\rangle$ to be the ground state (3.2) of the multi-band Hamiltonian (2.6). The explicit form of the dynamic variables D_i will be given in Sec. 7.2. For the moment, however, the discussion remains completely general. We only assume that the operators A and B from the correlation function (7.1), which we want to evaluate, are contained in the set of dynamic variables. The vectors $D_\alpha |\Psi\rangle$ are required to be mutually linear independent, but not necessarily orthogonal

$$\sum_\gamma \langle\Psi| D_\alpha^\dagger D_\gamma |\Psi\rangle^{-1} \langle\Psi| D_\gamma^\dagger D_\beta |\Psi\rangle = \delta_{\alpha\beta} \; . \tag{7.4}$$

The projector P can be written in the form

$$P = \sum_{\alpha,\beta} D_\alpha |\Psi\rangle \; \langle\Psi| D_\alpha^\dagger D_\beta |\Psi\rangle^{-1} \langle\Psi| D_\beta^\dagger \; . \tag{7.5}$$

Using Eq.(7.4) it is easy to show that P is indeed idempotent. We define the action of the Liouville operator $\mathcal{L}$ on P as

$$\mathcal{L}P = \sum_{\alpha,\beta} (\mathcal{L}D_\alpha) |\Psi\rangle \; \langle\Psi| D_\alpha^\dagger D_\beta |\Psi\rangle^{-1} \langle\Psi| D_\beta^\dagger \; . \tag{7.6}$$

With these expressions, correlation functions of the form (7.1) can be rewritten

$$\left\langle D_\alpha^\dagger \frac{1}{z-\mathcal{L}} D_\beta \right\rangle = \frac{1}{z}\left\langle D_\alpha^\dagger D_\beta \right\rangle + \sum_{\gamma,\eta} \left\langle D_\alpha^\dagger \frac{1}{z-\mathcal{L}Q}\mathcal{L}D_\gamma \right\rangle \times \left\langle D_\gamma^\dagger D_\eta \right\rangle^{-1} \left\langle D_\eta^\dagger \frac{1}{z-\mathcal{L}} D_\beta \right\rangle \ , \tag{7.7}$$

where $\langle \dots \rangle$ is a shorthand for $\langle \Psi | \dots | \Psi \rangle$ which will be used in the following derivation. Equation (7.7) can be verified by use of the following operator identity

$$\begin{aligned} \frac{1}{z-\mathcal{L}} &= \frac{1}{z-\mathcal{L}Q}\left(z-\mathcal{L}Q\right)\frac{1}{z-\mathcal{L}} \\ &= \frac{1}{z-\mathcal{L}Q}\left(z-\mathcal{L}+\mathcal{L}P\right)\frac{1}{z-\mathcal{L}} \\ &= \frac{1}{z-\mathcal{L}Q}\left(1+\mathcal{L}P\frac{1}{z-\mathcal{L}}\right) \ . \end{aligned}$$

Using Eq.(7.6) and

$$\begin{aligned} \left\langle D_\alpha^\dagger \frac{1}{z-\mathcal{L}Q} D_\beta \right\rangle &= \frac{1}{z}\left\langle D_\alpha^\dagger \left(1+\frac{1}{z}\mathcal{L}Q+\dots\right) D_\beta \right\rangle \\ &= \frac{1}{z}\left\langle D_\alpha^\dagger D_\beta \right\rangle \end{aligned}$$

one obtains Eq.(7.7).

Equation (7.7) can be rewritten in a more convenient form. Notice that

$$\begin{aligned} \left\langle D_\alpha^\dagger \frac{1}{z-\mathcal{L}Q}\mathcal{L}D_\gamma \right\rangle &= \frac{1}{z}\left\langle D_\alpha^\dagger \frac{z}{z-\mathcal{L}Q}\mathcal{L}D_\gamma \right\rangle \\ &= \frac{1}{z}\left\langle D_\alpha^\dagger \frac{z-\mathcal{L}Q+\mathcal{L}Q}{z-\mathcal{L}Q}\mathcal{L}D_\gamma \right\rangle \\ &= \frac{1}{z}\left\langle D_\alpha^\dagger \mathcal{L}D_\gamma \right\rangle + \frac{1}{z}\left\langle D_\alpha^\dagger \mathcal{L}Q\frac{1}{z-\mathcal{L}Q}\mathcal{L}D_\gamma \right\rangle \\ &= \frac{1}{z}\left\langle D_\alpha^\dagger \mathcal{L}D_\gamma \right\rangle + \frac{1}{z}\left\langle D_\alpha^\dagger \mathcal{L}Q\frac{1}{z-Q\mathcal{L}Q}Q\mathcal{L}D_\gamma \right\rangle \ , \end{aligned}$$

where we have used the fact that the projector Q is idempotent. Inserting this expression in Eq.(7.7), and multiplying with z leads to

$$z\left\langle D_\alpha^\dagger \frac{1}{z-\mathcal{L}} D_\beta \right\rangle = \left\langle D_\alpha^\dagger D_\beta \right\rangle + \sum_{\gamma,\eta}\left(\left\langle D_\alpha^\dagger \mathcal{L}D_\gamma \right\rangle + \left\langle D_\alpha^\dagger \mathcal{L}Q\frac{1}{z-Q\mathcal{L}Q}Q\mathcal{L}D_\gamma \right\rangle\right) \times \left\langle D_\gamma^\dagger D_\eta \right\rangle^{-1}\left\langle D_\eta^\dagger \frac{1}{z-\mathcal{L}} D_\beta \right\rangle \ ,$$

or, in matrix notation

$$zG = \chi + (\Omega + \Sigma)\,\chi^{-1} G \ . \tag{7.8}$$

G is the matrix of correlation functions

$$G_{\alpha\beta}(z) = \langle \Psi |\, D_\alpha^\dagger \frac{1}{z - \mathcal{L}} D_\beta \,| \Psi \rangle \ , \tag{7.9}$$

χ is the so-called susceptibility matrix

$$\chi_{\alpha\beta} = \langle \Psi |\, D_\alpha^\dagger D_\beta \,| \Psi \rangle \ , \tag{7.10}$$

Ω is called frequency matrix

$$\Omega_{\alpha\beta} = \langle \Psi |\, D_\alpha^\dagger \mathcal{L} D_\beta \,| \Psi \rangle \ , \tag{7.11}$$

and Σ is the self-energy matrix

$$\Sigma_{\alpha\beta}(z) = \langle \Psi |\, D_\alpha^\dagger \mathcal{L} Q \frac{1}{z - Q\mathcal{L}Q} Q \mathcal{L} D_\beta \,| \Psi \rangle \ . \tag{7.12}$$

Formally, Eq.(7.8) can be solved for G by inversion

$$G = \left[z - (\Omega + \Sigma)\,\chi^{-1} \right]^{-1} \chi \ . \tag{7.13}$$

This equation is the starting point for the projection technique. Remember that the operators A and B from Eq.(7.1) belong to the set of dynamic variables D_α. Therefore, one of the matrix elements of G is the correlation function (7.1). However, to obtain this matrix element, one has to solve the whole matrix equation (7.13). Note that on the r.h.s. of Eq.(7.13) the contributions from the two subspaces $\mathcal{P}$ and $\mathcal{Q}$ are neatly separated. Only the self-energy matrix Σ contains the projection operator Q. All other quantities pertain to subspace $\mathcal{P}$. Therefore, χ and Ω describe the dynamics in the "relevant" subspace $\mathcal{P}$, whereas Σ is the coupling to the "rest" subspace $\mathcal{Q}$. Furthermore, χ and Ω contain no operator fractions. Consequently, the susceptibility and frequency matrix can be calculated exactly, if $|\Psi\rangle$ and the dynamic variables D_α are known. Since, by assumption, $\mathcal{P}$ contains the most important parts of the Hilbert space, the contribution of Σ should be small. In this case it is justified to replace Σ by some approximate expression which can be calculated explicitly. There are many possibilities to obtain an approximation for the self-energy matrix [37]. For instance, one approach uses the fact that Σ has the same structure as G. Thus, we can repeat the procedure that has led to Eq.(7.13), by applying it to Σ. In this way, a new self-energy matrix is generated which can again be subjected to the

above procedure, and so on. Thus, one obtains a continued fraction which can be approximately truncated at some point.

In the present thesis a different approach will be used. It follows from Eq.(7.3) that, the larger subspace $\mathcal{P}$ is chosen, the smaller is subspace $\mathcal{Q}$ (and, consequently, the smaller is Σ). We assume that the set of dynamic variables D_α (and, therefore, $\mathcal{P}$) is sufficiently large so that the self-energy matrix can be completely neglected. In this case, Eq.(7.13) reduces to

$$G = \left[z - \Omega\chi^{-1}\right]^{-1} \chi \ . \tag{7.14}$$

By solving Eq.(7.14) one obtains the exact solution of the problem in the subspace $\mathcal{P}$. The quality of this approximation can be systematically improved by enlarging the set of dynamic variables until the results have converged. Equation (7.14) is most easily solved by diagonalizing $\Omega\chi^{-1}$ using a unitary transformation matrix U

$$\begin{aligned} G &= \left[z - \Omega\chi^{-1}\right]^{-1} \chi \\ &= U^\dagger U \left[z - \Omega\chi^{-1}\right]^{-1} U^\dagger U \chi \\ &= U^\dagger \left[z - U\Omega\chi^{-1}U^\dagger\right]^{-1} U\chi \ . \end{aligned}$$

This leads to

$$G_{\alpha\beta}(z) = \sum_{\gamma,\eta} U^\dagger_{\alpha\gamma} \frac{1}{z - \omega_\gamma} U_{\gamma\eta}\chi_{\eta\beta} \ ,$$

or

$$G_{\alpha\beta}(z) = \sum_{\gamma} \frac{W_{\alpha\beta}(\gamma)}{z - \omega_\gamma} \ , \tag{7.15}$$

with $z = \omega + i\eta$. ω_γ are the diagonal elements of $U\Omega\chi^{-1}U^\dagger$, and

$$W_{\alpha\beta}(\gamma) = U^\dagger_{\alpha\gamma} \sum_{\eta} U_{\gamma\eta}\chi_{\eta\beta} \ . \tag{7.16}$$

$W_{\alpha\beta}(\gamma)$ is the spectral weight of the excitation γ, with energy ω_γ. Note the similarity between the imaginary part of Eq.(7.15) and Eq.(2.15). In analogy to Eq.(2.15), $W_{\alpha\beta}(\gamma)$ can be interpreted as an overlap between the state $|\Psi\rangle$ and final states with index γ. Since the transformation matrix U consists of the eigenvectors of $[z - \Omega\chi^{-1}]$, we can determine the contribution of variable D_η to the final state with index γ by

$$\mathrm{contr}_\gamma(D_\eta) = |U_{\gamma\eta}|^2 \ . \tag{7.17}$$

7.2 Dynamic variables

We now use Eq.(7.14) to calculate the Cu $2p_{3/2}$ core-level spectra. According to Eqs.(2.18) and (2.19), the intensity $I(\omega)$ is proportional to the imaginary part of the single core hole correlation function

$$\begin{aligned} I(\omega) &\sim -\sum_{\xi} \mathrm{Im}\left[G^{\xi}_{00}(\omega + i0)\right] , \\ G^{\xi}_{00}(\omega + i0) &= \langle\Psi| c_{0\xi} \frac{1}{\omega + i0 - \mathcal{L}_{\mathrm{XPS}}} c^{\dagger}_{0\xi} |\Psi\rangle . \end{aligned}$$

$|\Psi\rangle$ is the ground state of Hamiltonian (2.6), and $c^{\dagger}_{0\xi}$ creates a core-hole with pseudo-spin ξ (see Chap. 2). For the projection technique, we need an appropriate set of dynamic variables D_{α}. Since we want G^{ξ}_{00} to be one of the matrix elements of the matrix of correlation functions G in Eq.(7.14), the set of dynamic variables has to include the core-hole creation operator $c^{\dagger}_{0\xi}$. Thus,

$$D_{0\xi} = c^{\dagger}_{0\xi} . \tag{7.18}$$

Additional dynamic variables may be mechanically generated by repeatedly applying $\mathcal{L}_{\mathrm{XPS}}$ onto $c^{\dagger}_{0\xi}$. However, it is more illustrative to derive the D_{α} by physical reasoning. In the case of core-level XPS, the role of the dynamic variables in the projection technique is to describe the reaction of the valence holes to the creation of the core hole. Let us for the moment again neglect the exchange interaction in Hamiltonian H_{XPS} from Eq.(2.1), i.e.: $I_{dc} = 0$. Then, the core hole affects valence holes only due to the Coulomb repulsion U_{dc} in H_{XPS}. Therefore, the dynamic reaction of the valence system will mainly consist in a delocalization of the valence hole that had previously occupied the core-hole Cu site $i = 0$. This ("dynamic") delocalization due to U_{dc} is a process that is forced upon the system from outside, in contrast to the ("static") delocalization during the fluctuation processes in the ground state. Nevertheless, both forms of delocalization occur in the Cu-O structures by means of the hopping factors t_{pd} and t_{pp}. Thus, it should be possible to describe the dynamic delocalization processes within the same framework as the static delocalization processes. Formally, this means that the dynamic variables D_{α} can be constructed using the ground-state fluctuation operators F_{α} from Sec. 4.1, and Appendices A and B

$$D_{\alpha\xi} = F_{0,\alpha} c^{\dagger}_{0\xi} , \ \alpha > 0 . \tag{7.19}$$

Physically, the $D_{\alpha\xi}$ describe the creation of a core hole with pseudo spin ξ at Cu site $i = 0$, and the subsequent delocalization of the valence hole from the

same site (via $F_{0,\alpha}$). For instance, for variable $D_{1\xi}$ the valence hole reacts to the creation of the core hole by hopping from Cu site i onto the four neighbouring O sites j

$$D_{1\xi} = -\sum_{j\sigma} \phi_{pd}^{0j} p_{j\sigma}^{\dagger} d_{0\sigma} c_{0\xi}^{\dagger} \ .$$

In the $F_{0,\alpha}$, a summation over all equivalent final sites is made (see Sec. 4.1). Therefore, the $D_{\alpha\xi}$ generate only excitations that have the same symmetry with respect to site $i = 0$ as the multi-band Hamiltonian H. This is justified, because the core-hole Hamiltonian H_c does not break this symmetry. In Sec. 7.3 we will show that already the set $\{D_0, D_1\}$ gives the exact solution for the XPS spectrum of a hole on a single CuO_4 plaquette with $I_{dc} = 0$.

In the case $I_{dc} \neq 0$, an additional kind of excitation becomes possible: Due to the non-vanishing exchange interaction, the spins of the valence hole and the core hole may be flipped. Thus, one needs a dynamic variable that describes spin flips

$$D_{0\xi}^{'} = \sum_{\sigma} d_{0,-\sigma}^{\dagger} d_{0,\sigma} c_{0,\xi+2\sigma}^{\dagger} \ . \tag{7.20}$$

$c_{0,\xi+2\sigma}^{\dagger}$ is only defined for $|\xi + 2\sigma| \leq 3/2$. Otherwise, the core-hole pseudo spin and the valence hole spin are maximally aligned and no spin-flip process is possible. In this case, no variables have to be added to Eqs.(7.18) and (7.19). In analogy to Eq.(7.19), additional dynamic variables describe the delocalization of the valence hole after the spin-flip process

$$D_{\alpha\xi}^{'} = F_{0,\alpha} \sum_{\sigma} d_{0,-\sigma}^{\dagger} d_{0,\sigma} c_{0,\xi+2\sigma}^{\dagger} \ . \tag{7.21}$$

Again, these variables are only necessary for $|\xi + 2\sigma| \leq 3/2$. In Sec. 7.4 we shall show that a set of fourteen variables gives the exact solution for the XPS spectrum of a hole on a single CuO_4 plaquette.

7.3 Calculation of matrix elements: $I_{dc} = 0$

According to Eqs.(7.10) and (7.11), the determination of the susceptibility matrix and the frequency matrix involves the evaluation of expectation values. In principle, it has already been demonstrated in Sec. 4.3 how expectation values are calculated within the ground-state formalism of part II. Therefore, in this and the following section we may restrict ourselves to a few examples.

To illustrate the usefulness of the dynamic variables from Eqs.(7.18) and (7.19), we first show that the set $\{D_0, D_1\}$ gives the exact XPS spectrum of a hole on a single CuO_4 plaquette with $I_{dc} = 0$ (see Sec. 6.1). In this case, the Cu site index i, and the pseudo-spin index ξ can be suppressed. Using the exact ground state $|\Psi\rangle$ from Eq.(3.7), we obtain the susceptibility matrix

$$\begin{aligned}
\chi &= \frac{1}{\langle\Psi \mid \Psi\rangle} \begin{pmatrix} \langle\Psi| D_0^\dagger D_0 |\Psi\rangle & \langle\Psi| D_0^\dagger D_1 |\Psi\rangle \\ \langle\Psi| D_1^\dagger D_0 |\Psi\rangle & \langle\Psi| D_1^\dagger D_1 |\Psi\rangle \end{pmatrix} \\
&= \frac{1}{\langle\Psi \mid \Psi\rangle} \begin{pmatrix} \langle\Psi| cc^\dagger |\Psi\rangle & \langle\Psi| cF_1 c^\dagger |\Psi\rangle \\ \langle\Psi| cF_1^\dagger c^\dagger |\Psi\rangle & \langle\Psi| cF_1^\dagger F_1 c^\dagger |\Psi\rangle \end{pmatrix} \\
&= \frac{1}{1+4\lambda_1^2} \begin{pmatrix} 1+4\lambda_1^2 & 4\lambda_1 \\ 4\lambda_1 & 4 \end{pmatrix} , \qquad (7.22)
\end{aligned}$$

where we have used Eq.(3.11), together with the fact that F_1 and $F_1^\dagger$ commute with c and $c^\dagger$. To calculate the frequency matrix, we have to evaluate some commutators. Using $\left[n^c, c^\dagger\right] = c^\dagger$ we obtain

$$\begin{aligned}
\mathcal{L}_{\rm XPS} c^\dagger &= \mathcal{L}_H c^\dagger + \mathcal{L}_{H_c} c^\dagger \\
&= \mathcal{L}_{H_c} c^\dagger \\
&= U_{dc} n^d c^\dagger \ .
\end{aligned}$$

Furthermore, $\left[n^d, d\right] = -d$ implies

$$\mathcal{L}_{H_c} F_1 c^\dagger = U_{dc} \left(F_1 n_d c^\dagger - F_1 c^\dagger - F_1 c^\dagger n_c \right) \ .$$

Since in the present system $F_1 n_d |\Psi\rangle = F_1 |\Psi\rangle$, and $c^\dagger n_c |\Psi\rangle = 0$, one obtains

$$\mathcal{L}_{H_c} F_1 c^\dagger |\Psi\rangle = 0 \ .$$

Therefore,

$$\begin{aligned}
\mathcal{L}_{\rm XPS} F_1 c^\dagger &= \mathcal{L}_H F_1 c^\dagger + \mathcal{L}_{H_c} F_1 c^\dagger \\
&= \left(\mathcal{L}_H F_1 \right) c^\dagger \ .
\end{aligned}$$

Consequently, the frequency matrix is

$$\begin{aligned}
\Omega &= \frac{1}{\langle\Psi \mid \Psi\rangle}\begin{pmatrix} \langle\Psi| D_0^\dagger \mathcal{L}_{\mathrm{XPS}} D_0 |\Psi\rangle & \langle\Psi| D_0^\dagger \mathcal{L}_{\mathrm{XPS}} D_1 |\Psi\rangle \\ \langle\Psi| D_1^\dagger \mathcal{L}_{\mathrm{XPS}} D_0 |\Psi\rangle & \langle\Psi| D_1^\dagger \mathcal{L}_{\mathrm{XPS}} D_1 |\Psi\rangle \end{pmatrix} \\
&= \frac{1}{\langle\Psi \mid \Psi\rangle}\begin{pmatrix} \langle\Psi| c\mathcal{L}_{\mathrm{XPS}} c^\dagger |\Psi\rangle & \langle\Psi| c\mathcal{L}_{\mathrm{XPS}} F_1 c^\dagger |\Psi\rangle \\ \langle\Psi| cF_1^\dagger \mathcal{L}_{\mathrm{XPS}} c^\dagger |\Psi\rangle & \langle\Psi| cF_1^\dagger \mathcal{L}_{\mathrm{XPS}} F_1 c^\dagger |\Psi\rangle \end{pmatrix} \\
&= \frac{1}{\langle\Psi \mid \Psi\rangle}\begin{pmatrix} U_{dc} \langle\Psi| cn^d c^\dagger |\Psi\rangle & U_{dc} \langle\Psi| c\mathcal{L}_H F_1 c^\dagger |\Psi\rangle \\ U_{dc} \langle\Psi| cF_1^\dagger n^d c^\dagger |\Psi\rangle & \langle\Psi| cF_1^\dagger \mathcal{L}_H F_1 c^\dagger |\Psi\rangle \end{pmatrix} \\
&= \frac{1}{\langle\Psi \mid \Psi\rangle}\begin{pmatrix} U_{dc} & U_{dc} \langle\Psi| \mathcal{L}_H F_1 |\Psi\rangle \\ 0 & \langle\Psi| F_1^\dagger \mathcal{L}_H F_1 |\Psi\rangle \end{pmatrix} . \qquad (7.23)
\end{aligned}$$

Expectation values like those in the second column of the last matrix have already been calculated in Sec. 3.2. In fact, the upper left matrix element is just the negative complex conjugate of the expression (3.8), which determines λ_1. Therefore, this matrix element vanishes

$$\begin{aligned}
\langle\Psi| \mathcal{L}_H F_1 |\Psi\rangle &= \langle\Psi| (\mathcal{L}_H F_1)^\dagger |\Psi\rangle^* \\
&= \langle\Psi| (HF_1 - F_1 H)^\dagger |\Psi\rangle^* \\
&= \langle\Psi| \left(F_1^\dagger H - HF_1^\dagger\right) |\Psi\rangle^* \\
&= -\langle\Psi| \mathcal{L}_H F_1^\dagger |\Psi\rangle^* \\
&= 0 ,
\end{aligned}$$

where the star symbolizes complex conjugation. On the other hand, the lower right matrix element in Eq.(7.23) can be evaluated in analogy to the calculations in Sec. 3.2, with the result

$$\Omega = \frac{1}{1 + 4\lambda_1^2}\begin{pmatrix} U_{dc} & 0 \\ 0 & 4\left(\Delta - 2t_{pp} - E_G\right) \end{pmatrix} , \qquad (7.24)$$

where

$$E_G = -4t_{pd}\lambda_1 .$$

By inserting the susceptibility and the frequency matrix from Eqs.(7.22) and (7.24) into the projection equation Eq.(7.14), one obtains the exact solution for the XPS spectrum of a hole on a single CuO_4 plaquette with $I_{dc} = 0$. A look at Fig. 6.1 illustrates why the small set $\{D_0, D_1\}$ is sufficient for the exact solution: Since the spectrum consists of only two lines, one only needs a set of two dynamic variables.

Some features of Eqs.(7.22) and (7.24) are also found in the χ- and Ω-matrices of larger systems. The first element is for all systems

$$\chi_{00} = 1 \ . \tag{7.25}$$

The other elements in the first row (or the first column) of the susceptibility matrix are

$$\chi_{0\alpha} = \frac{z_\alpha p_\alpha \lambda_\alpha}{\langle \Psi \mid \Psi \rangle} \ , \tag{7.26}$$

where z_α is the number of equivalent final sites, and p_α is the probability of the process (see Sec. 4.3). The diagonal matrix elements of χ (except $\chi_{00} = 1$) are

$$\chi_{\alpha\alpha} = \frac{z_\alpha p_\alpha}{\langle \Psi \mid \Psi \rangle} \ . \tag{7.27}$$

All other elements of the susceptibility matrix vanish. On the other hand, the first element of the frequency matrix is

$$\Omega_{00} = \frac{U_{dc}}{\langle \Psi \mid \Psi \rangle} \left(1 + 2 z_{2d} \lambda_{2d}^2 p_{2d} + z_{2s} \lambda_{2s}^2 p_{2s} \right) \ . \tag{7.28}$$

The next element is

$$\Omega_{01} = \frac{U_{dc} z_1 z_{2s} \lambda_{2s} \lambda_1 \lambda_{2d}}{\langle \Psi \mid \Psi \rangle^2} \ . \tag{7.29}$$

There is a close relationship between the remaining elements of the frequency matrix and the equations for the determination of the fluctuation strengths λ_α. The diagonal elements $\Omega_{\alpha\alpha}$ (except Ω_{00}) are the terms proportional to λ_α in the αth equation, multiplied by $(-z_\alpha) / (\lambda_\alpha \langle \Psi \mid \Psi \rangle)$ (compare Eqs.(4.27) to (4.31)). For instance, in the case of a CuO_2 plane, the comparison with Eqs.(4.27) and (4.28) gives

$$\Omega_{11} = \frac{4 (\Delta - 2t_{pp} - E_G)}{\langle \Psi \mid \Psi \rangle} + \frac{8 t_{pp} \lambda_1 \lambda_3}{\langle \Psi \mid \Psi \rangle^2} \ , \tag{7.30}$$

$$\Omega_{2s,2s} = \frac{-4 E_G}{\langle \Psi \mid \Psi \rangle} \ , \tag{7.31}$$

and so on. The off-diagonal elements of the frequency matrix (besides Ω_{01}) can be obtained in a similar fashion. Element $\Omega_{\alpha\alpha'}$ is the term proportional to $\lambda_{\alpha'}$ in the αth equation, multiplied by $(-z_\alpha) / (\lambda_{\alpha'} \langle \Psi \mid \Psi \rangle)$ (compare Eqs.(4.27) to

(4.31)). If there is no such term, the corresponding matrix element vanishes. Thus, again for the example of the CuO_2 plane one finds

$$\Omega_{1,2s} = \frac{-4t_{pd}p_{2s}}{\langle \Psi \mid \Psi \rangle} , \tag{7.32}$$

$$\Omega_{2s,3} = \frac{-8t_{pd}p_3p_{2s}}{\langle \Psi \mid \Psi \rangle} , \tag{7.33}$$

and so on.

Summarizing, it turns out that the condition (3.4) for the determination of the fluctuation strengths has additional advantages beyond those which have been discussed in Part II: All matrix elements for the projection technique (for $I_{dc} = 0$) have effectively already been calculated in Sec. 4.3. Notice, furthermore, that the vanishing lower left elements of the frequency matrix are zero because $F_\alpha^\dagger n_d \,|\Psi\rangle = 0$ (see Eq.(7.23)). In contrast, the vanishing upper right elements of Ω are zero due to condition (3.4), as we have already seen in Eq.(7.23). Therefore, condition (3.4) ensures that the frequency matrix is Hermitian (and, consequently, that its eigenvalues are real). This is a non-trivial property, if an approximate ground state is used for the calculation of the matrix elements: Let $|\varphi\rangle$ be an approximate eigenstate of H. Then, in general

$$\langle\varphi|\, HX \,|\varphi\rangle \neq \langle\varphi|\, XH \,|\varphi\rangle \ ,$$

for an operator X which is not Hermitian. However, this implies

$$\begin{aligned} \langle\varphi|\, A^\dagger \mathcal{L}_H B \,|\varphi\rangle &= \langle\varphi|\, A^\dagger HB \,|\varphi\rangle - \langle\varphi|\, A^\dagger BH \,|\varphi\rangle \\ &= \langle\varphi|\, B^\dagger HA \,|\varphi\rangle^* - \langle\varphi|\, HB^\dagger A \,|\varphi\rangle^* \\ &\neq \langle\varphi|\, B^\dagger HA \,|\varphi\rangle^* - \langle\varphi|\, B^\dagger AH \,|\varphi\rangle^* \ , \end{aligned}$$

and, therefore,

$$\langle\varphi|\, A^\dagger \mathcal{L}_H B \,|\varphi\rangle \neq \langle\varphi|\, B^\dagger \mathcal{L}_H A \,|\varphi\rangle^* \ .$$

This means that, if $|\varphi\rangle$ is only an approximate eigenstate of H, the matrix $\langle\varphi|\, D_\alpha^\dagger \mathcal{L}_H D_\beta \,|\varphi\rangle$ is in general not Hermitian. This problem is avoided in the present approach due to condition (3.4).

7.4 Calculation of matrix elements: $I_{dc} \neq 0$

For a non-vanishing exchange interaction $I_{dc} \neq 0$, the set of dynamic variables includes $D'_{0\xi}$ and $D'_{\alpha\xi}$ from Eqs.(7.20) and (7.21). Remember that one needs

these variables only if the spin directions of the core- and the valence hole make a spin flip possible, i.e. if $|\xi + 2\sigma| \leq 3/2$. Thus, if $\xi = 3/2$ and $\sigma = 1/2$, or if $\xi = -3/2$ and $\sigma = -1/2$, no additional dynamic variables are necessary to solve the problem with non-vanishing exchange interaction. In this case, the susceptibility matrix is the same as for $I_{dc} = 0$ (see Sec. 7.3). The frequency matrix also remains almost unchanged. Only in the elements Ω_{00} and Ω_{01} appear additional Ising-contributions proportional to I_{dc}

$$\Omega_{00} = \frac{U_{dc} + I_{dc}\xi\sigma}{\langle\Psi \mid \Psi\rangle} + \frac{2U_{dc}z_{2d}\lambda_{2d}^2 p_{2d}}{\langle\Psi \mid \Psi\rangle} + \frac{(U_{dc} - I_{dc}\xi\sigma)\, z_{2s}\lambda_{2s}^2 p_{2s}}{\langle\Psi \mid \Psi\rangle} , \quad (7.34)$$

$$\Omega_{01} = \frac{(U_{dc} - I_{dc}\xi\sigma)\, z_1 z_{2s}\lambda_{2s}\lambda_1\lambda_{2d}}{\langle\Psi \mid \Psi\rangle^2} . \quad (7.35)$$

Next, we consider the case $|\xi + 2\sigma| \leq 3/2$. For simplicity, we assume that in the ground state the spin of the valence hole at the core-hole Cu site is $\sigma = 1/2$. Then, we only have to take account of the values $\xi = -3/2, -1/2, 1/2$ of the core-hole pseudo spin. As in the preceding section, we start by giving the exact solution for one hole on a single CuO_4 plaquette in the formulation of the projection technique. Since the core-hole Hamiltonian H_c does not influence the susceptibility matrix, the elements of χ without spin-flip remain unchanged (cf. Eq.(7.22)). Furthermore, due to spin conservation, the subsets $\{D\}$ and $\{D'\}$ of dynamic variables do not couple in the susceptibility matrix. New non-vanishing matrix elements appear only within the block of the variables with spin flip

$$\chi = \frac{1}{1+4\lambda_1^2} \begin{pmatrix} 1+4\lambda_1^2 & 4\lambda_1 & 0 & 0 \\ 4\lambda_1 & 4 & 0 & 0 \\ 0 & 0 & \langle\Psi| D_{0\xi}^{'\dagger} D_{0\xi}^{'} |\Psi\rangle & \langle\Psi| D_{0\xi}^{'\dagger} D_{1\xi}^{'} |\Psi\rangle \\ 0 & 0 & \langle\Psi| D_{1\xi}^{'\dagger} D_{0\xi}^{'} |\Psi\rangle & \langle\Psi| D_{1\xi}^{'\dagger} D_{1\xi}^{'} |\Psi\rangle \end{pmatrix} .$$

In contrast to $D_{0\xi}$, the variable $D_{0\xi}^{'}$ requires that the Cu site is occupied. On the other hand, $D_{1\xi}^{'\dagger}$ gives a non-vanishing contribution only if applied to an empty Cu site (otherwise, $F_1^\dagger$ creates a doubly occupied Cu site, which makes a spin-flip impossible). Therefore, the off-diagonal elements in the spin-flip block vanish, and one obtains

$$\chi = \frac{1}{1+4\lambda_1^2} \begin{pmatrix} 1+4\lambda_1^2 & 4\lambda_1 & 0 & 0 \\ 4\lambda_1 & 4 & 0 & 0 \\ 0 & 0 & 1 & 0 \\ 0 & 0 & 0 & 4 \end{pmatrix} . \quad (7.36)$$

The first two elements of the frequency matrix have already been given in Eqs.(7.34) and (7.35). Besides these two elements, the sub-block with no spin flip, denoted

by Ω^n, remains unchanged

$$\begin{aligned}\Omega^n &= \frac{1}{\langle\Psi \mid \Psi\rangle}\begin{pmatrix} \langle\Psi| D_0^\dagger \mathcal{L}_{\mathrm{XPS}} D_0 |\Psi\rangle & \langle\Psi| D_0^\dagger \mathcal{L}_{\mathrm{XPS}} D_1 |\Psi\rangle \\ \langle\Psi| D_1^\dagger \mathcal{L}_{\mathrm{XPS}} D_0 |\Psi\rangle & \langle\Psi| D_1^\dagger \mathcal{L}_{\mathrm{XPS}} D_1 |\Psi\rangle \end{pmatrix} \\ &= \frac{1}{1+4\lambda_1^2}\begin{pmatrix} U_{dc} + I_{dc}\xi\sigma & 0 \\ 0 & 4\left(\Delta - 2t_{pp} - E_G\right) \end{pmatrix} .\end{aligned}$$

On the other hand, the spin-flip sub-block Ω^f is

$$\begin{aligned}\Omega^f &= \frac{1}{\langle\Psi \mid \Psi\rangle}\begin{pmatrix} \langle\Psi| D_0^{'\dagger} \mathcal{L}_{\mathrm{XPS}} D_0^{'} |\Psi\rangle & \langle\Psi| D_0^{'\dagger} \mathcal{L}_{\mathrm{XPS}} D_1^{'} |\Psi\rangle \\ \langle\Psi| D_1^{'\dagger} \mathcal{L}_{\mathrm{XPS}} D_0^{'} |\Psi\rangle & \langle\Psi| D_1^{'\dagger} \mathcal{L}_{\mathrm{XPS}} D_1^{'} |\Psi\rangle \end{pmatrix} \\ &= \frac{1}{1+4\lambda_1^2}\begin{pmatrix} U_{dc} - I_{dc}\left(\xi + 2\sigma\right)\sigma - E_G & -4t_{pd} \\ -4t_{pd} & 4\left(\Delta - 2t_{pp} - E_G\right) \end{pmatrix} .\end{aligned}$$

The coupling between these two blocks occurs only through the matrix element $\Omega_{00'} = \langle\Psi| D_0^\dagger \mathcal{L}_{\mathrm{XPS}} D_0^{'} |\Psi\rangle$

$$\Omega = \begin{pmatrix} & \Omega^n & & \frac{I_{dc} g_\xi}{1+4\lambda_1^2} & 0 \\ & & & 0 & 0 \\ \frac{I_{dc} g_\xi}{1+4\lambda_1^2} & 0 & & \Omega^f & \\ 0 & 0 & & & \end{pmatrix} . \tag{7.37}$$

g_ξ is $1/2$ times the factor of the pseudo-spin operator (see Sec. 6.2)

$$g_\xi = \begin{cases} \sqrt{3}/2 & \text{for } \xi = -3/2, 1/2 \\ 1 & \text{for } \xi = -1/2 \end{cases} . \tag{7.38}$$

Summarizing, fourteen dynamic variables are sufficient for the exact solution on a single CuO_4 plaquette. These variables are $D_{0\xi}$, $D_{1\xi}$, $D_{0\xi}^{'}$, $D_{1\xi}^{'}$ for $\xi = -3/2, -1/2, 1/2$, and $D_{0\xi}$, $D_{1\xi}$ for $\xi = 3/2$. Due to degeneracy, only four peaks appear in the spectrum (see Fig. 6.5).

Again, some of the considerations that led to Eqs.(7.36) and (7.37) remain valid for the χ- and Ω-matrices of larger systems. In the susceptibility matrix, dynamic variables without spin flip do not couple to variables with spin flip, because of spin conservation. The block of matrix elements that contains variables without spin flip is the same as in the case $I_{dc} = 0$. The first element in the block with spin flip is

$$\chi_{0'0'} = \frac{1}{\langle\Psi \mid \Psi\rangle} . \tag{7.39}$$

All off-diagonal elements of this block vanish. The diagonal elements have the same form as the diagonal elements in the block without spin flip (see Eq.(7.27)).

However, the probability factors are different, since it is now a hole with a flipped spin which delocalizes in an antiferromagnetic surrounding. For example

$$\chi_{1'1'} = \frac{z_1 p_4}{\langle \Psi \mid \Psi \rangle} , \tag{7.40}$$

$$\chi_{2s',2s'} = \frac{z_2 p_5}{\langle \Psi \mid \Psi \rangle} , \tag{7.41}$$

and so on. Note that it is not necessary to include the spin-flip variable $D'_{2d,\xi}$: Since the dynamic variables are applied to state $|\Psi\rangle$, which is antiferromagnetically ordered, the Pauli principle prevents a flipped valence spin to create a double occupancy on a neighbouring Cu site. The first two elements of the frequency matrix have already been given in Eqs.(7.34) and (7.35). Besides these two elements, the block with no spin flip in the frequency matrix remains unchanged. The coupling between this block and the block with spin flips occurs only through the element $\Omega_{00'}$

$$\Omega_{00'} = \frac{I_{dc} g_\xi}{\langle \Psi \mid \Psi \rangle} . \tag{7.42}$$

All other matrix elements outside the two blocks vanish due to spin conservation. The elements of the spin-flip block can be calculated in analogy to the elements in the block without spin flip. The only difference is that the hole that delocalizes in this case has a flipped spin.

7.5 Convergence

As described in Sec. 7.1 we assume that our set of dynamic variables is sufficiently large so that the self-energy matrix in Eq.(7.13) can be neglected. This assumption can be checked by comparing the spectra obtained with different sets of dynamic variables. If a set is large enough, the inclusion of additional dynamic variables should have no large influence on the resulting spectra. In this sense we may talk about the convergence of the projection technique with respect to the number of dynamic variables.

In the present section we will use the case of the CuO_3 chain as an example. These spectra will be discussed in detail in Sec. 8.1 . For the moment, we are only interested in the overall change of the spectrum with increasing number of variables. Figure 7.1 shows the Cu $2p_{3/2}$ XPS spectra of the infinite CuO_3 chain calculated using the projection technique. The parameters are those of set (2.9), with $\Delta = 2.7$ eV, $U_{dc} = 7.7$ eV, and $I_{dc} = -1.5$ eV. Solid lines are broadened with a Gaussian function of width $\Gamma = 1.8$ eV, dashed lines with $\Gamma = 0.2$ eV. Figure

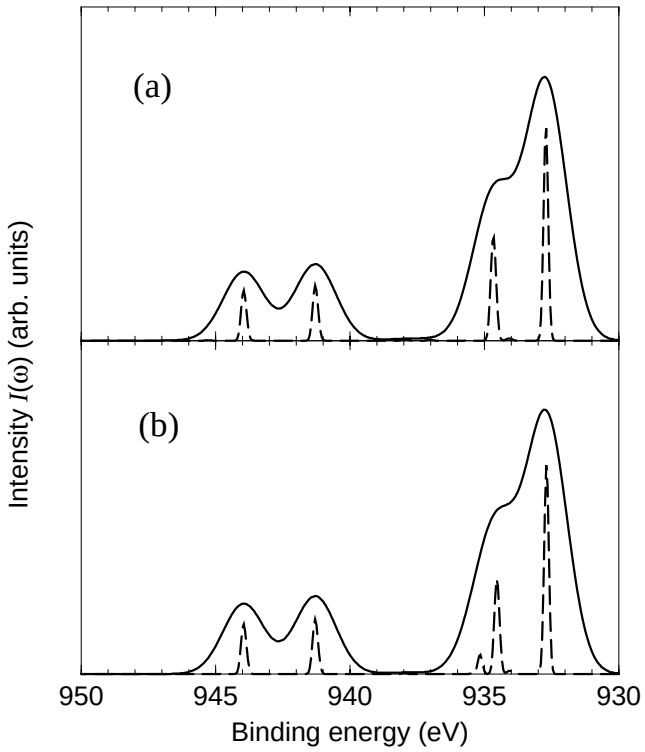

Figure 7.1: Convergence of the projection technique. The spectra for an infinite CuO_3 chain are shown with a line width of $\Gamma = 1.8$ eV (solid lines), and $\Gamma = 0.2$ eV (broken lines). (a) and (b) show the result with 40 and 70 dynamic variables, respectively.

7.1(a) shows the result with 40 dynamic variables, which allow for a delocalization to the nearest-neighbour plaquette. In Fig. 7.1(b) we show the spectrum with additional dynamic variables of the type D_5, D_6, and D_7. These variables make a delocalization to the next nearest neighbour plaquette possible. Altogether 70 dynamic variables have been used to calculate the spectrum in Fig. 7.1(b). The inclusion of the additional variables leads to a small redistribution of spectral weight around 935 eV binding energy. This change is only visible when a small line width Γ is used for the convolution of the line spectrum. For larger line width the spectrum remains unchanged. Convergence of similar good quality is observed for the case of the CuO_2 plane.

In conclusion we observe excellent convergence of the calculated spectra with respect to the number of dynamic variables. Strictly speaking, convergence alone does not completely prove the validity of the results. Convergence of the projection technique contains no information about the quality of the ground state used for the calculation of the expectation values. Furthermore, it might be conceiv-

able that the spectra could change upon inclusion of additional dynamic variables of a different kind than those discussed above. However, in view of the agreement with numerical simulations (Sec. 5.3), and the physical reasoning presented above, the convergence observed in Fig. 7.1 strongly supports the viability of the theoretical results.

Chapter 8

Infinite structures

In this chapter we calculate the Cu $2p_{3/2}$ XPS spectra of the infinite CuO_3 chain and the infinite CuO_2 plane. For this purpose we use the approach for the approximation of the ground state from Part II, and the projection technique for the calculation of the excitations from Chap. 7. The present chapter is organized as follows: In Sec. 8.1 we calculate the spectrum of the CuO_3 chain, and compare the result to experimental data for Sr_2CuO_3, as well as to some other theoretical works. Excellent agreement between theory and experiment is obtained. We discuss the influence of several model parameters, as well as the dependence on anisotropy. Section 8.1 is concluded with some remarks on the interplay of spin and charge degrees of freedom. In Sec. 8.2 the calculated spectra for the CuO_2 plane are compared to the experimental result for $Sr_2\ CuO_2Cl_2$. The agreement between theory and experiment turns out to be less satisfactory than in the case of the other cuprates. In Sec. 8.3 we discuss how the dimensionality influences charge excitations in the cuprates. Finally, an outlook concludes the Chapter. Some results of this chapter have been published in Refs. [108] and [109].

8.1 CuO_3 chain

The projection technique from Chap. 7 is now used to calculate the Cu $2p_{3/2}$ XPS spectrum of the infinite CuO_3 chain. We use up to 70 dynamic variables, and obtain excellent convergence (see Sec. 7.5). The theoretical result is then compared to the experimental spectrum of Sr_2CuO_3. For the determination of the parameter values we employ the strategy that has been explained in Sec. 6.3. This means we use the standard values from sets (2.9) and (6.5), which have been deduced from band-structure calculations and from the comparison with the spectra of Bi_2CuO_4 and Li_2CuO_2 (see Sec. 6.3), respectively.

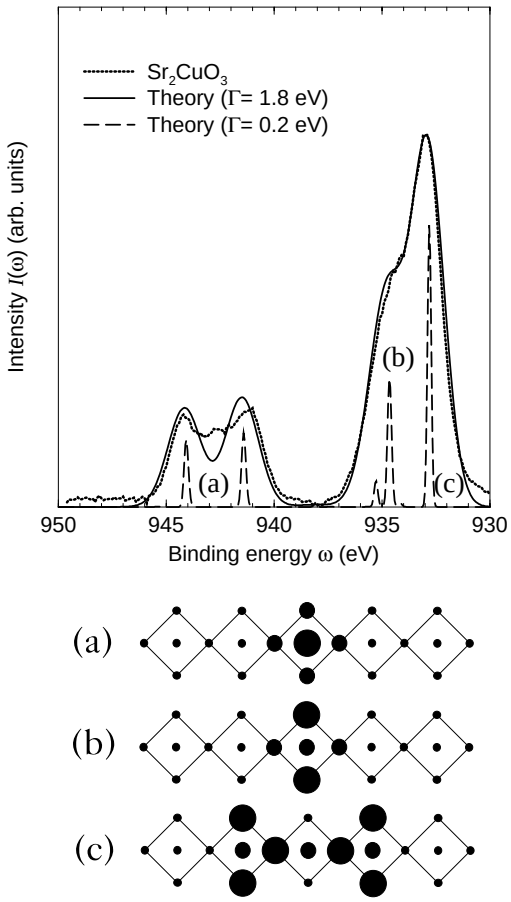

Figure 8.1: Comparison between the CuO_3 chain spectrum and the experimental result for Sr_2CuO_3 from Ref. [16]. The same theoretical spectrum is shown with two different line widths: $\Gamma = 1.8$ eV (solid line), and $\Gamma = 0.2$ eV (dashed line). The parameter values are $\Delta = 2.7$ eV and $U_{dc} = 7.7$ eV. All other values are given in sets (2.9) and (6.5). The lower part shows the final states that correspond to the peaks in the spectrum. Larger dots symbolize a larger valence hole density.

Thereby we allow for a general energy shift of ± 0.3 eV for the whole spectrum which is the experimental accuracy of the absolute energy values [16]. We vary the charge-transfer energy Δ until the theoretical value for the satellite to main-line intensity ratio is equal to the experimental one $I_s/I_m = 0.37$ (see Table 1.4). While doing so we keep the difference $U_{dc} - \Delta = 5$ eV constant. Thus, we effectively use only one single free parameter. In Fig. 8.1 the theoretical result is compared to the experimental spectrum of Sr_2CuO_3 from Ref. [16]. For $\Delta = 2.7$ eV we obtain excellent agreement between the experiment (dots) and the theoretical result with a broadening of $\Gamma = 1.8$ eV (solid line). The same theoretical result is shown with a smaller broadening $\Gamma = 0.2$ eV as well (dashed

line). This smaller line width allows to distinguish the different contributions to the theoretical spectrum. The corresponding valence hole distribution in the final states is shown in the lower part of Fig. 8.1. It has been determined using Eq.(7.17). The high-energy satellite feature (a) is found to be due to a highly local final state with a large weight at the core hole site (which is the central site in the chain fragments shown in the lower part of Fig. 8.1). This final state (a) is completely analogous to the one found for the satellite feature of the single-plaquette spectrum (Fig. 6.5). Due to the large weight at the core hole site, state (a) shows a large exchange splitting into a quintet and a triplet component (cf. Sec. 6.2).

The main line in Fig. 8.1 is found to consist of essentially two contributions. There is a higher energy shoulder (b) and a dominant lower energy feature (c). The shoulder (b) is associated with a rather local final state in which the valence hole from the core-hole Cu site has moved to the surrounding O sites. Again, this state is rather similar to the final state (b) of the single-plaquette spectrum (Fig. 6.5). The main difference is that the distribution of O weight in Fig. 8.1(b) is asymmetric, with a larger weight on the out-of chain O sites. An analogous asymmetry has been found in exact diagonalization calculations by Okada and Kotani [75]. However, in their work the in-chain part of the weight was found to move away from the central plaquette. This property is not reproduced in the present calculation, where final state (b) turns out to be essentially local. Thus, features (a) and (b) in the CuO_3 chain spectrum (Fig. 8.1) are found to be very similar to the excitations in the single-plaquette spectrum (Fig. 6.5). In contrast, peak (c) in Fig. 8.1 is associated with an excitation which is impossible in the single-plaquette system. As shown in the lower part of Fig. 8.1, in the final state (c) the valence hole delocalizes onto the nearest neighbour plaquettes. Since these plaquettes are already occupied by a hole of opposite spin direction, one might interpret this excitation as the formation of a Zhang-Rice singlet [113]. This conclusion is in principal agreement with several theoretical analyses, following the seminal work by Veenendaal, Eskes and Sawatzky [103][104] (see Sec. 2.3). The Zhang-Rice singlet in state (c) is found to be asymmetric, with more weight near the core-hole site. There are also final states that are more delocalized than state (c). One of them is connected with a delocalization to the next-nearest neighbour plaquette. This state leads to a small peak at 936 eV binding energy (visible in the dashed line in Fig. 8.1). However, these delocalized states have no significant influence on the overall spectrum, as already noticed in Sec. 7.5.

Summing up, the dominant peak (c) of the main line in the spectrum of Sr_2CuO_3 is found to be associated with a Zhang-Rice singlet-like delocalization process. While other spectral features are similar to those found in Bi_2CuO_4 and

Li_2CuO_2, this excitation is only possible in a geometry with a dimensionality larger than zero. In agreement with previous works [73] the value $\Delta = 2.7$ eV for the charge-transfer energy is found to be smaller than in Bi_2CuO_4, Li_2CuO_2, and other cuprates.

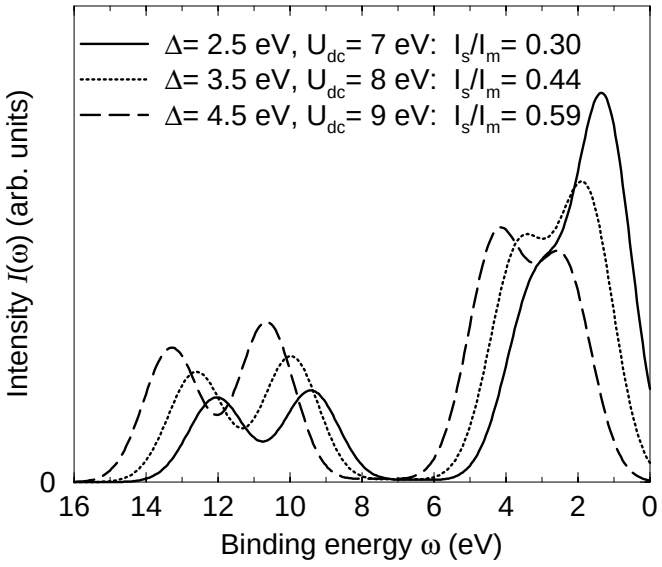

Figure 8.2: Δ- and U_{dc}-dependence of the CuO_3 chain spectrum.

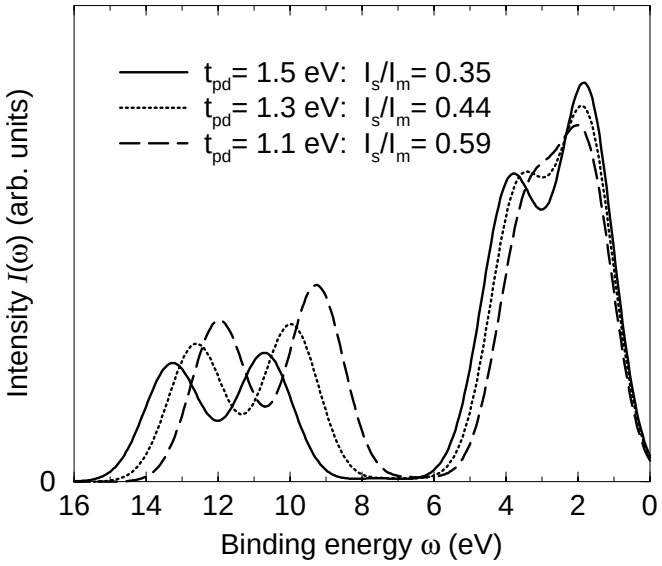

Figure 8.3: t_{pd}-dependence of the CuO_3 chain spectrum.

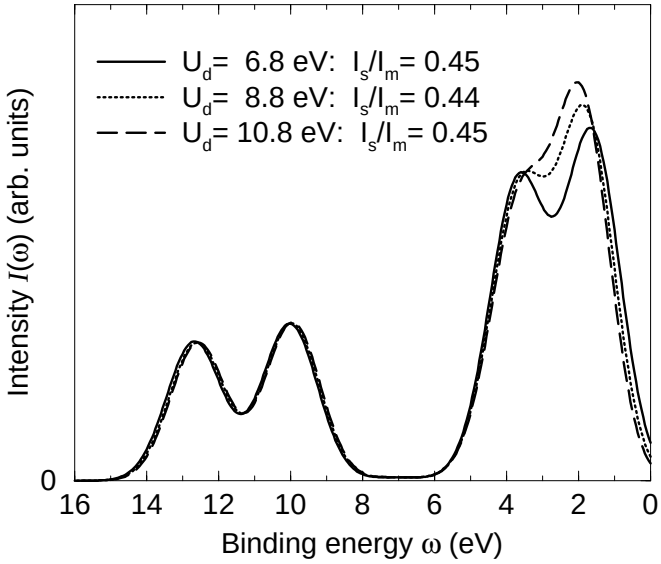

Figure 8.4: U_d-dependence of the CuO_3 chain spectrum.

Next, we discuss the parameter dependence of the CuO_3 chain spectrum. Figure 8.2 shows the Δ-dependence of the spectrum, where the difference $U_{dc} - \Delta = 5$ is kept constant. The exchange parameter is $I_{dc} = -1.5$ eV, and all other parameters are those from set (2.9). Like in the case of a single plaquette (Fig. 6.3), with increasing Δ the intensity of the satellite I_s increases relative to the intensity of the main line I_m. The explanation for this behaviour remains the same as in the case of the single plaquette: a larger value of Δ leads to a larger Cu weight in the ground state, and, consequently, to a larger overlap with the final state of the satellite. With increasing Δ both sub-peaks of the main line – the higher-energy "local" peak (b) and the lower-energy "Zhang-Rice" peak (c) – lose intensity to the satellite. However, the intensity of the "Zhang-Rice" peak decreases much stronger. This is due to the fact that the corresponding final state is more delocalized, and, therefore, is much stronger suppressed with increasing Δ. As in the case of a single plaquette (Fig. 6.3), with increasing Δ the whole spectrum shifts towards larger binding energies.

The influence of t_{pd} is shown in Fig. 8.3. The parameters for the calculation are the same as for Fig. 8.2, with $\Delta = 3.5$ eV, and $U_{dc} = 8$ eV. Since a smaller t_{pd} means a larger Cu weight in the ground state, the ratio I_s/I_m is observed to increase with decreasing t_{pd}. The influence of t_{pd} on the main line is, however, less dramatic than that of Δ (see Fig. 8.2). The "Zhang-Rice" peak loses some intensity with respect to the higher-energy "local" peak, but the energy positions of the two main-line features remain essentially unchanged. Again, this is in analogy to the results for the single plaquette (Fig. 6.4). The two sub-peaks of

the satellite (the quintet and the triplet) behave similar in both Figs. 8.2 and 8.3.

Figure 8.4 shows how the spectrum depends on the Coulomb repulsion U_d. The parameters are again the same as in Figs. 8.2 and 8.3. The satellite structure as well as the "local" shoulder of the main line are found to be practically independent of U_d. This is easy to understand: the corresponding final states do not contain any Cu double occupancies. On the other hand, states with doubly occupied Cu sites contribute to the Zhang-Rice singlet. Consequently, one finds that the intensity of the lowest energy line in Fig. 8.4 depends on U_d. Overall it can be concluded that the spectrum depends most sensitively on Δ (and U_{dc}), as shown in Fig. 8.2. There is also some dependence on t_{pd} (see Fig. 8.3). In contrast, the influence of U_d is small. Therefore, a comparison with the experiment will help to determine Δ and t_{pd}, while we cannot expect to deduce precise values for U_d from Cu $2p_{3/2}$ XPS spectra.

We now discuss the influence of anisotropy on the core-level spectra. Band-structure calculations [85] suggest that Sr_2CuO_3 is anisotropic with respect to the O sites out of chain direction ($\perp$) and in chain direction ($\parallel$). This means that its electronic structure should be modelled using two different charge transfer energies $\Delta_\perp$ and $\Delta_\parallel$, and two different Cu-O hopping strengths $t_{pd}^\perp$ and $t_{pd}^\parallel$. According to Ref. [85]: $\Delta_\perp > \Delta_\parallel$ and $t_{pd}^\perp > t_{pd}^\parallel$. Therefore, one might ask: Is it possible to deduce this anisotropy from the Cu $2p_{3/2}$ XPS spectrum? Some generalizations of our formalism are necessary to answer this question. They are explained in Appendix B. Figure 8.5 shows the influence of anisotropic charge-transfer energies on the spectrum. All other parameters are as given in the previous figures.

As $\Delta_\parallel$ increases with respect to $\Delta_\perp$, the Zhang-Rice singlet-like delocalization is suppressed. Consequently, the shoulder structure of the main line gains intensity. However, the form of the satellite and all energy positions remain practically unaffected. A similar result is found for the dependence on t_{pd} (Fig. 8.6). With decreasing $t_{pd}^\parallel$ (with decreasing delocalization) the shoulder structure of the main line grows in intensity. Again, the satellite and the energy positions remain essentially unchanged.

The results from Figs. 8.5 and 8.6 show that increasing $\Delta_\perp$ leads to the opposite result as increasing $t_{pd}^\perp$. Thus, for a simultaneous increase in $\Delta_\perp$ and $t_{pd}^\perp$, the effects should cancel each other, without any relevant influence on the spectrum. This is shown in Fig. 8.7, where again all other parameters are like in the previous figures. A simultaneous increase in $\Delta_\perp$ and $t_{pd}^\perp$ leads only to a small overall shift, but it does not affect the form of the spectrum. Thus, we may conclude that the Cu $2p_{3/2}$ XPS spectra are not sensitive to a possible electronic anisotropy in $Sr_2\ CuO_3$ of the kind suggested in Ref. [85].

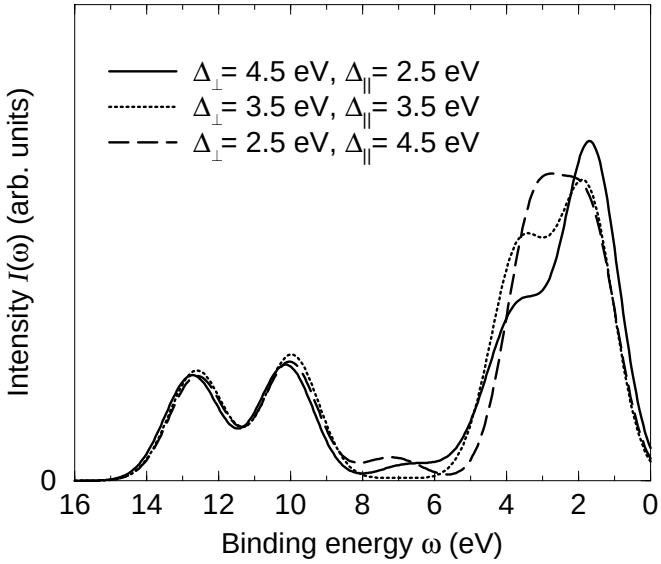

Figure 8.5: Influence of anisotropic charge transfer Δ on the CuO_3 chain spectrum.

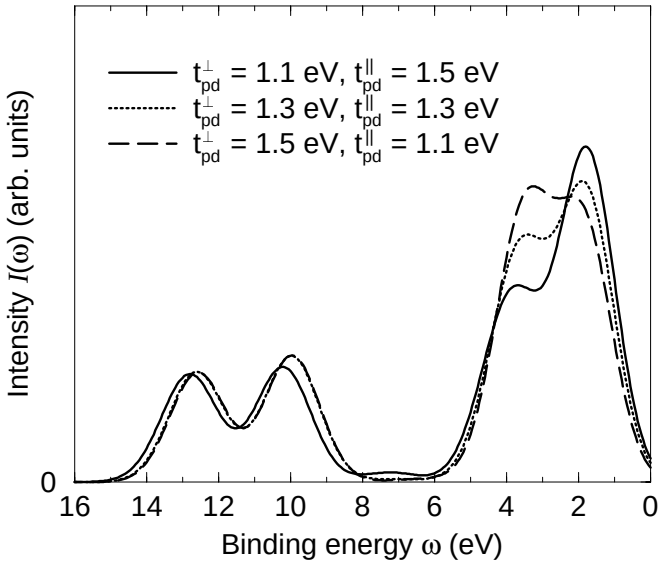

Figure 8.6: Influence of anisotropic Cu-O hopping t_{pd} on the CuO_3 chain spectrum.

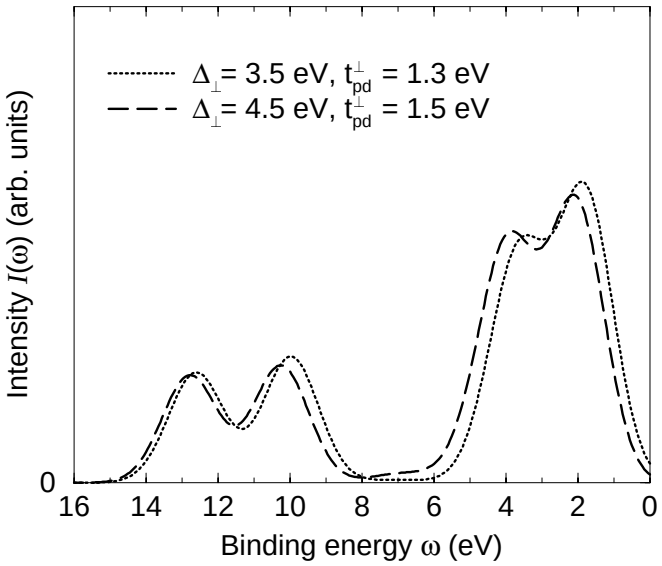

Figure 8.7: The simultaneous influences of anisotropic Δ and t_{pd} on the CuO_3 chain spectrum nearly cancel each other.

We conclude this section by a discussion of the relationship between local antiferromagnetic correlations (that is, spin degrees of freedom) and the form of the core-level spectra (charge degrees of freedom). In Fig. 8.8 we compare different theoretical results with an artificial line width $\Gamma = 0.2$ eV. The model parameters are those of set (2.9), with $\Delta = 2.5$ eV, and $U_{dc} = 7.7$ eV. For simplicity, no exchange splitting has been included ($I_{dc} = 0$).

The dashed line in Fig. 8.8(a) shows the spectrum obtained by an exact diagonalization calculation of a Cu_3O_{10} cluster (open boundary conditions), that is a system of 3 valence holes on 3 plaquettes, where the central Cu site is the core-hole site. The solid line in Fig. 8.8(a) is the solution in the presence of antiferromagnetic order which has been imposed by restricting the two holes with the same spin to the two outer plaquettes. One finds that the introduction of spin order leads to an enhancement of the shoulder structure of the main line, and to an increase of spectral weight of the satellite structure. An analogous effect results when the spin order is imposed by applying a staggered field to the Cu sites. The same behaviour is also observed for larger systems. Figure 8.8(b) shows a comparison of the spectrum obtained by exact diagonalization of a Cu_7O_{21} cluster, taken from Ref.[73] (dashed line), with the result of the projection technique for an infinite chain (solid line). Since the projection technique starts from a Néel-ordered state, it overestimates antiferromagnetic correlations. Again, this leads to a relative enhancement of the shoulder structure and the satellite, while other excitations are suppressed. However, due to its small Néel

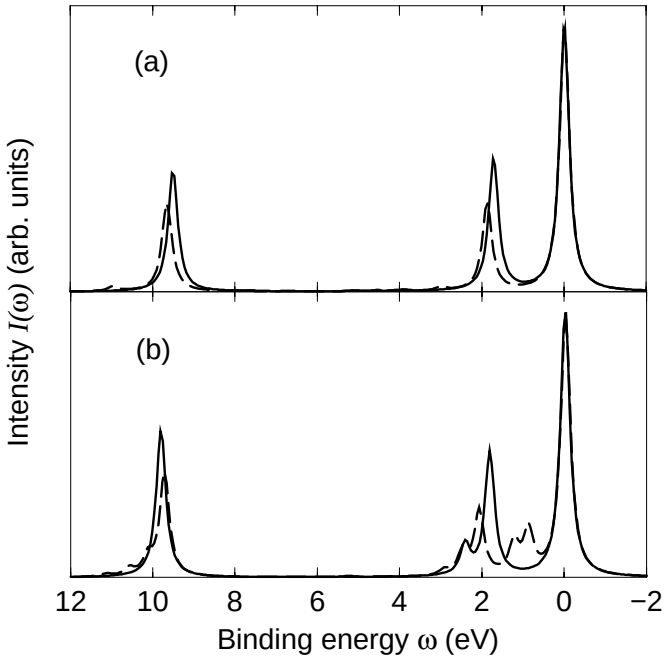

Figure 8.8: Influence of antiferromagnetic correlations for chains of different length. (a) shows the exact diagonalization of a CuO_3 cluster without (dashed line) and with (solid lines) antiferromagnetic order. (b) compares the exact diagonalization of a Cu_7O_{21} cluster from Ref.[73] (dashed line) with the result of the projection technique for an infinite chain (solid line).

temperature of 5 K it is not plausible to assume that these effects can actually be observed in the experimental spectrum of Sr_2CuO_3. The detailed form of the main line may rather be determined by polarization effects due to the presence of the core hole (see Ref. [74]).

8.2 CuO_2 plane

Since the CuO_2 plane has a higher symmetry than the CuO_3 chain, one needs less dynamic variables for the calculation of the Cu $2p_{3/2}$ XPS spectrum. We have found that 33 variables are sufficient for an excellent convergence of the spectrum. However, it turns out that a fit using the charge-transfer energy Δ like in Sec. 8.1 does not lead to a satisfying agreement with the experimental spectrum of $Sr_2CuO_2Cl_2$ from Ref.[16]. This is shown in Fig. 8.9. For parameter sets (2.9) and (6.5), with $\Delta = 3.5$ eV and $U_{dc} = 7.7$ eV (dashed line in Fig. 8.9), the

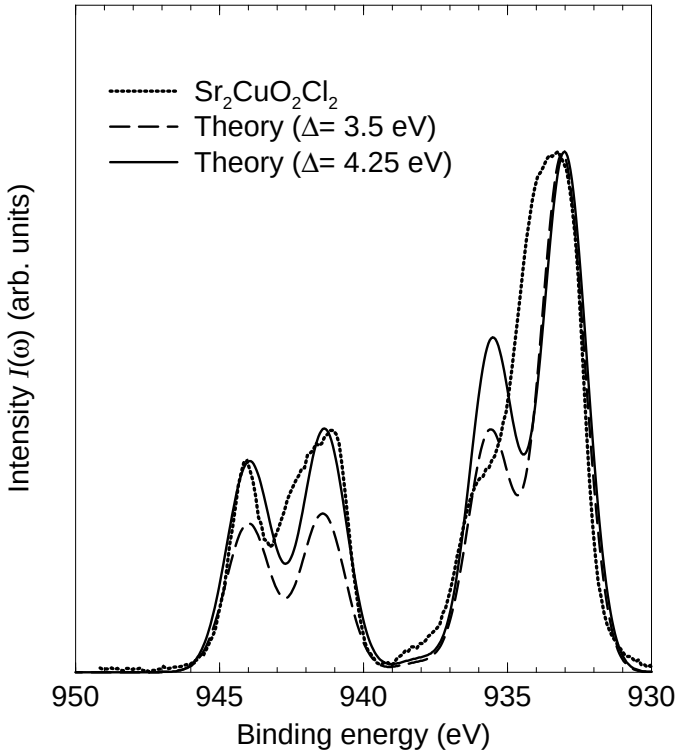

Figure 8.9: Comparison of theoretical CuO_2 plane spectra for different values of Δ and U_{dc} (solid line, dashed line) with the experimental spectrum of $Sr_2CuO_2Cl_2$ (dots) from Ref. [16].

calculated intensity ratio $I_s/I_m = 0.4$ is too small compared to the experimental value $I_s/I_m = 0.52$ (see Table 1.4). As for the single plaquette (Fig. 6.3) and the CuO_3 chain (Fig. 8.2), with increasing Δ the relative intensity of both the satellite and the shoulder structure around 935 eV binding energy increases. (All other parameter dependencies are analogous to the case of the CuO_3 chain as well. Therefore, they are not discussed in more detail.) For $\Delta = 4.25$ eV and $U_{dc} = 8.45$ eV (solid line in Fig. 8.9), the calculated ratio I_s/I_m is equal to the experimental one. However, the form of the main line is not reproduced correctly. The intensity of the shoulder structure is grossly overestimated, and a line seems to be missing around 934 eV binding energy.

In order to obtain a better fit we have varied t_{pd} and U_{dc} instead of Δ and U_{dc}. As shown in Fig. 8.10 this leads to a better agreement with the spectrum of $Sr_2CuO_2Cl_2$. For $\Delta = 3.5$ eV the experimental ratio $I_s/I_m = 0.52$ is reproduced for $t_{pd} = 1.15$ eV and $U_{dc} = 8.1$ eV. The delocalization properties of the most important final states are shown in the lower part of Fig. 8.10. They have been determined using Eq.(7.17).

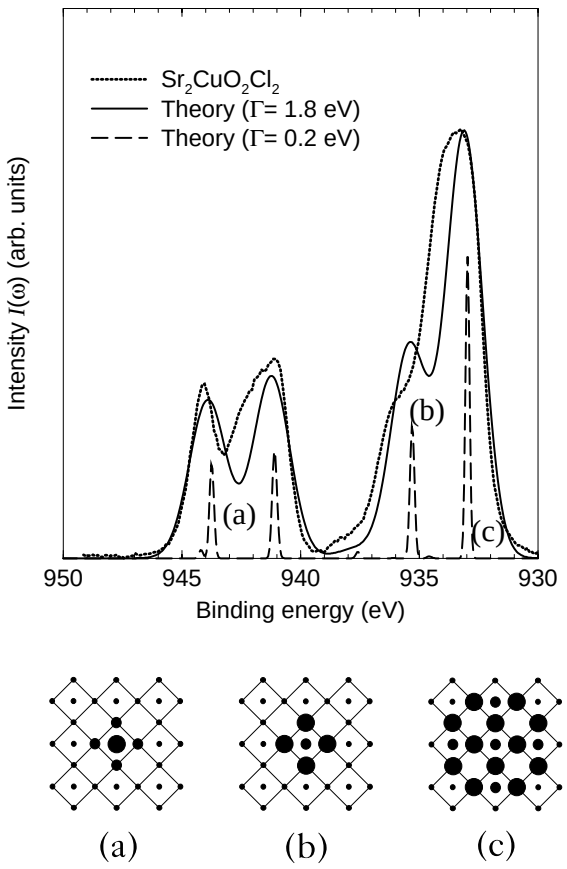

Figure 8.10: Comparison between the CuO_2 plane spectrum and the experimental result for $Sr_2CuO_2Cl_2$ from Ref. [16]. The same theoretical spectrum is shown with two different line widths: $\Gamma = 1.8$ eV (solid line), and $\Gamma = 0.2$ eV (dashed line). The parameter values are $t_{pd} = 1.15$ eV and $U_{dc} = 8.1$ eV. All other values are given in sets (2.9) and (6.5). The lower part shows the final states that correspond to the peaks in the spectrum. Larger dots symbolize a larger valence hole density.

In contrast to the zero- and one-dimensional cases, the valence hole from the core-hole site may now delocalize in two dimensions. Nevertheless, the final states obtained for a CuO_2 plane are rather similar to those of the lower dimensional systems. For state (a) this is easy to explain by the local nature of the satellite peak. The fact that the delocalization in states (b) and (c) is not significantly larger in two dimensions than in one dimension is, on the other hand, somewhat surprising. Key element in the explanation of this effect are again the four Cu sites which are the diagonal nearest neighbours of the core-hole site (cf. the lower part of Fig. 8.10). In Sec. 4.4 it was already pointed out that these diagonal sites

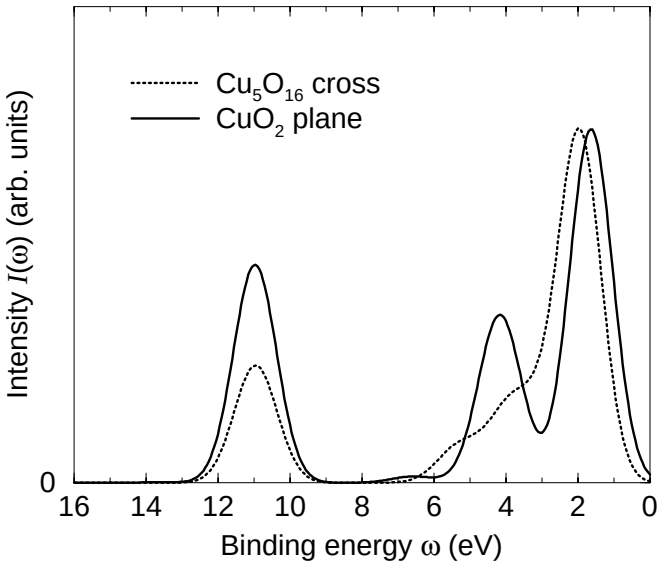

Figure 8.11: Influence of diagonal Cu sites: Comparison between the spectrum obtained by exact diagonalization of a Cu_5O_{16} cross from Ref. [15] (dots), and the result of the projection technique for an infinite CuO_2 plane (solid line).

suppress charge fluctuations: Due to antiferromagnetic correlations these sites are predominantly occupied by valence holes which have the same spin direction as the valence hole on the core-hole site. Therefore, because of the Pauli principle, the holes from the diagonal Cu sites suppress fluctuations of the valence hole from the core-hole site. The increase of charge fluctuations due to the higher dimensionality is largely compensated by this suppression.

It is interesting to compare the results of the projection technique to exact diagonalization calculations (without multiplet splitting) of a Cu_5O_{16} cluster from Ref. [15]. This cluster contains five plaquettes in a cross-like configuration where the central Cu site is the core-hole site. Notice that the Cu_5O_{16} system does not contain the diagonal Cu sites which, as discussed above, suppress fluctuations from the central Cu site. Therefore, one expects this system to display features of artificially strong delocalization like, for instance, a reduced ratio I_s/I_m. This is shown in Fig. 8.11, where the Cu_5O_{16} cross spectrum from Ref. [15] is compared to the result of the projection technique. The parameters are those of set (2.9), with $I_{dc} = 0$, $U_{dc} = 7.7$ eV, and $\Gamma = 1.4$ eV. While the diagonalization shows a similar shoulder structure as the projection technique, the intensity of this shoulder, its separation from the lowest-energy line as well as the ratio I_s/I_m are smaller.

The slightly reduced value $t_{pd} = 1.15$ eV for the Cu-O hopping parameter

which leads to the spectrum shown in Fig. 8.10 may be explained by the larger Cu-O distance in $Sr_2CuO_2Cl_2$ compared to other cuprates (see Sec. 1.2). However, from band structure calculations a value of $t_{pd} = 1.33$ eV has been obtained [85]. In any case the agreement of the theoretical result with the experimental spectrum is still not satisfactory. The calculated main line is dominated by two features, and at least one excitation seems to be missing in the region around 934 eV binding energy. The same problem has been encountered in the single-impurity approach by Karlsson, Gunnarsson, and Jepsen [54]. These results suggest the conclusion that Hamiltonian $H_{\rm XPS}$ from Eq.(2.1) still does not include all degrees of freedom that are necessary for a detailed description of the main line in the Cu $2p_{3/2}$ spectrum of $Sr_2CuO_2Cl_2$. Since all effects of the Cu-O network geometry are already included in H_{XPS}, we expect the missing third main-line feature to be a material-specific effect. This assumption, together with our conclusions about the influence of the dimensionality on the spectra, will be discussed in the next section.

8.3 Role of dimensionality

How does the dimensionality influence the electronic properties of the cuprates? We are now in the position to provide some answers to this question. Let us begin by recalling some of the results obtained for ground-state properties. As we have seen in Sec. 4.4, the step from zero dimension to higher dimensions is associated with a significant increase in ground-state fluctuations (see Tables 4.1 and 4.2). On the other hand, only small differences have been found between ground-state fluctuations in one and two dimensions. For example, the reduction of the ground-state energy from one to two dimensions amounts to only about 5% (see Fig. 5.8). It has been shown that the reason for this unexpected suppression of charge fluctuations in two dimensions are the diagonal Cu sites which are missing in the one-dimensional CuO_3 chain (see Table 4.4).

An analogous conclusion can be drawn for the influence of the dimensionality on the excitations. We observe qualitative differences between the Cu $2p_{3/2}$ core-level spectra of zero- and one-dimensional structures, but only quantitative changes between one- and two-dimensional structures. This is illustrated in Fig. 8.12 which shows the results of the projection technique for zero-, one- and two-dimensional Cu-O networks. Since the same parameter set (2.9), with $U_{dc} = 8.5$ eV and $I_{dc} = -1.5$ eV, has been used for all geometries, all changes in the spectra are exclusively due to dimensionality effects.

The most important effect is that for the one- and two-dimensional system

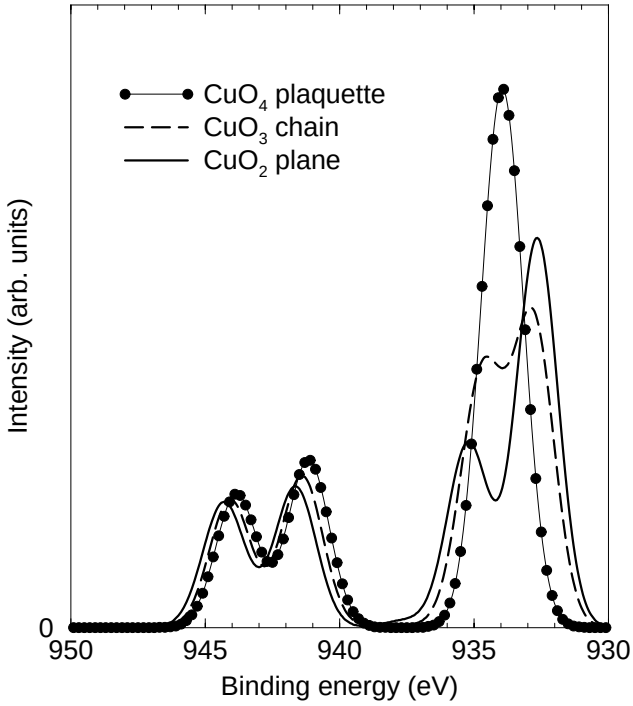

Figure 8.12: Effects of the Cu-O network dimensionality. Since the spectra of the three different Cu-O networks are shown using the same set of parameter values, all differences are exclusively due to dimensionality effects.

an additional excitation appears at lower binding energies. As discussed above the final states of this excitation are delocalized and rather similar for both the one- and the two-dimensional structure (see Figs. 8.1(c) and 8.9(c)). Overall, there is only a quantitative change from one to two dimensions, in contrast to the qualitative change observed between zero and higher dimensions. The peak around 934 eV binding energy in Fig. 8.12 that dominates the main line in the case of zero dimension becomes a shoulder structure which decreases in intensity and shifts towards higher binding energies as the dimensionality increases. Nevertheless, the final state associated with this peak preserves its main properties (a large valence-hole density at the O sites around the core-hole site) with changing dimensionality (see states (a) in Figs. 6.5, 8.1, and 8.9). As the dimensionality increases the delocalization in the Cu-O network increases as well. Therefore, one observes a monotonic decrease in the ratio I_s/I_m for increasing dimensions. Since this trend is not observed experimentally, the actual value of I_s/I_m has to depend mainly on material-specific properties. In our calculations these properties are reflected by the values of the model parameters. For all dimensions the theoretical spectra depend in a similar way on these parameters. For decreasing charge

fluctuations (larger values of Δ, smaller values of t_{pd}, t_{pp}) the satellite structure gains intensity. In the case of one and two dimensions the intensity of the "local" excitation (b) increases furthermore with respect to the "Zhang-Rice singlet" excitation (c). All spectra depend only weakly on the Coulomb interaction U_d.

Finally, we want to make some suggestions for the possible origin of the missing line around 934 eV binding energy in the theoretical CuO_2 result, as compared to the spectrum of $Sr_2CuO_2Cl_2$ (see Fig. 8.10). As mentioned before we infer from this discrepancy that the missing third main-line feature is due to a material-specific effect. Orbitals that are not yet taken into account in Hamiltonian $H_{\rm XPS}$ from Eq.(2.1) are, for instance, the non-bonding O $2p_{x(y)}$ orbitals. Choi and coworkers [20] attributed a feature in their optical spectra of $Sr_2CuO_2Cl_2$ to excitations into these orbitals. Non-planar orbitals in the CuO_2 system, like the Cu $3d_{z^2-r^2}$ orbital, are neglected in $H_{\rm XPS}$ as well. However, in view of the good agreement with the experiment shown in Figs. 6.6, 6.7, and 8.1, these orbitals do not seem necessary for the description of Bi_2CuO_4, Li_2CuO_2, and Sr_2CuO_3. It may also be possible that sites that do not belong to the CuO_2 plane (like the Cl apex site) contribute to the screening in $Sr_2CuO_2Cl_2$. However, both the large spatial distance between Cl and the CuO_2 plane (see Sec. 1.2), and the large energy difference between the Cl-3p and the Cu-3d-O-2p line in the valence photoelectron spectrum [16] suggest that screening from Cl sites should be small.

8.4 Outlook

There are many ways to proceed from here. The discussion in the last section has shown that it would be worthwhile to study systematically how the ions that do not (directly) belong to the Cu-O networks influence the Cu $2p_{3/2}$ core-level spectra. The example of the apex Cl ion in $Sr_2CuO_2Cl_2$ has already been mentioned, other examples are the O apex ions in several other cuprates (like La_2CuO_4). Furthermore, the importance of non-bonding orbitals should be checked. Another interesting problem is the calculation of Cu $2p_{1/2}$ spectra using the same model (and, hopefully, the same parameter values). The formalism presented in this work should be applicable to all these problems without principal obstacles. More generalizations in the theoretical framework will be necessary to describe the doping dependence of Cu $2p_{3/2}$ core-level spectra. From the experimental point of view, however, measurements on polycrystalline $Nd_{2-x}Ce_xCuO_4$ suggest that there is little change in the Cu $2p$ XPS as a function of doping [21]. An even more challenging task is to generalize the formalism developed in this thesis to the calculation of valence band photoemission spectra of cuprates, using a

multi-band model. This would allow a direct study of the interplay between spin and charge degrees of freedom which, as many physicists believe, should be the cornerstone of a possible explanation of high-temperature superconductivity.

Appendix A: Ground state of the CuO_3 chain

In this Appendix we derive an approximate ground state of the multi-band Hubbard Hamiltonian (2.6) at half-filling for the CuO_3 chain. A generalization to anisotropic Cu-O hopping and anisotropic Cu-O charge transfer is given in Appendix B. We use the approach that has been discussed in detail in chapters 3 and 4. Therefore, we consider only the new features that appear because of geometrical differences. The resulting equations are very similar to the case of the CuO_2 plane. The main differences are due to the reduced symmetry and the smaller number of neighbouring sites. In a CuO_3 chain, O sites which are located perpendicular to the chain direction have only one nearest-neighbour Cu site and two nearest-neighbour O sites (see Fig. A.1). Therefore, they are topologically different from the O sites that lie in chain direction (with two nearest-neighbour Cu sites and four nearest-neighbour O sites). To account for this asymmetry, we split the fluctuation operator F_1 from Eq.(4.1) into two parts $F_{1\parallel}$ and $F_{1\perp}$

$$F_{i,1\parallel} = -\sum_{j(\parallel)\sigma} \phi_{pd}^{ij} p_{j\sigma}^{\dagger} d_{i\sigma} \ , \tag{A.1}$$

$$F_{i,1\perp} = -\sum_{j(\perp)\sigma} \phi_{pd}^{ij} p_{j\sigma}^{\dagger} d_{i\sigma} \ . \tag{A.2}$$

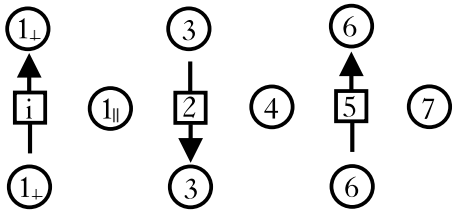

Figure A.1: Final sites reached by fluctuation operators. For reasons of symmetry only one half of the allowed fluctuation range is shown.

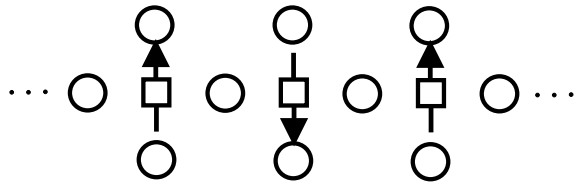

Figure A.2: The Néel-ordered ground state $|\psi_0\rangle$.

The sums are over the two O sites in chain direction and perpendicular to the chain direction, respectively (see Fig. A.1). All other fluctuation operators are defined as in the case of a CuO_2 plane, cf. Eqs.(4.3) to (4.9). The only difference is that for a CuO_3 chain the sums in these expressions contain a smaller number of final sites. These final sites are shown in Fig. A.1. For reasons of symmetry only one half of the allowed fluctuation range is shown starting from site i.

Like in Sec. 4.2 we use the fluctuation operators F_α in our ansatz for the ground state of an infinite CuO_3 chain

$$|\Psi\rangle = \exp\left(\sum_{i\alpha} \lambda_\alpha F_{i\alpha}\right) |\psi_0\rangle \ . \tag{A.3}$$

$|\psi_0\rangle$ is the Néel-ordered ground state of H_0

$$|\psi_0\rangle = \prod_i d^\dagger_{i,\sigma(i)} |0\rangle \ . \tag{A.4}$$

This state is shown in Fig. A.2. Next, we apply the approximations that have been discussed in Sects. 4.2 and 4.3. Thus, Eq.(A.3) is transformed

$$|\Psi\rangle = \exp\left(\sum_{i,\alpha>1} \lambda_\alpha F_{i\alpha}\right) \prod_{i'} \left(1 + \lambda_{1i} F_{i',1\parallel} + \lambda_{1\perp} F_{i',1\perp}\right) |\psi_0\rangle \ . \tag{A.5}$$

In analogy to Eq.(4.15) the norm of this state is $\langle \Psi \mid \Psi \rangle = \nu^N$, where N is the number of Cu sites and

$$\nu = 1 + \sum_\alpha z_\alpha p_\alpha \lambda_\alpha^2 \ . \tag{A.6}$$

z_α is again the number of equivalent final sites of the given process

$$\begin{aligned} z_{1\parallel} &= 2 \quad , \quad z_{1\perp} = 2 \quad , \quad z_{2s} = 2 \quad , \quad z_{2d} = 2 \quad , \\ z_3 &= 4 \quad , \quad z_4 = 2 \quad , \quad z_5 = 2 \quad , \quad z_6 = 4 \quad , \quad z_7 = 2 \ . \end{aligned} \tag{A.7}$$

The probabilities p_α are defined as in Sec. 4.3

$$\begin{aligned} p_{1\parallel} &= 1 \quad , \quad p_{1\perp} = 1 \quad , \quad p_{2s} = 1 - 1/\nu \quad , \quad p_{2d} = 1/\nu \quad , \\ p_3 &= 1 \quad , \quad p_4 = 1 - \lambda^2/\nu \quad , \quad p_5 = 1 - \left(1 + \lambda^2\right)/\nu \quad , \\ p_6 &= 1 - \left(1 + 2\lambda^2\right)/\nu \quad , \quad p_7 = 1 - \left(1 + 2\lambda^2\right)/\nu \quad , \end{aligned} \tag{A.8}$$

where λ is a mean on-plaquette fluctuation parameter

$$\lambda = \frac{\lambda_{1\parallel} + \lambda_{1\perp}}{2} \ . \tag{A.9}$$

The values of the parameters λ_α are determined from Eq.(3.4) for an arbitrary site $i = 0$

$$0 = \langle\Psi| \left[H, F^\dagger_{0,\alpha}\right] |\Psi\rangle \ , \ \alpha = 1, 2, \ldots \qquad . \tag{A.10}$$

One obtains the following nonlinear system of equations for $\lambda_{1\perp}, \ldots, \lambda_4$

$$\begin{aligned}
0 &= (E_G - \Delta)\,\lambda_{1\perp} + 2t_{pp}\lambda_{1\parallel} + t_{pd} \ , & \text{(A.11)}\\
0 &= (E_G - \Delta)\,\lambda_{1\parallel} + 2t_{pp}\lambda_{1\perp} + t_{pd} + t_{pd}\lambda_{2s}p_{2s} \\
&\quad + t_{pd}\lambda_{2d}p_{2d} + 2t_{pp}\lambda_3 p_3 \ , & \text{(A.12)}\\
0 &= E_G\lambda_{2s} + 4t_{pd}\lambda_{2d}\lambda/\nu + t_{pd}\lambda_{1\parallel}p_{2s} \\
&\quad + 2t_{pd}\lambda_3 p_{2s} + t_{pd}\lambda_4 p_4 p_{2s} \ , & \text{(A.13)}\\
0 &= (2E_G - U_d)\,\lambda_{2d} + 4t_{pd}\lambda_{2s}\lambda \\
&\quad + t_{pd}\lambda_{1\parallel} + 2t_{pd}\lambda_3 + t_{pd}\lambda_4 p_4 \ , & \text{(A.14)}\\
0 &= (E_G - \Delta)\,\lambda_3 + t_{pp}\lambda_{1\parallel} + t_{pd}\lambda_{2s}p_{2s} \\
&\quad + t_{pd}\lambda_{2d}p_{2d} + t_{pp}\lambda_4 p_4 \ , & \text{(A.15)}\\
0 &= (E_G - \Delta)\,\lambda_4 p_4 + t_{pd}\lambda_{2s}p_{2s}p_4 + t_{pd}\lambda_{2d}p_{2d}p_4 + 2t_{pp}\lambda_3 p_4 \\
&\quad + t_{pd}\lambda_5 p_5 + 2t_{pp}\lambda_6 p_6 - (t_{pd} + 2t_{pp}\lambda)\,\lambda\lambda_4/\nu \ . & \text{(A.16)}
\end{aligned}$$

The equations for the "far-reaching" parameters $\lambda_5, \ldots, \lambda_7$ are

$$\begin{aligned}
0 &= E_G\lambda_5 p_5 + t_{pd}\lambda_4 p_5 + 2t_{pd}\lambda_6 p_6 + t_{pd}\lambda_7 p_7 \\
&\quad - (3t_{pd} + 2t_{pp}\lambda)\,\lambda\lambda_5/\nu \ , & \text{(A.17)}\\
0 &= (E_G - \Delta)\,\lambda_6 p_6 + t_{pp}\lambda_4 p_6 + t_{pd}\lambda_5 p_6 + t_{pp}\lambda^2\lambda_7/\nu \\
&\quad - 2\,(t_{pd} + t_{pp}\lambda)\,\lambda\lambda_6/\nu \ , & \text{(A.18)}\\
0 &= (E_G - \Delta)\,\lambda_7 p_7 + t_{pd}\lambda_5 p_7 + 2t_{pp}\lambda^2\lambda_6/\nu \\
&\quad - 2\,(t_{pd} + 2t_{pp}\lambda)\,\lambda\lambda_7/\nu \ . & \text{(A.19)}
\end{aligned}$$

This system of equations, together with Eqs.(A.6) and (A.8), can be solved self-consistently for all λ_α and for ν. The solution with the lowest value of the ground-state energy per Cu site E_G is then used for the ground state. Like in Sec. 4.4, the ground-state energy E_G is

$$E_G = \frac{\langle\psi_0|\, H\, |\Psi\rangle}{\langle\psi_0 \mid \Psi\rangle} = -4t_{pd}\lambda \ . \tag{A.20}$$

	ν	$\lambda_{1\parallel}$	$\lambda_{1\perp}$	λ_{2s}	λ_{2d}	λ_3	λ_4	λ_5	λ_6	λ_7
$\Delta = 1.5$	2.63	0.60	0.48	0.40	0.18	0.21	0.15	0.06	0.03	0.01
$\Delta = 2.5$	1.97	0.48	0.40	0.30	0.13	0.13	0.09	0.03	0.01	0.01
$\Delta = 3.5$	1.59	0.38	0.33	0.21	0.09	0.09	0.05	0.02	0.01	$<$
$\Delta = 4.5$	1.38	0.31	0.28	0.16	0.07	0.06	0.03	0.01	$<$	$<$

Table A.1: Decrease of fluctuation strength with distance: ν and λ_α for different Δ. $<$ symbolizes values smaller than 0.005.

Note that there are only few differences between the above system of equations and that for the CuO_2 plane. The reduced symmetry of the CuO_3 chain has led to a splitting of Eq.(4.27) into two Eqs.(A.11) and (A.12). Since the out-of chain O site has less neighbours, the parameter $\lambda_{1\perp}$ couples only to $\lambda_{1\parallel}$. For the same reason no t_{pp}-contribution in the first term of Eq.(A.15) appears as compared to Eq.(4.30). All other changes are caused by the absence of diagonal Cu sites. Thus, p_3 is equal to 1 and the negative terms from Eqs.(4.27) and (4.30) are missing in Eqs.(A.12) and (A.15). We finally note that the last positive term in Eqs.(A.18) and (A.19) has been slightly simplified.

Table A.1 shows ν and the λ_α that are obtained from Eqs.(A.11) to (A.19) for parameter set (2.9) with several different values for Δ. Like in the case of a CuO_2 plane (Sec. 4.4) we observe a rapid decrease of the fluctuation strengths with increasing distance. This means that the neglect of far-reaching fluctuations and many-body effects is justified in the case of a CuO_3 chain as well. Therefore, we will usually neglect fluctuations beyond F_4.

Ground-state properties of the CuO_3 chain may now be calculated in analogy to the case of the CuO_2 plane, Eqs.(4.23) to (4.26). The Cu-occupation number is

$$\langle n_{Cu} \rangle = \frac{\langle \Psi | \, n_i^d \, | \Psi \rangle}{\langle \Psi \mid \Psi \rangle} = \frac{1}{\nu} \left(1 + 2\lambda_{2s}^2 p_{2s} + 2\lambda_{2d}^2 p_{2d} \right) \ . \tag{A.21}$$

The O-occupation numbers are

$$\left\langle n_O^\perp \right\rangle = \frac{\langle \Psi | \, n_i^{p\perp} \, | \Psi \rangle}{\langle \Psi \mid \Psi \rangle} = \frac{1}{\nu} \left(\lambda_{1\perp}^2 + 2\lambda_3^2 \right) \tag{A.22}$$

and

$$\left\langle n_O^\parallel \right\rangle = \frac{\langle \Psi | \, n_i^{p\parallel} \, | \Psi \rangle}{\langle \Psi \mid \Psi \rangle} = \frac{2}{\nu} \left(\lambda_{1\parallel}^2 + \lambda_4^2 p_4 \right) \ . \tag{A.23}$$

As in the case of the CuO_2 plane the number of holes is conserved, i.e. $\langle n_{Cu} \rangle +$

$2\left\langle n_O^{\perp}\right\rangle + \left\langle n_O^{\parallel}\right\rangle = 1$. The double occupancies of Cu and O sites are

$$\langle d_{Cu}\rangle = \frac{\langle\Psi|\, n_{i\uparrow}^{d} n_{i\downarrow}^{d}\,|\Psi\rangle}{\langle\Psi\mid\Psi\rangle} = \frac{1}{\nu}\left(2\lambda_{2d}^{2} p_{2d}\right) \ , \tag{A.24}$$

and

$$\left\langle d_O^{\perp}\right\rangle = \frac{\langle\Psi|\, n_{i\uparrow}^{p\perp} n_{i\downarrow}^{p\perp}\,|\Psi\rangle}{\langle\Psi\mid\Psi\rangle} = \frac{1}{4}\left\langle n_O^{o}\right\rangle^{2} \ , \tag{A.25}$$

$$\left\langle d_O^{\parallel}\right\rangle = \frac{\langle\Psi|\, n_{i\uparrow}^{p\parallel} n_{i\downarrow}^{p\parallel}\,|\Psi\rangle}{\langle\Psi\mid\Psi\rangle} = \frac{1}{4}\left\langle n_O^{\parallel}\right\rangle^{2} \ . \tag{A.26}$$

Appendix B: Ground state of the anisotropic CuO_3 chain

Band-structure calculations [85] suggest that Sr_2CuO_3 is anisotropic with respect to the O sites out of chain direction ($\perp$) and in chain direction ($\parallel$). This means that its electronic structure should be modelled using two different charge-transfer energies $\Delta_\perp$ and $\Delta_\parallel$ and two different Cu-O hopping strengths $t_{pd}^\perp$ and $t_{pd}^\parallel$. Therefore, it is interesting to investigate the ground-state properties of an anisotropic CuO_3 chain, also in view of a possible importance of the anisotropy for the calculation of core-level photoemission spectra.

Only a small number of changes is necessary to describe the ground state of the anisotropic CuO_3 chain. We use the same fluctuation operators as in Appendix A. The equations (A.5) to (A.9) for the ground state $|\Psi\rangle$, its norm ν^N, and the probabilities p_α remain unchanged. Again, we use a mean on-plaquette fluctuation parameter λ

$$\lambda = \frac{\lambda_{1\parallel} + \lambda_{1\perp}}{2} \; .$$

For reasons of simplicity we introduce a mean hopping strength t

$$t = \frac{t_{pd}^\parallel + t_{pd}^\perp}{2} \; .$$

Furthermore we assume that the ground-state energy E_G is given by

$$E_G = -4t\lambda \; .$$

Equation (3.4) leads to the following equations for the determination of $\lambda_{1o}, \ldots, \lambda_4$

$$
\begin{aligned}
0 &= (E_G - \Delta_\perp)\,\lambda_{1\perp} + 2t_{pp}\lambda_{1\parallel} + t_{pd}^{\perp}\ , && \text{(B.1)}\\
0 &= \left(E_G - \Delta_\parallel\right)\lambda_{1\parallel} + 2t_{pp}\lambda_{1\perp} + t_{pd}^{\parallel} + t_{pd}^{\parallel}\lambda_{2s}p_{2s} \\
&\quad + t_{pd}^{\parallel}\lambda_{2d}p_{2d} + 2t_{pp}\lambda_3 p_3\ , && \text{(B.2)}\\
0 &= E_G\lambda_{2s} + 4t\lambda_{2d}\lambda/\nu + t_{pd}^{\parallel}\lambda_{1\parallel}p_{2s} \\
&\quad + 2t_{pd}^{\perp}\lambda_3 p_{2s} + t_{pd}^{\parallel}\lambda_4 p_4 p_{2s}\ , && \text{(B.3)}\\
0 &= (2E_G - U_d)\,\lambda_{2d} + 4t\lambda_{2s}\lambda \\
&\quad + t_{pd}^{\parallel}\lambda_{1\parallel} + 2t_{pd}^{\perp}\lambda_3 + t_{pd}^{\parallel}\lambda_4 p_4\ , && \text{(B.4)}\\
0 &= (E_G - \Delta_\perp)\,\lambda_3 + t_{pp}\lambda_{1\parallel} + t_{pd}^{\perp}\lambda_{2s}p_{2s} \\
&\quad + t_{pd}^{\perp}\lambda_{2d}p_{2d} + t_{pp}\lambda_4 p_4\ , && \text{(B.5)}\\
0 &= \left(E_G - \Delta_\parallel\right)\lambda_4 p_4 + t_{pd}^{\parallel}\lambda_{2s}p_{2s}p_4 + t_{pd}^{\parallel}\lambda_{2d}p_{2d}p_4 + 2t_{pp}\lambda_3 p_4 \\
&\quad + t_{pd}^{\parallel}\lambda_5 p_5 + 2t_{pp}\lambda_6 p_6 - (t + 2t_{pp}\lambda)\,\lambda\lambda_4/\nu\ . && \text{(B.6)}
\end{aligned}
$$

The equations for the "far-reaching" parameters $\lambda_5, \ldots, \lambda_7$ are

$$
\begin{aligned}
0 &= E_G\lambda_5 p_5 + t_{pd}^{\parallel}\lambda_4 p_5 + 2t_{pd}^{\perp}\lambda_6 p_6 + t_{pd}^{\parallel}\lambda_7 p_7 \\
&\quad - (3t + 2t_{pp}\lambda)\,\lambda\lambda_5/\nu\ , && \text{(B.7)}\\
0 &= (E_G - \Delta_\perp)\,\lambda_6 p_6 + t_{pp}\lambda_4 p_6 + t_{pd}^{\perp}\lambda_5 p_6 + t_{pp}\lambda^2\lambda_7/\nu \\
&\quad - 2\,(t + t_{pp}\lambda)\,\lambda\lambda_6/\nu\ , && \text{(B.8)}\\
0 &= \left(E_G - \Delta_\parallel\right)\lambda_7 p_7 + t_{pd}^{\parallel}\lambda_5 p_7 + 2t_{pp}\lambda^2\lambda_6/\nu \\
&\quad - 2\,(t + 2t_{pp}\lambda)\,\lambda\lambda_7/\nu\ . && \text{(B.9)}
\end{aligned}
$$

The equations for the occupation numbers and double occupancies are the same as in the isotropic case, see Eqs.(A.21) to (A.26).

Appendix C: Projector Quantum Monte Carlo

The Projector Quantum Monte Carlo (PQMC) method is a numerical approach which allows to calculate approximately ground-state properties of finite clusters. For reviews of this method see Refs. [106] and [45]. In the PQMC approach, the ground state $|\Psi\rangle$ of a finite cluster is projected out from a suitable trial state $|\psi_{\rm trial}\rangle$ by applying an exponential projection operator

$$|\Psi\rangle = \lim_{\beta\to\infty} \frac{e^{-\beta H}\,|\psi_{\rm trial}\rangle}{\sqrt{\langle\psi_{\rm trial}|\,e^{-2\beta H}\,|\psi_{\rm trial}\rangle}}\ . \tag{C.1}$$

Here, β is a projection parameter and *not* the inverse physical temperature. Ground-state expectation values are calculated from

$$\langle A\rangle = \lim_{\beta\to\infty} \frac{\langle\psi_{\rm trial}|\,e^{-\beta H}Ae^{-\beta H}\,|\psi_{\rm trial}\rangle}{\langle\psi_{\rm trial}|\,e^{-2\beta H}\,|\psi_{\rm trial}\rangle}\ . \tag{C.2}$$

The trial state $|\psi_{\rm trial}\rangle$ has to have a non-zero overlap with the real ground state. A convenient choice for $|\psi_{\rm trial}\rangle$ is a linear combination of one-particle functions in form of a Slater determinant, for example in position space

$$\begin{aligned} |\psi_{\rm trial}\rangle &= \left|\psi^{\uparrow}_{\rm trial}\right\rangle \otimes \left|\psi^{\downarrow}_{\rm trial}\right\rangle\ , \\ |\psi^{\sigma}_{\rm trial}\rangle &= \prod_{\nu=1}^{N_\sigma}\left(\sum_{i=1}^{L}\chi^{\sigma}_{\nu,i}c^{\dagger}_{i,\sigma}\right)|0\rangle\ . \end{aligned} \tag{C.3}$$

N_σ is the number of particles with spin σ, and L is the number of sites in the cluster. $c^{\dagger}_{i,\sigma}$ creates a particle with spin σ on site i. The coefficient $\chi^{\sigma}_{\nu,i}$ is the probability to find particle ν at site i. $\chi^{\sigma}_{\nu,i}$ is a non-singular matrix (Pauli principle). In principle, the formalism described above is exact. However, for a numerical implementation one faces three problems which will make approximations necessary.

The first problem is that only finite values of the parameter β are accessible. Therefore, the limit $\beta\to\infty$ in Eq.(C.1) cannot be carried out numerically.

Nevertheless, a reasonable approximation should be obtained for large, but finite, values of β (in our case, we use values up to $\beta = 12$). The quality of this approximation can be judged from the convergence of the results with respect to β.

The second problem is that we (usually) do not know the eigenstates of H since it is neither diagonal in position space nor in momentum space. Generally, if $(A)_{ij}$ is a diagonal matrix, $\left(e^A\right)_{ij}$ is a diagonal matrix as well, with $\left(e^A\right)_{ij} = e^{A_{ij}}$. However, if A is not diagonal, then e^A is an infinite series of matrices which cannot be handled numerically. One way to circumvent this problem is to split H into a part K which is diagonal in momentum space, and a part V which is diagonal in position space. Then, $e^{-\beta H}$ may be approximately factorized using the symmetric Trotter-Suzuki formula [100]

$$e^{-\beta(K+V)} = \left(e^{\frac{-\beta}{2m}K} e^{\frac{-\beta}{m}V} e^{\frac{-\beta}{2m}K}\right)^m + \mathcal{O}\left(\beta^3/m^2\right) \ , \tag{C.4}$$

where m is the number of the so-called Trotter slices. The operator $e^{\frac{-\beta}{2m}K}$ can be evaluated by diagonalizing the hopping part of the Hamiltonian. The operator $e^{\frac{-\beta}{m}V}$, on the other hand, is already diagonal in position space. The approximate factorization of Eq.(C.4) becomes better when larger numbers of Trotter slices m are used (in our case we use values up to $m = 256$). Furthermore, since the error in Eq.(C.4) is of the order (β^3/m^2), larger values of β have to be compensated by larger values of m.

At this point one has to overcome a technical obstacle. The operator $e^{\frac{-\beta}{2m}K}$ is the exponential of a one-particle operator. Therefore, it maps a Slater determinant of the form (C.3) back onto a single Slater determinant [98]. The operator $e^{\frac{-\beta}{m}V}$, on the other hand, creates states that are linear combinations of Slater determinants. This is due to terms in V that are quadratic in the densities. Thus, in order to keep the formalism transparent, it is useful to factorize these terms. This can be achieved exactly, using the discrete Hubbard-Stratonovich transformation (for positive U) of Hirsch [46]

$$\exp\left(\frac{-\beta}{m}U\sum_{i,\sigma} n_i^\sigma n_i^{\overline{\sigma}}\right) = \prod_i \frac{1}{2}\sum_{\xi=\pm 1}\prod_\sigma \exp\left(\left(2\lambda\xi\sigma - \frac{\beta}{m}U\right)n_i^\sigma\right) \ . \tag{C.5}$$

λ is defined by

$$\cosh\left(2\lambda\right) = \exp\left(\frac{\beta}{m}U\right) \ .$$

In this way one always maps Slater determinants back onto Slater determinants. However, one now has to evaluate sums over auxiliary variables ξ

$$e^{-\beta H}\left|\psi_{\text{trial}}\right\rangle = \sum_\alpha \left|\psi\left(\alpha\right)\right\rangle \ .$$

Here, α is a m-dimensional configuration vector which represents a set of values of the ξ. $|\psi(\alpha)\rangle$ is the contribution of configuration α to the ground state.

Finally, the third (and most fundamental) problem is the extremely high dimensionality of the configuration space, even for relatively small clusters. Formally, this high dimensionality is reflected by the enormous number of sums over ξ which one has to evaluate. For every Trotter slice in Eq.(C.4) which is applied onto the trial state $|\psi_{\text{trial}}\rangle$, the resulting state "spreads" into the vast configuration space. The way in which this problem is handled in the PQMC is to evaluate the sums over ξ statistically. Thus, instead of calculating all sums, one creates a sufficiently large number of configurations (α, α'), i.e. different sets of values of the ξ for both bra $\langle\psi(\alpha)|$ and ket vectors $|\psi(\alpha')\rangle$. The final expectation value $\langle A\rangle$ is then the mean value of the expectation values $\langle A(\alpha,\alpha')\rangle$ in each configuration

$$\langle A\rangle = \frac{\sum_{\alpha,\alpha'} \langle A(\alpha,\alpha')\rangle\, g(\alpha,\alpha')}{\sum_{\alpha,\alpha'} g(\alpha,\alpha')} \;, \tag{C.6}$$

where

$$\langle A(\alpha,\alpha')\rangle = \frac{\langle\psi(\alpha)|\, A\, |\psi(\alpha')\rangle}{\langle\psi(\alpha)\mid\psi(\alpha')\rangle} \;.$$

The weight g in Eq.(C.6) is used to improve the convergence of the calculation (in the sense of an importance sampling). It is defined by

$$g(\alpha,\alpha') = \langle\psi(\alpha)\mid\psi(\alpha')\rangle \;.$$

Technically, the configurations (α,α') are created as follows. One starts with a randomly selected configuration $(1,1')$. A new random configuration $(2,2')$ is accepted with probability

$$p = \begin{cases} 1 & \cdots \quad |g(2,2')| > |g(1,1')| \\ |g(2,2')/g(1,1')| & \cdots \quad \text{otherwise} \end{cases} \;.$$

In this way one creates a Markov chain of configurations which approximates the distribution $|g|$ with increasing length. In our case we use several thousand configurations. In contrast to the former two approximations (which involve the parameters β and m), the error that is made in the third approximation is statistical. It is usually displayed in the form of an error bar.

Summing up, PQMC is a powerful numerical tool to calculate ground-state properties of finite clusters. Its inherent approximations can be systematically improved by enlarging the projection parameter β, the number of Trotter slices m, and the number of configurations used in the statistical evaluation of the sums

over ξ. In certain cases the quality of the statistical results can deteriorate when the denominator in Eq.(C.6) becomes too small. This is the so-called sign problem [23] which originates from the fact that $g(\alpha, \alpha')$ is a complex number, and that, therefore, different contributions in the denominator of Eq.(C.6) may cancel each other. Finally, since in the PQMC results for finite clusters are extrapolated to infinite systems, one has to carefully check the numerical results for finite-size effects.

Bibliography

[1] A. Aharony, R. J. Birgenau, A. Coniglio, M. A. Kastner, and H. E. Stanley, Phys. Rev. Lett. **60**, 1330 (1988).

[2] M. Ain, G. Dhalenne, O. Guiselin, B. Hennion, and A. Revcolevschi, Phys. Rev. B **47**, 8167 (1993).

[3] C. Almasan and M. B. Maple, *Chemistry of High-Temperature Superconductors*, edited by C. M. Rao (World Scientific, Singapore 1991).

[4] T. Ami, M. K. Crawford, R. L. Harlow, Z. R. Wang, D. C. Johnston, Q. Huang, and R. W. Erwin, Phys. Rev. B **51**, 5994 (1995).

[5] S. Atzkern, M. Knupfer, M. S. Golden, J. Fink, C. Waidacher, J. Richter, K. W. Becker, N. Motoyama, H. Eisaki, and S. Uchida, submitted to Phys. Rev. B.

[6] G. Baumgärtel, J. Schmalian, and K.-H. Bennemann, Phys. Rev. B **48**, 3983 (1993).

[7] A. Beatrici and M. A. Gusmão, Phys. Rev. B **51**, 7508 (1995).

[8] K. W. Becker and P. Fulde, Z. Phys. B **72**, 423 (1988).

[9] K. W. Becker and W. Brenig, Z. Phys. B **79**, 195 (1990).

[10] K. W. Becker, W. Brenig, and P. Fulde, Z. Phys. B **81**, 165 (1990).

[11] J. G. Bednorz and K. A. Müller, Z. Phys. B **64**, 189 (1986).

[12] H. Bethe, Z. Phys. **71**, 205 (1931).

[13] A. Bhattacharya and C. S. Wang, Phys. Rev. B **48**, 13949 (1993).

[14] T. Böske, private communication.

[15] T. Böske, O. Knauff, R. Neudert, M. Kielwein, M. Knupfer, M. S. Golden, J. Fink, H. Eisaki, S. Uchida, K. Okada, and A. Kotani, Phys. Rev. B **56**, 3438 (1997).

[16] T. Böske, K. Maiti, O. Knauff, K. Ruck, M. S. Golden , G. Krabbes, J. Fink, T. Osafune, N. Motoyama, H. Eisaki, and S. Uchida, Phys. Rev. B **57**, 138 (1998).

[17] J. C. Bonner and M. E. Fisher, Phys. Rev. **135**, A640 (1964).

[18] W. Brenig, Phys. Rep. **251**, 153 (1995).

[19] G. Chiaia, M. Qvarford, I. Lindau, S. Söderholm, U. O. Karlsson, S. A. Flodström, L. Leonyuk, A. Nilsson, and N. Mårtensson, Phys. Rev. B **51**, 1213 (1995).

[20] H. S. Choi, Y. S. Lee, T. W. Noh, E. J. Choi, Y. Bang, and Y. J. Kim, Phys. Rev. B **60**, 4646 (1999).

[21] T. R. Cummins and R. G. Egdell, Phys. Rev. B **48** , 6556 (1993).

[22] E. Dagotto, Rev. Mod. Phys. **66**, 763 (1994).

[23] H. De Raedt and A. Lagendijk, Phys. Rev. Lett. **46**, 47 (1981).

[24] G. Dopf, A. Muramatsu, and W. Hanke, Phys. Rev. B **41**, 9264 (1990).

[25] G. Dopf, J. Wagner, P. Dieterich, A. Muramatsu, and W. Hanke, Phys. Rev. Lett. **68**, 2082 (1992).

[26] S.-L. Drechsler, J. Málek, S. Zališ, and K. Rosciszewski, Phys. Rev. B **53**, 11328 (1996).

[27] S.-L. Drechsler, J. Málek, and H. Eschrig, Phys. Rev. B **55**, 606 (1997).

[28] S.-L. Drechsler, unpublished.

[29] V. J. Emery, Phys. Rev. Lett. **58**, 2794 (1987).

[30] V. J. Emery and G. Reiter, Phys. Rev. B **38**, 4547 (1988).

[31] H. Eskes, L. H. Tjeng, and G. A. Sawatzky, Phys. Rev. B **41**, 288 (1990).

[32] H. Eskes and G. A. Sawatzky, Phys. Rev. B **43**, 119 (1991).

[33] A. J. Fedro, Yu Zhou, T. C. Leung, B. N. Harmon, and S. K. Sinha, Phys. Rev. B **46**, 14785 (1992).

[34] J. Fink, Adv. Electron Phys. **75**, 121 (1989).

[35] A. Fujimori, F. Minami, and S. Sugano, Phys. Rev. B **29**, 5225 (1984).

[36] A. Fujimori, E. Takayama-Muromachi, Y. Uchida, and B. Okai, Phys. Rev. B **35**, 8814 (1987).

[37] P. Fulde, *Electron Correlations in Molecules and Solids* (Springer, Berlin, third edition 1995).

[38] J. Ghijsen, L. H. Tjeng, J. van Elp, H. Eskes, J. Westerink, G. A. Sawatzky, and M. T. Czyzyk, Phys. Rev. B **38**, 11322 (1988).

[39] A. Goldoni, U. del Pennino, F. Parmigiani, L. Sangaletti, and A. Revcolevschi, Phys. Rev. B **50**, 10435 (1994).

[40] J. B. Grant and A. K. McMahan, Phys. Rev. B **46**, 8440 (1992).

[41] M. Greven, R. J. Birgeneau, Y. Endoh, M. A. Kastner, B. Keimer, M. Matsuda, G. Shirane, and T. R. Thurston, Phys. Rev. Lett. **72**, 1096 (1994).

[42] O. Gunnarsson and K. Schönhammer, Phys. Rev. Lett. **50**, 604 (1983).

[43] O. Gunnarsson and K. Schönhammer, Phys. Rev. B **28**, 4315 (1983).

[44] A. Brooks Harris and R. V. Lange, Phys. Rev. B **157**, 295 (1967).

[45] R. E. Hetzel, to be published.

[46] J. E. Hirsch, Phys. Rev. B **28**, 4059 (1983).

[47] J. Hubbard, Proc. R. Soc. A **276**, 238 (1963).

[48] A. Hübsch, unpublished.

[49] S. Hüfner, *Photoelectron Spectroscopy* (Springer, Berlin, second edition 1996).

[50] L. Hulthén, Ark. Met. Astron. Fysik **26A**, No.11 (1938).

[51] M. S. Hybertsen, M. Schlüter, and N. E. Christensen, Phys. Rev. B **39**, 9028 (1989).

[52] Y. Kakehashi, K. Becker, and P. Fulde, Phys. Rev. B **29**, 16 (1984).

[53] K. Karlsson, O. Gunnarsson, and O. Jepsen, J. Phys.: Condens. Matter **4**, 2801 (1992).

[54] K. Karlsson, O. Gunnarsson, and O. Jepsen, Phys. Rev. Lett. **82**, 3528 (1999).

[55] A. Keren, L. P. Le, G. M. Luke, B. J. Sternlieb, W. D. Wu, Y. J. Uemura, S. Tajima, and S. Uchida, Phys. Rev. B **48**, 12926 (1993).

[56] K. Kladko and P. Fulde, Int. J. Quant. Ch. **66**, 377 (1998).

[57] K. M. Kojima, Y. Fudamoto, M. Larkin, G. M. Luke, J. Merrin, B. Nachumi, Y. J. Uemura, N. Motoyama, H. Eisaki, S. Uchida, K. Yamada, Y. Endoh, S. Hosoya, B. J. Sternlieb, and G. Shirane, Phys. Rev. Lett. **78**, 1787 (1997).

[58] A. Kotani and Toyozawa, J. Phys. Soc. Japan **35**, 1073, 1082 (1973).

[59] R. Kubo, J. Phys. Soc. Japan **17**, 1100 (1962).

[60] H. Kuzmany, *Solid-State Spectroscopy* (Springer, Berlin, 1998).

[61] S. Larsson and M. Braga, Chem. Phys. Lett. **48**, 596 (1977).

[62] J. Luo and N. E. Bickers, Phys. Rev. B **47**, 12153 (1993).

[63] K. Maiti, D. D. Sarma, T. Mizokawa, and A. Fujimori, Europhys. Lett. **37**, 359 (1997).

[64] K. Maiti, D. D. Sarma, T. Mizokawa, and A. Fujimori, Phys. Rev. B **57**, 1572 (1998).

[65] Th. Maier, M. B. Zölfl, Th. Pruschke, and J. Keller, Eur. Phys. J. B **7**, 377 (1999).

[66] A. K. McMahan, R. M. Martin, and S. Satpathy, Phys. Rev. B **38**, 6650 (1988).

[67] L. L. Miller, X. L. Wang, S. X. Wang, C. Stassis, D. C. Johnston, J. Faber Jr., and C.-K. Loong, Phys. Rev. B **41**, 1921 (1990).

[68] H. Mori, Prog. Theor. Phys. **33**, 423 (1965).

[69] N. Motoyama, H. Eisaki, and S. Uchida, Phys. Rev. Lett. **76**, 3212 (1996).

[70] N. Nücker, J. Fink, B. Renker, D. Ewert, C. Politis, P. J. W. Weijs, and J. C. Fuggle, Z. Phys. B **67**, 9 (1987).

[71] K. Okada and A. Kotani, J. Phys. Soc. Japan **58**, 1095, 2578 (1989).

[72] K. Okada and A. Kotani, Phys. Rev. B **52**, 4794 (1995).

[73] K. Okada, A. Kotani, K. Maiti and D. D. Sarma, J. Phys. Soc. Japan **65**, 1844 (1996).

[74] K. Okada and A. Kotani, J. Phys. Soc. Japan **66**, 341 (1997).

[75] K. Okada and A. Kotani, J. Electron. Spectrosc. Relat. Phenom. **86**, 119 (1997).

[76] K. Okada and A. Kotani, J. Electron. Spectrosc. Relat. Phenom. **88-91**, 255 (1998).

[77] A. M. Oles and J. Zaanen, Phys. Rev. B **39**, 9175 (1989).

[78] E. W. Ong, G. H. Kwei, R. A. Robinson, B. L. Ramakrishna, R. B. Von Dreele, Phys. Rev. B **42**, 4255 (1990).

[79] F. Parmigiani, G. Samoggia, Europhys. Lett. **7**, 543 (1988).

[80] F. Parmigiani, Z. X. Shen, D. B. Mitzi, I. Lindau, W. E. Spicer, and A. Kapitulnik, Phys. Rev. B **43**, 3085 (1991).

[81] F. Parmigiani, L. E. Depero, T. Minerva, and J. B. Torrance, J. Electron. Spectrosc. Relat. Phenom. **58**, 315 (1992).

[82] F. Parmigiani, L. Sangaletti, A. Goldoni, U. del Pennino, C. Kim, Z.-X. Shen, A. Revcolevschi, and G. Dhalènne, Phys. Rev. B **55**, 1 (1997).

[83] J. Richter, Diplomarbeit, TU Dresden 1998.

[84] H. Rosner, H. Eschrig, R. Hayn, S.-L. Drechsler, and J. Málek, Phys. Rev. B **56**, 3402 (1997).

[85] H. Rosner, Dissertation, TU Dresden 1999.

[86] F. Sapiña, J. Rodriguez-Carvajal, M. J. Sanchis, R. Ibañez, A. Beltrán, and D. Beltrán, Solid State Commun. **74**, 779 (1990).

[87] R. T. Scalettar, D. J. Scalapino, R. L. Sugar, S. R. White, Phys. Rev. B **44**, 770 (1991).

[88] T. Schork and P. Fulde, J. Chem. Phys. **97**, 9195 (1992).

[89] T. Schork and P. Fulde, Int. J. Quant. Ch. **51**, 113 (1994).

[90] Z.–X. Shen, J. W. Allen, J. J. Yeh, J.-S. Kang, W. Ellis, W. Spicer, I. Lindau, M. B. Maple, Y. D. Dalichaouch, M. S. Torikachvili, J. Z. Sun, and T. H. Geballe, Phys. Rev. B **36**, 8414 (1987).

[91] Z.–X. Shen and D. S. Dessau, Phys. Rep. **253**, 1 (1995).

[92] W. H. Stephan, W. von der Linden, and P. Horsch, Phys. Rev. B **39**, 2924 (1989).

[93] M. Sugihara, M. A. Ikeda, and P. Entel, Phys. Rev. B **57**, 11760 (1998).

[94] H. Suzuura, H. Yasuhara, A. Furusaki, N. Nagaosa, and Y. Tokura, Phys. Rev. Lett. **76**, 2579 (1996).

[95] M. Takigawa, O. A. Starykh, A. W. Sandvik, and R. R. P. Singh, Phys. Rev. B **56**, 13681 (1997).

[96] S. Tanaka, K. Okada, A. Kotani, J. Phys. Soc. Japan **60**, 3893 (1991).

[97] S. Tanaka and T. Jo, Physica B **237-238**, 385 (1997).

[98] D. J. Thouless, Nucl. Phys. **21**, 225 (1960).

[99] J. M. Tranquada, S. M. Heald, W. Kunnmann, A. R. Moodenbaugh, S. L. Qiu, Youwen Xu, and P. K. Davies, Phys. Rev. B **44**, 5176 (1991).

[100] H. F. Trotter, Prog. Am. Math. Soc. **10**, 545 (1959); M. Suzuki, Commun. Math. Phys. **51**, 183 (1976); M. Suzuki, Phys. Rev. Lett. **146**, 319 (1990).

[101] D. Vaknin, S. K. Sinha, C. Stassis, L. L. Miller, and D. C. Johnston, Phys. Rev. B **41**, 1926 (1990).

[102] G. van der Laan, C. Westra, C. Haas, and G. A. Sawatzky, Phys. Rev. B **23**, 4369 (1981).

[103] M. A. van Veenendaal and G. A. Sawatzky, Phys. Rev. Lett. **70**, 2459 (1993).

[104] M. A. van Veenendaal, H. Eskes, and G. A. Sawatzky, Phys. Rev. B **47**, 11462 (1993).

[105] M. A. van Veenendaal and G. A. Sawatzky, Phys. Rev. B **49**, 3473 (1994).

[106] W. von der Linden, Phys. Rep. **220**, 53 (1992).

[107] C. Waidacher, J. Richter, R. E. Hetzel, and K. W. Becker, Phys. Rev. B **60**, 2255 (1999).

[108] C. Waidacher, J. Richter, and K. W. Becker, Europhys. Lett. **47**, 77 (1999).

[109] C. Waidacher, J. Richter, and K. W. Becker, submitted to Phys. Rev. B.

[110] R. Weht and W. E. Pickett, Phys. Rev. Lett. **81**, 2502 (1998).

[111] Z. Weihong, J. Oitmaa, and C. J. Hamer, Phys. Rev. B **52**, 12278 (1995).

[112] J. Zaanen, C. Westra, and G. A. Sawatzky, Phys. Rev. B **33**, 8060 (1986).

[113] F. C. Zhang and T. M. Rice, Phys. Rev. B **37**, 3759 (1988).

[114] R. Zwanzig, in *Lectures in Theoretical Physics* (Interscience, New York, 1961).

Acknowledgement

It is said that acknowledgements are only read by those who think they deserve to be mentioned. If this is true, many people will have an excellent reason to read this page. In fact, so many of my colleagues, friends, and relatives have given me so much essential support for this thesis that it seems impossible to do them justice with a written acknowledgement, how long and elaborate it may be. Nevertheless, let me give a short – and necessarily insufficient – list of all the distinguished physicists who have honoured me with their acquaintance, and without whom this thesis never would have been written.

I am much obliged to Prof. Klaus W. Becker for his supervision of this thesis. Many thanks to Dr. Frank Bagehorn, Dr. Ralf Hetzel, Arnd Hübsch, Jan Richter, Dr. Matthias Vojta, and all other (former) members of the Institut für Theoretische Physik at TU Dresden. The collaboration with experimental physicists has been one of the most important aspects of this thesis. Let me thank Stefan Atzkern, Prof. Jörg Fink, Dr. Mark S. Golden, Dr. Ralph Neudert from IFW Dresden, and Prof. Fulvio Parmigiani and Dr. Luigi Sangaletti from Brescia University. I acknowledge many helpful discussions with Dr. Stefan-Ludwig Drechsler and Dr. Helge Rosner from IFW Dresden, with Prof. Peter Fulde from MPI Dresden, with Prof. Wolfram Brenig and his group from TU Braunschweig, and with Prof. Wolfgang von der Linden and his group from TU Graz. Many thanks to all members of SFB 463, in particular to Prof. Clemens Laubschat and his group.

Finally, let me just express my deep gratitude to everybody who has helped me during the last three years.

HSSS AdminTools (c) 2001, last visited: Tue Aug 28 14:38:42 GMT+02:00 2001